# Confined Masonry: Theoretical Fundamentals, Experimental Test, Finite Element Models, and Future Uses

---

by

Lan Nguyen

B.S., University of Colorado Boulder, 2009

M.S., University of Colorado Boulder, 2011

A thesis submitted to the

Faculty of the Graduate School of the

University of Colorado in partial fulfillment

of the requirement for the degree of

Doctor of Philosophy

Department of Civil, Environmental, and Architectural Engineering

In Civil Engineering

This report entitled:

**Confined Masonry: Theoretical Fundamentals, Experimental Test, Finite Element Models, and Future Uses**

*Written by* Lan Nguyen

Has been approved for the Department of Civil, Environmental, and Architectural Engineering

_____

(Ross Corotis- Committee Chair- University of Colorado Boulder)

_____

(Franck Vernerey- Committee - University of Colorado Boulder)

_____

(Petros Sideris- Committee -University of Colorado Boulder)

Date_____

The final copy of this report has been examined by the signatories, and we

Find that both the content and the form meet acceptable presentation standards

Of scholarly work in the above mentioned discipline.

## Abstract

Lan Nguyen (Ph.D. , Department of Civil, Environmental, and Architectural Engineering)

Thesis directed by Professor Ross Corotis and Professor Guido Camata

Inspired from the MS thesis that investigated the underlying relationship between the implicit level of risk accepted for natural hazards and the level of economic, social and political development of Haiti, a developing country, this dissertation focuses structurally on the use of low-rise confined masonry (CM) buildings in natural hazard consideration areas. The research emphasizes the responses of the CM shear wall structure as a whole, as well as the material conditions in detail. Key findings are presented from experimental tests, computational modeling procedures, analytical results, and reliability analysis for CM structures followed with the summary of the behavior of CM subjected to in-plane loading.

This project covers behavior and reliability of CM structures subject to earthquake loading and enables informed decisions about risk in earthquake engineering design, including assessment of existing structures and retrofit design. Through experimental tests, development of a finite element analysis algorithm, and reliability analysis, this study found that structural integrity of a CM system is especially sensitive to the compression confining the wall from the surrounding concrete tie-frame and the materials used in the masonry panel. These parameters are addressed through the use of micro and macro modeling concepts, with the final model based on a macro-modeling strategy built by a force-deformation envelope curve prediction, and analysis that shows the structural safety aspect of CM in a recommended reliability index.

Unreinforced masonry contributes significantly to the number of structural failures, value of economic losses, and business disruption associated with natural hazards in the U.S. This study is an initial step towards providing the Masonry Standards Joint Committee (MSJC) with information on the CM system and build guidelines as a variation of the masonry infill system. For regular masonry buildings, this study provides a mechanism to improve the consistency and efficiency of building codes through explicit evaluation of design provisions. This research outcome is applicable to a large number of unreinforced masonry structures throughout the world, and as extension ranging from the vulnerability of lifeline system to historical preservation of masonry structures.

*This thesis is dedicated to the people of Haiti*

## Acknowledgement

I would like to start off by offering special acknowledgement to my technical advisor, Mr. Michael Schuller who provided instrumental guidance and direction to the project. His knowledge, advice, technical mentoring, and encouragement throughout my PhD program have always been appreciated.

I deeply appreciate Dr. Ross Corotis, committee chair/co-advisor, especially for his endless effort in finding financial support for me to be able to work on the thesis topic I choose, and Dr. Guido Camata for being my committee co-chair/co-advisor. By the help from both of advisers, I had an opportunity to study abroad in Italy for a semester, where I met and learned from such special people. Dr. Josko Ozbolt and Dr. Nicolas Tarque were two of them, who constantly offered many helpful suggestions and information throughout my research till the last semester of my PhD program.

I would like to extend my sincerest thank and gratitude to the two people who were side by side with me involved in this research: Mr. Michael Scott Cusack and Mr. Thomas Bowen. Only by the insight, guidance, encouragement, time, and effort contributed by all those involved could this work have been possible.

The members of my committee board, Dr. Jennifer Tanner Eisenhauer, Dr. Franck Vernerey, and Dr. Petros Sideris whom provided a great deal of help in my graduate studies, and to whom I am grateful for taking their time to serve on my committee. I am especially thankful for being

taught by Dr. Franck Vernerey, who introduced me to the beautiful world of finite element analysis and advanced mechanics of materials.

Acknowledgement is extended to those who provided help with the experimental portion of this research. Michael Scott Cusack contributed a great deal of laboratory assistance and helpful suggestions regarding the experimental work of this project from the start to finish which was greatly appreciated. William J. Cobb, Andrew Hoeschelle, and “Going to be Dr.”Kamtornkiat “Noom” Musiket are also thanked for their significant contribution to the laboratory work. Ben Gallaher is appreciated for his help directing me in testing materials as well. Thanks are specially offered to Kent Polkinghorne who worked closely with me in the instrumentation and data analysis. I greatly thank to be among a wonderful graduate office mates: Dr. MohammadReza Kabiri, Sarah Welsh Huggins, Cody Harrington, Yolanda Lin, Dr. Karim Farokhnia, Dr. Louis Foucard, Kanghyeon Koo, Eduard Benet, Boning Zhang, “Going to be Dr.”Emily Elwood, Dr. Holly Bonstrom, Dr. Siamak Sattar, Dr. Meera R Nandan, Umut Akalp, Mohammad Amin Hariri Adebili, Farhad Shahabi, Reza Behrou, Yuxiang Jing, Yao Wang, and Ji Yun Lee. Your supports and encouragement throughout my research has been significantly appreciated.

I would like to express my gratitude to Mr. Carlo Citto at Atkinson-Noland & Associates, for providing such a great help in modeling guidance. I greatly appreciate Dr. Richard Regueiro for his remarkable guidance in modeling nonlinear solid continuum mechanics. His insight and effective assistance mean a great deal to me, and especially to my future career. I would also like to express my appreciation to Dr. Yunping Xi, who supported and constantly provided me

guidance and technical help at any time I needed. I would like to specially thank Dr. Abbie Liel for her enthusiasm in teaching and creating a wonderful Liel Research Group, where I have learned so much from so many wonderful graduate students.

I acknowledge all the authors whom I cited in my selected reference chapter. I specially thank Dr. Ziad Taqiedinn, who provided me the material to learn modeling remotely, and provided me such a great deal of help in finite element analysis and modeling through his research study.

I specially thank Ms. Gretchen Lee, who introduced me to the Achievement Reward for College Scientists, an organization from which I received scholarships over two years. The support provided a tremendous help for me. I truly appreciate the Public Entity Risk Institutes Fellowship for their generous laboratory support. I also thank Dr. Molennaar and the CEAE Department at CU for all the support in providing the materials and access to laboratory testing equipment, and in offering me the Graduate Teaching Assistant position while I pursue my degree.

I still could not even imagine how hard it is for Haiti, the country that lost more than 200,000 people at once. There is only one solid reason to study the structural safety aspect of confined masonry structures that it is in need to me. As every difficult part of the learning journey, I fortunately know that I am surrounded by the sweetest world ever. The warm heart attitude and encouragement comes from ever where. I am inspired by the work that Build Change is doing, and am motivated by Mr. Mark Sinclair's encouragement. I deeply thank my family, my mother, Anh Do, my sisters Quynh Nguyen and Lilly Nguyen, my brothers Son Nguyen and Tan Nguyen for constantly reminding and encouraging me to complete doing the right thing with all

my effort. I truly thank all my friends, all my awesome people at 5 Stars, who significantly support me as always.

Finally, I would like to thank the most important person, my husband, Andrew Geister, for whose continual support, encouragement, understanding, love, and patience I am ever grateful.

## Contents

## List of Figures

## List of Tables

# Chapter 1.
# Introduction

## 1.1 General Remarks

Based on their performance in many earthquakes, unreinforced masonry (URM) structures have been deemed unsatisfactory for practical use in seismic regions. They are generally classified as brittle, and highly vulnerable to lateral loads, such as from high winds or earthquakes. However, earthquake survival of many masonry buildings, particularly those constructed with the practice known as "confined masonry" (CM) for low rise buildings in Indonesia in 2008, Chile in 2010, and Peru in 2010, indicates that this does not have to be the case (Brzev et al., 2010), (Tanner & Carboni, 2011), (Quiun, 2011). Indeed, many CM structures behaved very well, and were fully capable of resisting the lateral loads caused by the earthquakes without significant damage. This research will provide a mechanics-based multi-scale theoretical, computational and experimental approach to understanding the fundamental behavior of CM structures and will explain their superior multi natural hazards performance.

This research is based on two critical and fundamental observations:

- The United States has a very large portfolio of unreinforced masonry structures in its current inventory, one particular example among other building structures are the tribal houses for Native Americans, many of which are in locations that are now known to pose significant seismic and high wind risk.
- Various ad hoc construction techniques for unreinforced masonry developed and used in other countries, such as confined masonry (CM), have tremendous potential for

refinement and adoption in the U.S for both new construction and retrofit scenarios and constitute a new structural application system.

## 1.2 Motivation and Objectives

This research is an outgrowth of master's research that investigated the underlying relationship between the implicit level of risk accepted for natural hazards, and the level of economic, social and political development of the country. Vulnerability information was related to the seismic provisions of the building codes and the atmosphere of code enforcement. Objectives for this research include:

(1) Analyze the behavior of a CM shear wall subjected to in-plane loading.

(2) Investigate the impact of different configuration in design aspects on the shear wall.

(3) Construct a finite element model to perform numerically analysis for a CM shear wall.

(4) Investigate the effect of material properties on structural reliability of a CM shear wall.

## 1.3 Scope and Organization

This study includes a summary of the observed behavior of CM after earthquakes, laboratory testing results, and modeling strategies for masonry structures. This research will encompass finite element modeling, structural assessment, and design/construction practice, with a particular focus on numerical mechanism convergence issues.

Chapter 2 will first investigate the basic background of CM structures, particularly emphasizing the mechanics-based behavior of the confined structure as a whole, as well as the material in detail. In this Chapter, local and global pictures of load path dependency for a structure will be investigated. This study will then emphasize the resistance capacity due to in-

plane loading conditions that are inherent within the CM mechanical behavior itself. Understanding the mechanics behavior of these composite structures as well as the loading conditions will provide the fundamental bases for the mechanics mechanism of the failure modes within that structure.

Chapter 3 lists the experimental work completed in this research. The Chapter points out the CM wall shear stiffness sensitivity and ductility with respect to different surrounding reinforced element configurations subjected to in-plane loading. The chapter focuses on all tasks performed to construct and test CM shear walls from a component standpoint, such as unit brick tests to whole wall structure testing. The majority of the work in this Chapter will cover the experimental set up for CM components in accordance with ASTM Standards and for the CM walls according to the EERI guideline for building construction, as well as address the in-plane shear capacities of a CM wall panel observed and recorded directly from experimental testing. This experimental work includes design, construction, and testing CM shear wall systems to evaluate the structure's sensitivity with respect to compression confinement within the frame, the materials used in the masonry panel, and the reinforcement scheme. The project explicitly emphasizes laboratory work such as specimen construction, instrumentation, materials behavior monitoring during the testing process, and ensuring construction safety in the testing facility while work is taking place. In conjunction with a literature review, this experimental test will serve as a validation for the finite element analysis approach, which is covered in Chapter 4.

Chapter 4 covers the available modeling methodologies for quasi-brittle materials including concrete particularly for reinforced concrete tie elements, and an unreinforced masonry panel inside a CM wall. The literature review from the chapter together with the

analysis leads to a choice of finite element analysis methodology which used in this study. Despite many numerical and finite element models in existence, there is not clear understanding of when the masonry can be treated as a homogenous panel, or damage recovery capacity of materials in unloading states. These previous studies will, however, provide important information for this research. This Chapter is set to demonstrate a macro modeling approach, an interface model approach, and recommendations to bridge the gap between the two approaches with the use of finite strain theory and damage mechanics. In this Chapter, finite strain theory is used to capture the most possible plastic strain within an element. In addition, a damage variable is applied to enhance the stiffness degradation that occurs in the structure. Finally, a damage model is presented for walls subjected to cyclic loading using ABAQUS software. Modeling examples include a CM shear wall subjected to monotonic as well as cyclic loading; shear capacity for the wall panel is calculated and validated to the experimental results provided from Chapter 3.

In Chapter 5, analysis of reliability of material used in confined masonry under concentric compression stress is presented in this chapter. Discussion for reliability in CM walls is also presented. The analytical findings theoretically solve the engineering design problems associated with composite shear wall capacity, stiffness degradation, and anticipation for ultimate inelastic behavior for CM shear walls.

Chapter 6 concludes a summary of the work, the validation of the research by the use of the experimental results, and the limitations within the study, along with recommendations for further research topics. It also contains a full list of selected references used throughout the research work. The author wishes to thank all the authors who contributed a tremendous

amount of valuable information and intelectuall findings which she has found and incorporated into her research.

# Chapter 2.
# Masonry Components and Confined Masonry Background

## 2.1 Confined masonry background

Confined masonry structures are built in almost the opposite manner to reinforced concrete (RC) frame infill structures. In CM structures, the wall is built first, then the concrete beam and columns are cast around the wall panel. In this type of construction, the masonry is confined by the surrounding beam and columns as the concrete shrinks slightly while it cures (Brzev et al., 2010). Ideally the panel should be encased by both a beam and columns, but when used in retrofit for existing URM structures, confining vertical elements (RC tie-columns) on the sides of the openings are not always feasible. The following Figure 2-1 shows the construction sequence of CM as opposed to the sequence showed in Figure 2-2 for reinforced masonry infill wall panel.

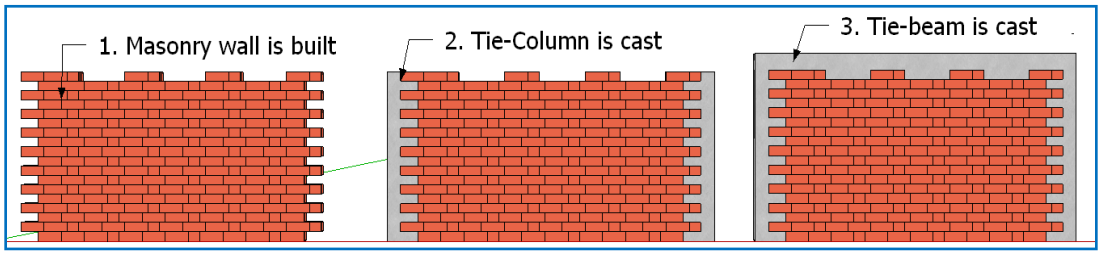


**Figure 2-1. Confined masonry construction sequence (Brzev, 2008)**

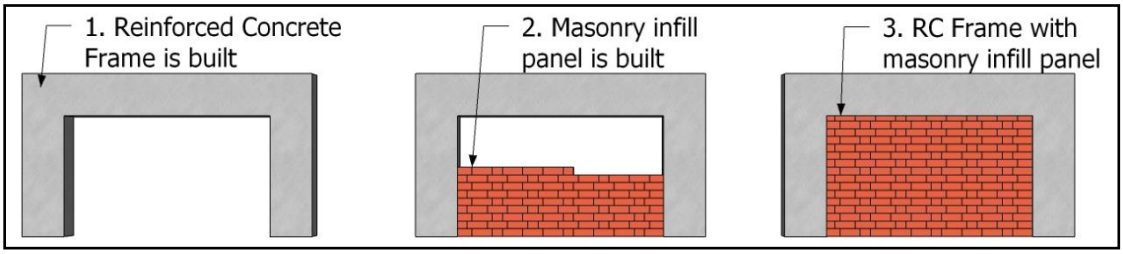


**Figure 2-2. Reinforced concrete frame masonry infill construction sequence (Brzev, 2008)**

In CM structures, vertical elements, called *tie-columns*, and horizontal elements, called *tie-beams*, resemble columns and beams in a CM wall panel, but do not function in the same

manner as those in typical RC frame construction. They tend to be of far smaller cross-sectional dimensions compared to those of RC frames Figure 2-1 and Figure 2-2. In addition, beams in CM construction are not intended to carry vertical load since confined masonry walls themselves are load-bearing, whereas in RC frame masonry infill, the RC frame is designed to carry loads. Until recently the infill panel was considered to be non-structural component and not contribute to the result or lateral capacity. Tie-columns in CM construction are slender, and along with the similarly slender tie-beam, cannot provide effective frame action. Tie-columns are cast against a rough (toothed and/or doweled) surface as seen in Figure 2-1. As a result of this type of connection, the wall in CM associates with the surrounding elements as one. When subjected to lateral seismic loads, walls in confined masonry members act as one piece together, just like walls in load bearing masonry construction or RC shear wall construction as seen in Figure 2-3.

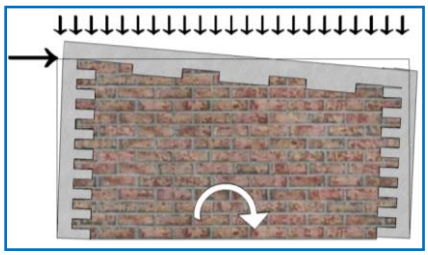

**Figure 2-3. CM load bearing wall**

Whereas infill walls in RC frames act as diagonal struts showed in Figure 2-4 below.

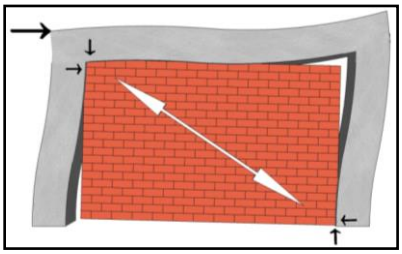

**Figure 2-4. RCMI wall**

## 2.2 The Uses of confined masonry to present

Masonry structures have been used extensively throughout history, including, for instance, the still-standing first century Pont du Gard in France and BCE Roman structures. For countries in seismic regions, there are many examples of reinforced frame structures with masonry infill, reinforced masonry, and other techniques. An alternative to masonry infill and reinforced masonry is confined masonry. In the U.S., confined masonry (CM) is known, but its usage is very limited compared to other countries such as Pakistan, Indonesia and Chile. Shown in Figure 2-5 is the typical confined masonry buildings used in Chile. Noting the survival of these multi-story buildings after the earthquake in 2011 reported in Tanner's study (Tanner & Carboni, 2011) raises the open question of the small usage for CM in the U.S. Reasons for this could relate to insufficient understanding, ability, skill, coordination between trades, and finally perceived cost. A fundamental understanding of CM could open the door to its extensive U.S. use as an alternative in retrofit and strengthening of structures, especially for essential facilities such as schools, hospitals and fire stations, many of which are constructed of masonry.

**Figure 2-5. Typical Confined Masonry Buildings in Chile (left: 2 story apartment, right: 4 story apartment) (Brzev et al., 2010)**

An increased use of CM structures is taking place in developing countries such as Pakistan after the 2005 Kashmir earthquake (Ibrar, Naseer, & Ashraf, 2012) and Haiti after the 2010 earthquake (Build Change, 2010). Other countries such as Iran have seen augmented use of CM as well as seismic code modifications for CM building structures (Sarrafi & Eshghi, 2012).

### 2.3 Load path and diaphragm effects in confined masonry

In an earthquake, load is transmitted to the building from its base. Thus the entire building and its contents experience the force. In general, the magnitude of this force which individual members experience is proportional to their mass. The ratio of the CM walls (parallel to the line of action) to the non-CM walls is the most important key to resistance of lateral loads. This relates to the amount of lateral force from either wind or earthquake that would be assumed to be resisted by the vertical wall. The lateral load transmitted to walls is different depending on which type of diaphragm is present in the structure. Buildings with rigid diaphragms are very common in most countries where confined masonry has been practiced. A RC roof structure, for example, acts as a rigid diaphragm (Roberto et al., 2011). For buildings with rigid diaphragms, the magnitude of shear forces in the walls is in direct proportion to the wall rigidity (relative to the rigidity of other walls laid in the same direction). In other words, under symmetrical loading a rigid diaphragm will cause each vertical wall parallel to the line of action to deflect an equal amount, and thus a vertical element with a high rigidity will resist a greater proportion of lateral force than an element with a lower rigidity. In low-rise buildings, wall rigidity is proportional to the wall's cross-sectional area. Torsional effects need to be considered, and may increase seismic forces in some of the walls.

Wood and thin metal sheet roofs in a building are classified as flexible diaphragms. In a

flexible diaphragm roof, the lateral force transmits to the shear walls differently as compared to the transmission discussed in the previous paragraph. For buildings with flexible diaphragms, the in-plane flexural mechanism in the diaphragm is critical because the lateral forces cannot be transmitted to the stiffer walls oriented in the direction of the seismic action. In-plane bending in flexible diaphragm is analogous to a series of beams spanning between supports. Lateral force distributed form a flexible diaphragm onto the vertical shear wall is similar to the tributary distributed load scenario.

In reality, structural diaphragms are never completely rigid or completely flexible. The Minimum Design Loads for Buildings and Other Structures (ASCE-7, 2005) provides guidelines for classifying diaphragms as rigid or flexible, however, the definitions are approximations based on assumptions that have proven to be reasonable in the past. These assumptions allow the engineer to calculate the forces in elements of the lateral force resisting system without explicitly including diaphragms in the structural analysis (Brandow, Ekwueme, & Hart, 2007).

## 2.4 Failure Modes

### 2.4.1 In plane shear failure

The shear failure mode for in-plane failure can be characterized as a distributed diagonal cracking in the wall. The failure of a tie-column also takes place when cracks propagate from the masonry wall into the tie-column; the masonry panel loses its resistance and force is completely transferred to the end of cracks, and finally shears the column off. When the load increases, damage forms in the tie-column with extensive crushing of concrete (also experienced as a *toe-crushing* condition) and yielding in the reinforcement, inducing “plastic hinges” as seen in Figure

2-6. This plastic hinge deformation type is different when compared to the plastic hinges in RC frame masonry infill panel. The distinguish failure mechanism will be disccused later in Chapter 3.

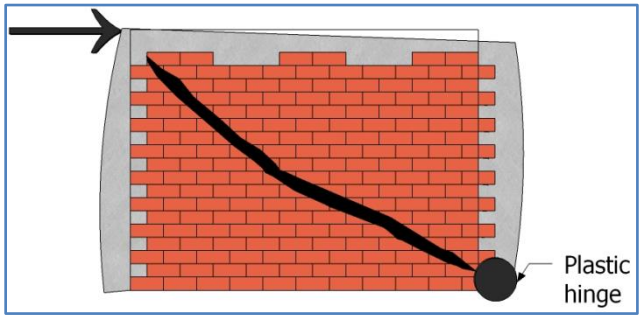


**Figure 2-6. In plane shear failure mode**

### 2.4.2 In plane flexural failure

*Flexural failure* due to in-plane lateral loads is characterized by horizontal cracking of the mortar bed joints located on the tension side of the wall. Separation of the tie-columns from the wall may occur in some cases when a toothed wall-to-column connection is absent, and there are no connecting ties between the tie-column and the wall panel (Bartolome & Quiun, 1992), (Roberto et al., 2011) as shown in the following Figure 2-7.

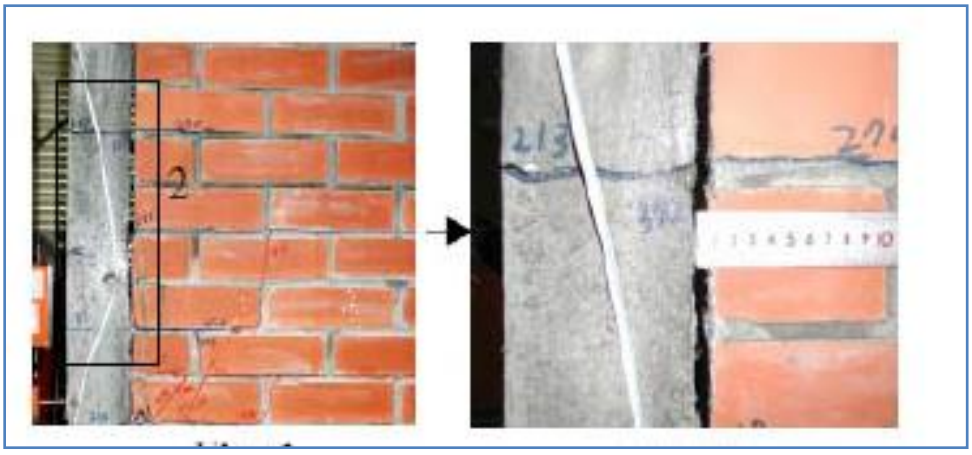

**Figure 2-7. In plane flexural failure in CM (EERI, 2010)**

This chapter briefly covers the overall behavior of confined masonry structure subjected to lateral acting load particularly for in-plane loading. In the next chapter, the experimental test will be discussed so that the technique and fundamental ideas behind the design, construction practice, and testing used in research can be illustrated.

# Chapter 3.
# In Plane Experimental Test on Confined Masonry Shear Walls

## 3.1 The purpose

In CM walls, the investigations on the effect of the vertical and horizontal wall reinforcement as well as reinforcement details were done by Yoshimura et al. in 1996 (Yoshimura, Kikuchi, Okamoto, & Sanchez, 1996). Eight different specimens were designed and tested under a constant gravity load and alternately cyclic repeated lateral forces. Test results indicate that the vertical and horizontal wall reinforcing bars provided in CM walls play an important role for developing higher strengths and better deformability (Yoshimura, Kikuchi, Okamoto, & Sanchez, 1996). Ibrar et al. designed and tested eight specimens for four types of CM walls with varying sizes of confining elements and reinforcement ratio using the same types of construction materials for the specimens in all tests. In their study, eight tests underwent constant vertical and cyclic horizontal loading in a displacement controlled environment (Ibrar, Naseer, & Ashraf, 2012). Irmies (2000) studied the influence of tie column reinforcement ratio on the seismic behavior of masonry walls. It was concluded that confining the unreinforced masonry walls by tie columns increase lateral resistance capacity of the masonry wall (Irmies, 2000). The investigation included the CM walls' lateral strength, stiffness, ductility and cracking pattern and it was found that by increasing the size of the confining element, the lateral strength, stiffness, and ductility of the CM wall increased. However, the increase of reinforcement did not affect the lateral strength or cracking pattern, even though the initial stiffness and ductility marginally increased (Ibrar, Naseer, & Ashraf, 2012). These eight CM walls were designed and tested in Iran according to the Iranian Seismic Code. The results were informative in terms of the effects of head joints, central

window opening, and vertical loading on the seismic behavior of the CM wall. Test results show that the minor changes in the construction of the CM walls will considerably affect their behavior under cyclic loads (Sarrafi & Eshghi, 2012).

This research shares the same goal with all the aforementioned above. The main goal is to bring attention to current and future research in structural safety aspects of CM buildings for new designs in Latin America, as well as for existing unreinforced masonry structures in America. In doing so, it is important to address the need that could potentially provide information to the existing guideline for CM structural design. Of interest is the NTC-M, 2004 included in Seismic Design Guideline for Low Rise Confined Masonry Buildings published in 2011 by the Earthquake Engineering Research Institute (EERI) Appendix A. According to the Seismic Design Guideline for Low Rise Confined Masonry Buildings, concrete tie elements can either built by toothed configuration or by smooth configuration with steel reinforcement dowels as shown in Figure 3-1 (Roberto et al., 2011). The designs of testing specimens in this research were made to address two considerations upon the aforementioned guideline for tie columns: (1) to confirm whether or not the CM shear wall capacities for these two configurations are compatible. (2) To evaluate the ductility in CM wall with dowel through the design of using a single dowel embedded in the tie column instead of two as recommended in the Seismic Guideline. This is done to further point out the application of drilling and placing rebar to enhance shear capacity by converting existing URM wall structures to CM structures.

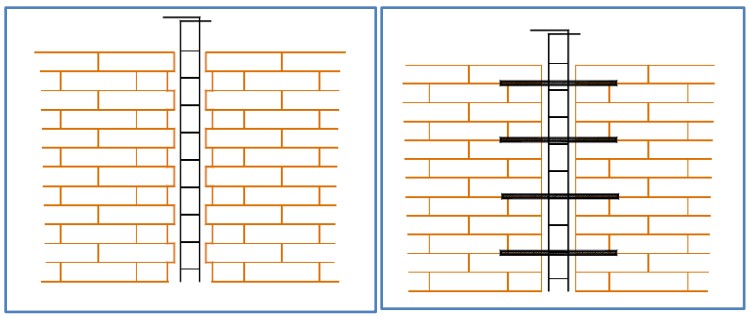

Figure 3-1. Two configurations for constructing tie columns in CM wall

## 3.2 Design of test specimens

### 3.2.1 Building layout

To be consistent with the guideline mentioned in Section 3.1, a one story CM building was selected as a typical structure. The plan of the structure is drawn and is shown in Figure 3-2. The lower RC bond-beams are restrained against the horizontal and vertical translations while the upper one transfers gravity and lateral loadings from the roof. The roof slab is assumed as a rigid diaphragm because the lateral forces are distributed by the in-plane stiffness and strength of the shear walls. It should be mentioned that in a flexible diaphragm, the total forces sustained by the shear walls will depend on the area supported by each wall and the flexible diaphragm is not capable of transferring either rotational or torsional forces.

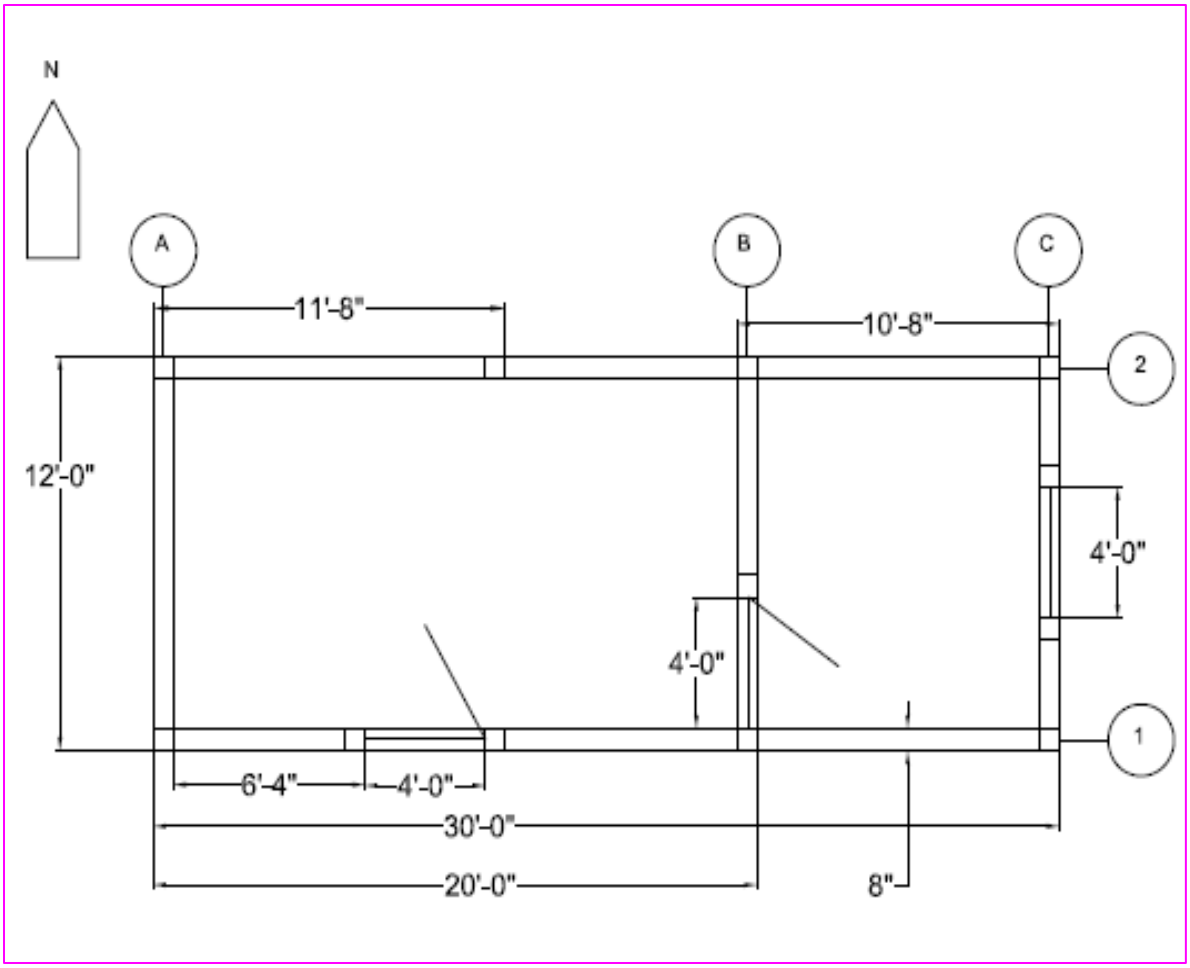


Figure 3-2. Building Layout

Building information for the scaled down design can also be found in the following Table 3-1.

| Building Information | Value | Units | Value | Units | Notes |
|---|---|---|---|---|---|
| Building Length | 6.0 | ft | 1.83 | m | N-S---> Seismic dirtn |
| Building Height | 5 | ft | 1.52 | m | |
| Building Width | 15 | ft | 4.57 | m | E-W |
| A/floor | 90 | $ft^2$ | 8.361 | $m^2$ | per floor |
| Usage Area | 90 | $ft^1$ | 8.361 | $m^2$ | per floor |

Table 3-1. Building information

Design configuration values for a protocol test element are listed in the following Table 3-2

| Wall | Value | Units | Value | Unit |
|---|---|---|---|---|
| Scale factor | 1 | | | |
| Wall L | 6 | ft | 1.8 | m |
| Wall H | 5 | ft | 1.5 | |
| Wall thickness | 8 | in | 20 | cm |
| Wall A to Wall B | 20.3 | ft | 6.2 | m |
| Tributary length | 10.2 | ft | 3.1 | m |
| Factored Line load on wall A | 997 | lb/ft | 0.70 | MPa |
| Check compression Wall A | 10 | psi | | |
| Un-factored dead load on wall A | 254 | lb/ft | - | - |

**Table 3-2. Wall information**

### 3.2.2 Laboratory component design and fabrication of test specimen

The specimen was comprised of three major components: the foundation pedestal, the double wythe solid clay brick wall, and the reinforced concrete frame consisting of two tie columns and one tie beam. Figure 3-3 shows the formwork, reinforcing layout and construction of the concrete foundation pedestal. The concrete foundation was designed to be 11 ft [3.35m] long, to be able to tighten to the strong floor at both ends. Contact area underneath the foundation was set with rubber mats and the use of a pressurized pump to fill the void between the foundation and the strong floor with fluid grout. The pedestal represented the foundation and therefore it could not move or slip during the test. For this reason, the pedestal was tensioned to 72 kips [4448N] at both ends to the lab strong floor using a center-hole jack and high strength Dywidag threaded rods to prevent slipping during the test, as shown in Figure 3-3, when concrete was at its full strength at 28 days. Later discussion will cover more detail for this slipping constraint for each wall test. The reinforcement layout for the pedestal was comprised of (4)-#9 longitudinal bars running the length and #3 stirrups on 15 inch spacing.

Figure 3-3. Footing and reinforcement for tie elements; Post tension jack on Dywidag rod

As specified in the structural plans, the concrete for the foundation has a compressive strength of 4000 psi [27.6 MPa]. The concrete cylinder test results for the pedestal can be seen in Figure 3-4.

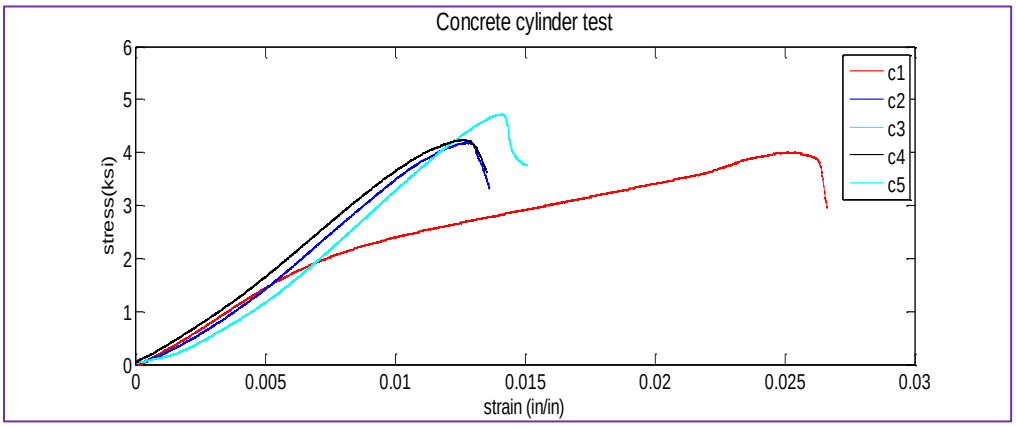


Figure 3-4. Concrete cylinder FDN test

To keep the mortar to be similar to the mortar type used in Haiti construction and in developing countries, average strength mortar type N was used in this experiment. The masonry wall was built the same way it is shown in the construction sequence shown in Figure 2-1 previously and was allowed to cure in the Structures and Materials Laboratory (SML) for 28 days.

As seen in the structural drawings in Figure 3-5, there are mechanical connections used throughout the cross section of the wall to transfer loads between specific components. To transfer the lateral load to the foundation the reinforced tie columns were embedded 12 inches [31cm] down into the foundation. Double wythe solid clay masonry walls were built 7 days after the concrete footing was poured as seen in Figure 3-5, Figure 3-6. The two walls were designed according to the Seismic Design Guideline for Low Rise Confined Masonry Buildings and also based on the specifications for unreinforced masonry shear wall panel per the 2011 MSJC code (see Appendix A). The two walls were built by a group of three experienced masons to possibly eliminate the workmanship errors, enhance construction techniques, and effectively quicken the construction procedures.

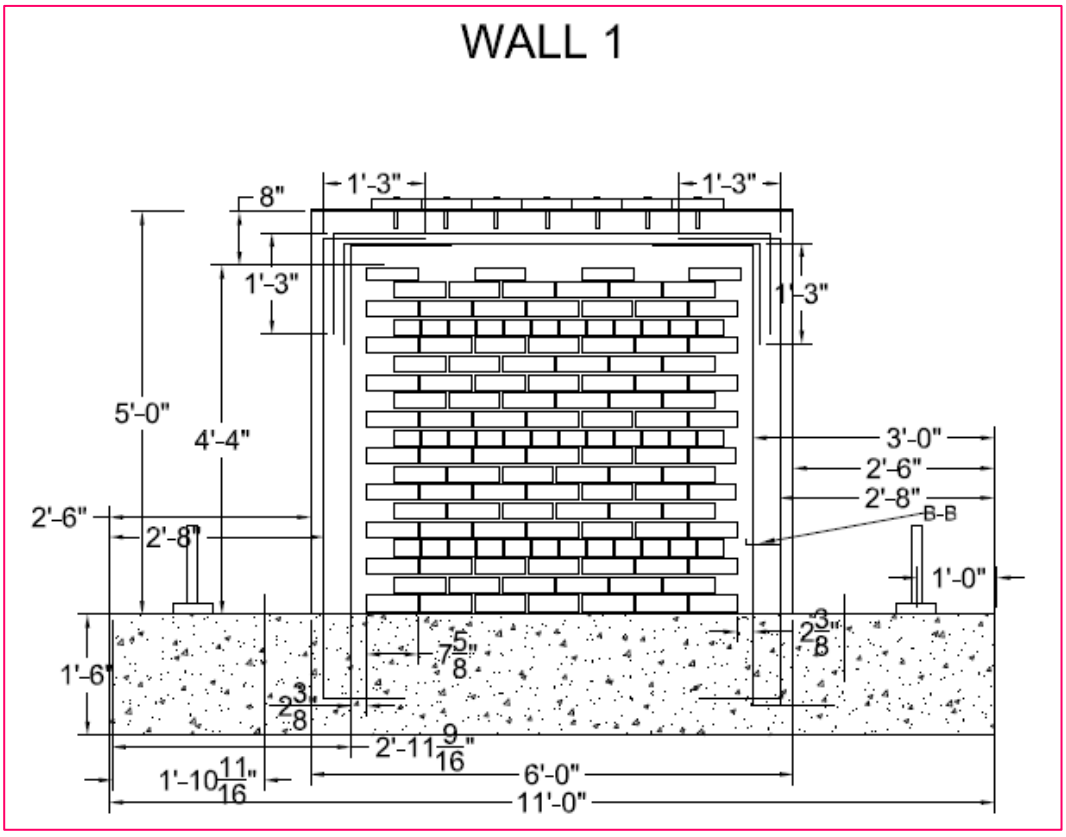


**Figure 3-5. CM Wall 1 assembly drawing**

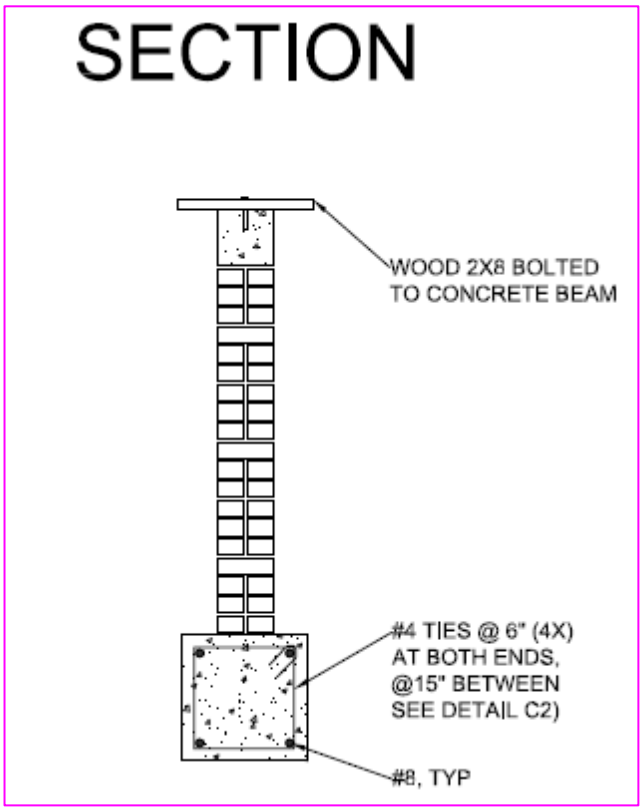


**Figure 3-6. CM Wall 1 section drawing**

Running bond was chosen for the wall configurations. Header courses were built every 5 courses. The toothed wall setup was built with alternating courses extending out on both ends of wall CM1, and reinforcement dowels were placed every 16 inches [40.6cm] on center into the smooth wall panel of wall CM2 as seen in Figure 3-7, Figure 3-8, and Figure 3-9. On wall CM2, instead of using two reinforcement bars as noted on the detailing requirement for the connection between wall panel and tie column, one bar was intentionally used since the research aims to investigate the potentially of retrofitting purposes. Changing this reinforcement detailing does not violate the requirement of the wall to tie-column interface since the dowels are not necessary for buildings up to two stories high according to the guideline (Roberto et al., 2011). Due to the high absorption properties of the brick, the masons considered the bricks to be "hot."

To reduce mortar shrinkage due to the water loss, the author watered the brick every other day for 14 days as recommended in the studies done by (Amadei, Sture, Saeb, & Atkinson, 1989) and (Mehrabi, Shing, Schuller, & Noland, 1994).

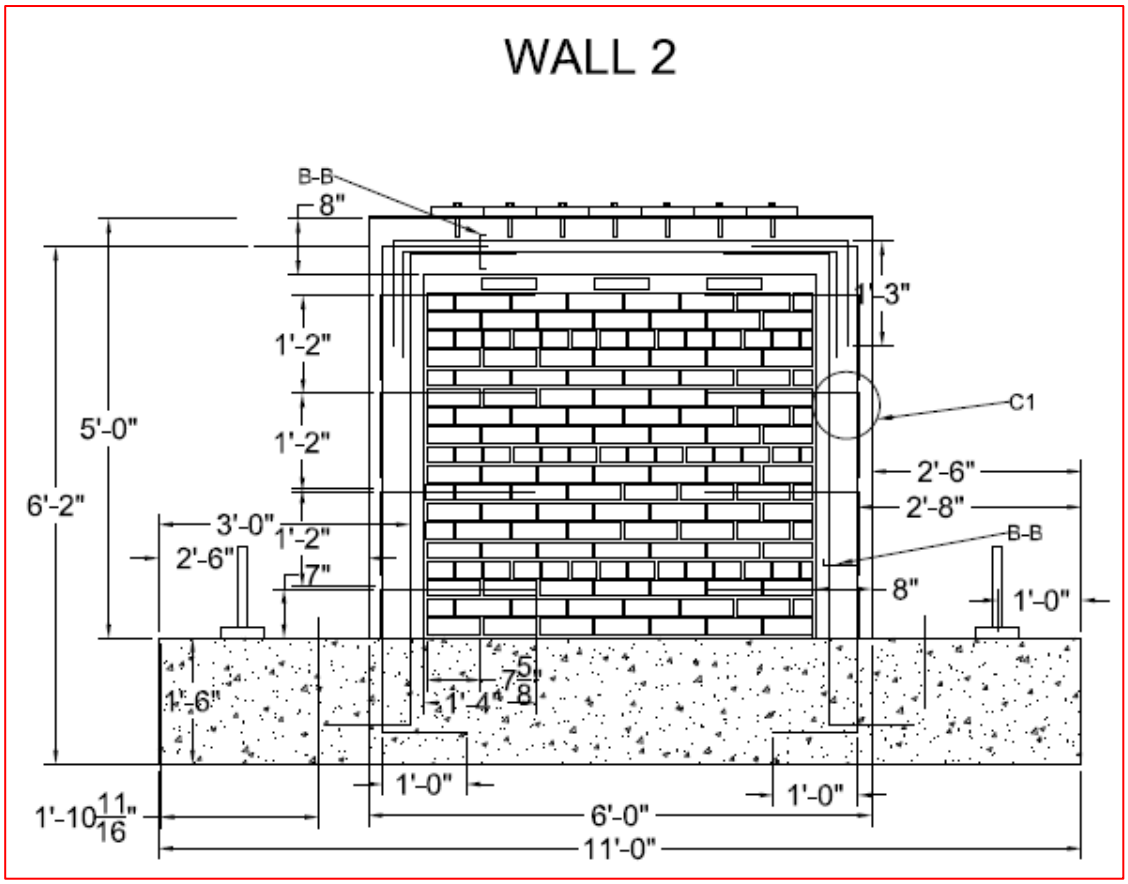


**Figure 3-7. CM Wall 2 assembly drawing**

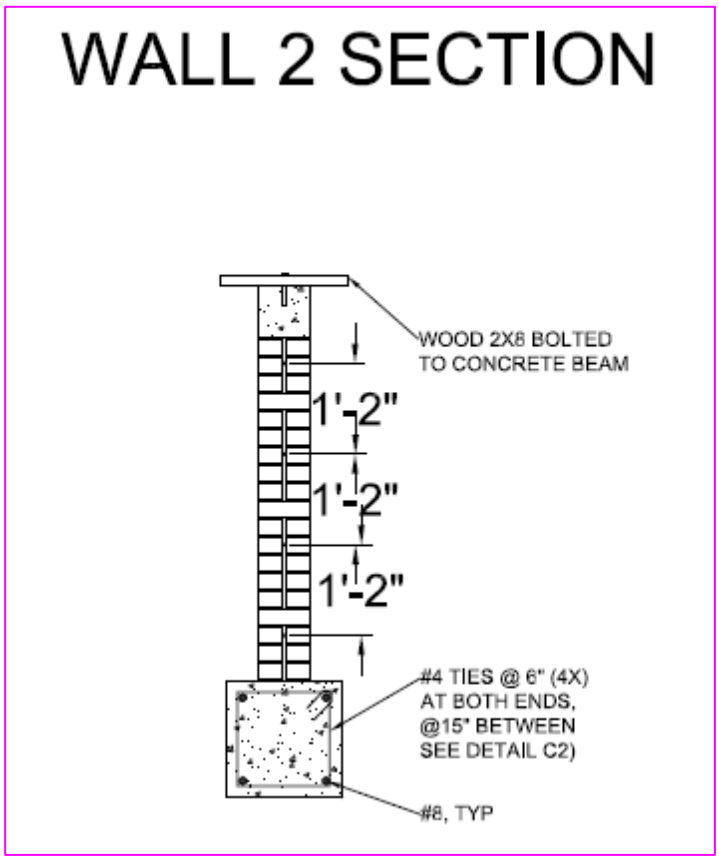


Figure 3-8. CM Wall 2 section drawing

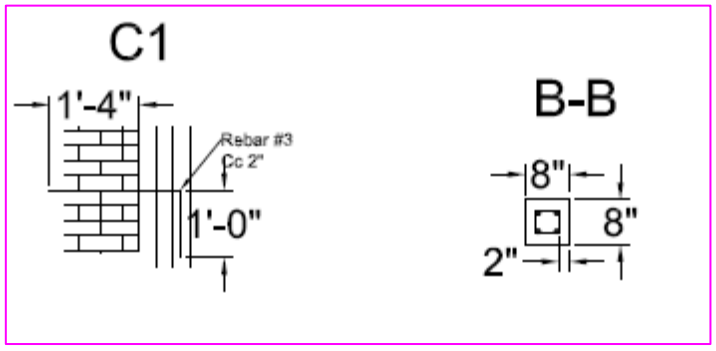


Figure 3-9. CM Walls details drawing

Reinforcement detail on both walls can be seen in the following Figure 3-10.

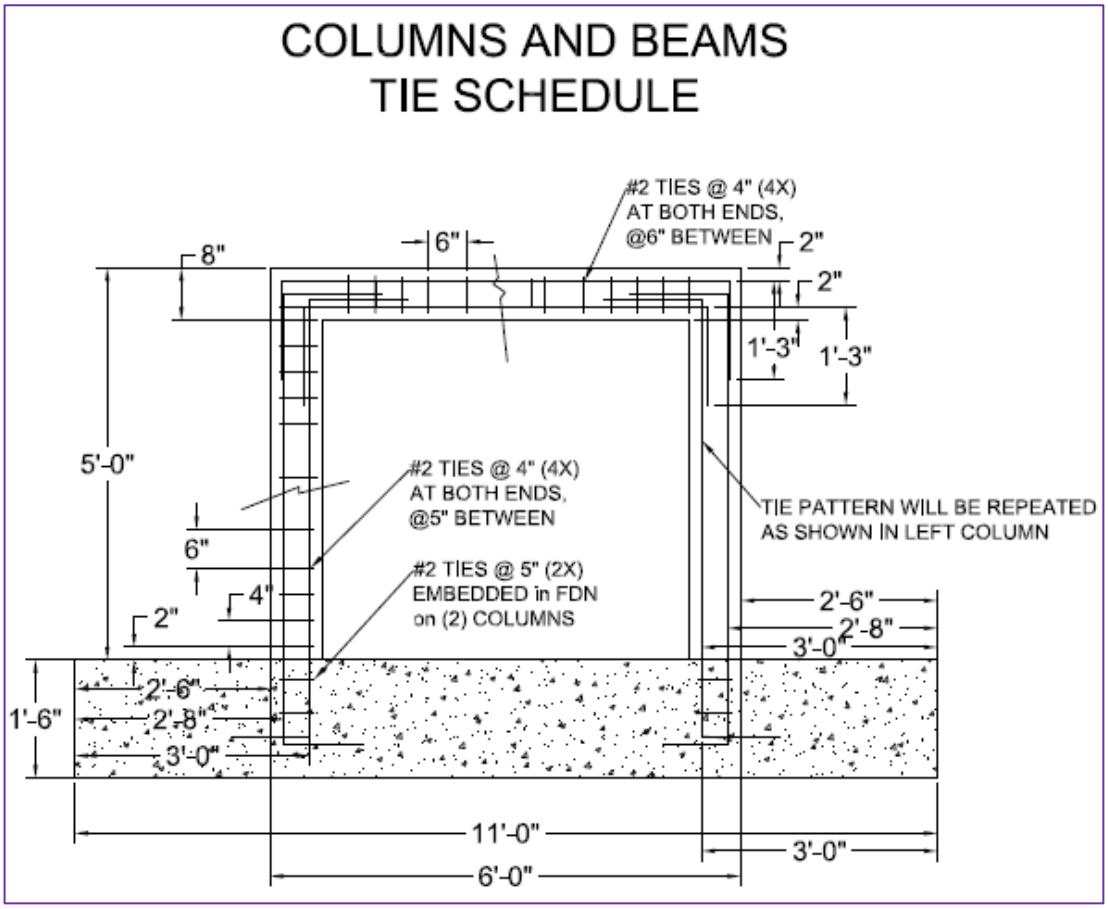


**Figure 3-10. CM Walls tie schedule drawing**

The construction for two CM shear walls can be seen in the following Figure 3-11.

**Figure 3-11. Construction of masonry wall panels**

The last components of the specimens were the 7.625 inch by 7.625 inch [20cm x20cm] cross sectional area reinforced concrete tie elements. The tie elements were cast-in-place 14 days after the construction of the masonry wall panel. Framework was built surrounding the wall panel and concrete was poured to build columns and beams. The frame elements are the important part of the test specimen because the lateral load was applied at the tie beam and was transferred through the specimen. The reinforcement for the tie beam and tie columns consisted of continuous (4)-#3's on both the inside and outside face with #2 smooth ties at 6 inches on center. A325 bolts were placed on the top beam prior to casting to use later for the assemblage of wood boards to hold the roof load. Shown in the following Figure 3-12 are the two test specimens after casting the frame element.

**Figure 3-12. Concrete tie elements**

The construction and design of test specimen has to be planned in advance to best fit the condition of the lab space as well as some constraints such as: the reaction wall's bolt pattern, tight bolt spacing on the strong floor, and other factors. The lateral force was applied at the tie beam cyclically; consequently a set of two plates with holes were fabricated to connect to the actuator swivel head and connected to each other by the use of 4 Dywidag steel rods as seen in Figure 3-13.

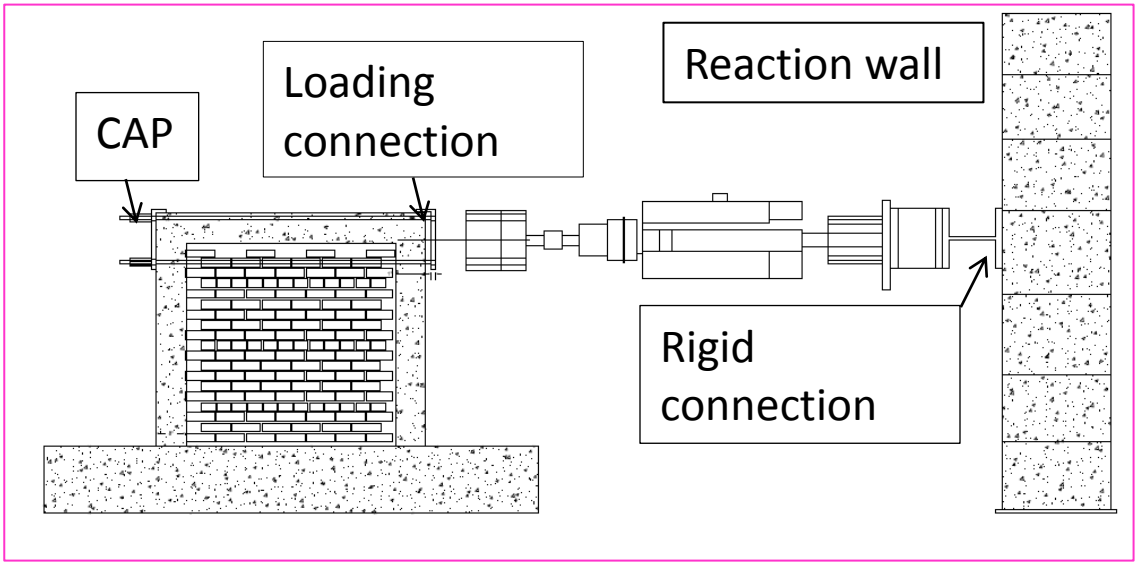


Figure 3-13. Specimen cap, loading connection, and reaction wall

The design for the cap connection and the cap details can be seen in the following Figure 3-14 and Figure 3-15.

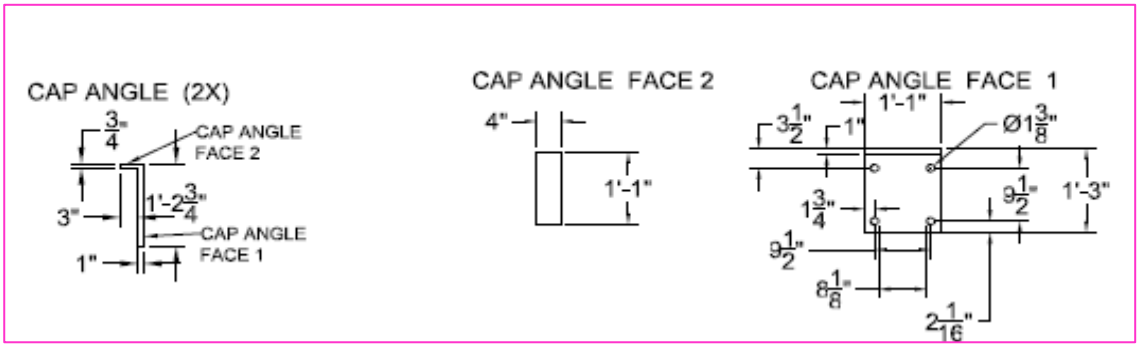


Figure 3-14. Cap detail drawing

Figure 3-15. Cap connection and details

Construction of the two walls in the Structures and Materials Laboratory (SML) can be seen in the Figure 3-16.

**Figure 3-16. CM shear walls built in the SML**

### 3.2.3 Units

The following types of masonry units are commonly used for CM construction:

1. Solid concrete block
2. Hollow concrete block
3. Solid clay bricks
4. Hollow clay tiles and blocks

The experimental carried out for CM wall used the solid masonry bricks, which are commonly used in developing countries.

### 3.2.4 Compressive test on unit brick

Compression testing for unit brick was carried out as part of this experimental chapter; a set of five half brick units were capped with gypsum cement and placed under the compression loading frame in an MTS machine. According to ASTM-C67, a common loading rate for unit brick compressive testing is approximately 0.003 in/s [0.0762mm/s]. However, the goal in this study is to statically load the specimen until the so-called post peaks occur, therefore the loading rate

chosen was 0.0001 in/s [0.00025mm/s]. Shown in the following Figure 3-17 are five chosen specimens.


Figure 3-17. Half unit brick

Test result for the unit compressive strength can be seen in the following Table 3-3.

| Unit Compressive Strength -ASTM C67-12-Section 7 | | | | | | Ref. (ASTM-C67-7.4.1) | |
|---|---|---|---|---|---|---|---|
| Specimen | $L_{after\ cut}$(in)[cm] | b(in)[cm] | W (lbf)[kN] | A($in^2$)[$cm^2$] | Fm psi [MPa] | C=W/A(psi) [MPa] | SDVT |
| B1 | 3.31[8.41] | 3.73[9.47] | 58552[260] | 12.3[89.7] | 4742[32.7] | 4470 [30.8] | 766.1 [5.28] |
| B2 | 3.51[8.91] | 3.75[9.52] | 43611[194] | 13.2[84.9] | 3313[22.8] | | |
| B3 | 3.31[8.41] | 3.72[9.49] | 64535[287] | 12.3[79.4] | 5241[36.14] | | |
| B4 | 3.51[8.91] | 3.78[9.60] | 65496[291] | 13.3[85.6] | 4936[34.0] | | |
| B5 | 3.61[9.17] | 3.75[9.53] | 55761[248] | 13.5[87.3] | 4119[28.4] | | |

Table 3-3. Unit compressive strength test result

### 3.2.5 Flexural test on unit brick

To determine the modulus of rupture for unit brick, unit brick flexural tests were carried out for five unit bricks. The following table shows the measurement on each unit for the test. Unit bricks are placed on a simple support steel plate consisting of one pinned side and one roller side. Vertical load in compression increasingly acts from the MTS machine through an inch wide steel plate until the brick fails in flexure as shown in the following Figure 3-18.

Figure 3-18. Unit flexural test

The obtained modulus of rupture for unit bricks is listed in the Table 3-4 below

| Modulus of Rupture (Flexural Test)-ASTM C67-12-Section 6 | | | | | | | |
|---|---|---|---|---|---|---|---|
| | d(in)[cm] | x(in)[cm] | W (lb)[kN] | $L_{whole}$ (in) | L (in) | S(psi) [MPa] | $S_{average}$ (psi)[MPa] $S=3W(L/2-x)/bd^2$ |
| B1 | 2.36[5.99] | 0.13[0.33] | 2253[10] | 7.70[19.6] | 7.0[17.78] | 1096[7.56] | 850[5.86] |
| B2 | 2.34[5.94] | 0.10[0.25] | 1642[7.3] | 7.64[19.4] | 7.0[17.78] | 816[5.63] | |
| B3 | 2.34[5.94] | 0.63[1.6] | 1913[8.51] | 7.63[19.38] | 7.0[17.78] | 809[5.78] | |
| B4 | 2.35[5.96] | 0.55[1.38] | 1571[6.99] | 7.60[19.3] | 7.0[17.78] | 666[4.59] | |
| B5 | 2.34[5.94] | 0.10[0.25] | 1735[7.72] | 7.63[19.38] | 7.0[17.78] | 862[5.94] | |

Table 3-4. Modulus of Rupture from Unit Flexural Test

### 3.2.6 Mortar

The United States uses cement-lime, mortar cement, and masonry cement types of mortars for most of the masonry structures, these types of mortars are the same for Mexico and Chile codes. Table 3-5 and Table 3-6 below list the mortar mix proportional and nominal compressive strength used in CM structures according to the NTC-M, 2004 Mexico Code (NTC-M, 2004) and according to ASTM C270 (ASTM, 2005), respectively.

| **NTC-M, 2004 (NTC-M, 2004)** | | |
|---|---|---|
| **Cement types** | Type of Mortar | Minimum Specified Compressive Strength at 28 Days (MPa)[(psi)] |

| | | |
|---|---|---|
| **Hydraulic Cement** | I | 12.5[1800] |
| | II | |
| | III | |
| **Masonry cement** | I | 7.5[1088] |
| | II | |
| | III | |
| **Hydrated lime** | I | 4 |
| | II | |
| | III | |

**Table 3-5. Mortar mix proportions used in confined masonry based on Mexico standards**

| **ASTM C 270 (ASTM, 2005)** | | | |
|---|---|---|---|
| **Cement types** | Type of Mortar | Minimum Specified Compressive Strength at 28 Days (psi) | Minimum Specified Compressive Strength at 28 Days (MPa) |
| **Cement- lime** | M | 2500 | 17.2 |
| | S | 1800 | 12.4 |
| | N | 750 | 5.17 |
| **Mortar cement** | M | 2500 | 17.2 |
| | S | 1800 | 12.4 |
| | N | 750 | 5.17 |
| **Masonry cement** | M | 2500 | 17.2 |
| | S | 1800 | 12.4 |
| | N | 750 | 5.17 |

**Table 3-6. Mortar mix proportional and compressive strength based on the American standards**

It has been known that stronger mortar performs more brittle, while weaker mortar tends to dissipate energy better. It is essential for researchers and designers to review carefully and choose appropriate mortar type according to the location of the design. In this project, the average strength type N mortar is thus chosen to use. The compression test verifying the mortar strength is listed in the following section.

### 3.2.7 Compression tests on mortar cubes

The type N premixed mortar used in constructing prisms and wall panels was tested in compression using 2-inch cubes to verify the strength characteristics of the mortar. Cubes are tested at 28 day old according to ASTM C109-12. The loading rate set for this test was 0.0001 in/s, gradually increasing until the failure crushing pattern was found on the specimens as seen in the following Figure 3-19. Three cubes were tested at 28 days. Shown in Figure 3-20 below is the result for two cubes, test data for the third one at 28 days old and the three extra cubes tested at 100 days old were not valid. The machine failed to capture a correct displacement readings from the test, thus the strain measurement data seemed too small to be acceptable. However, the compressive strength for six cubes agrees with one another at 1200 psi. The result for the three mortar cubes tested at 100 days old was listed in the subsequent Figure 3-21.

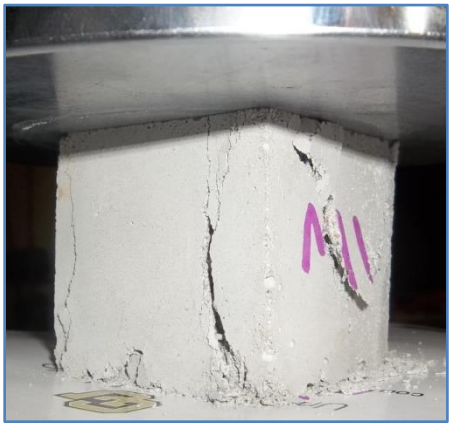

**Figure 3-19. Mortar cube undergoes compression**

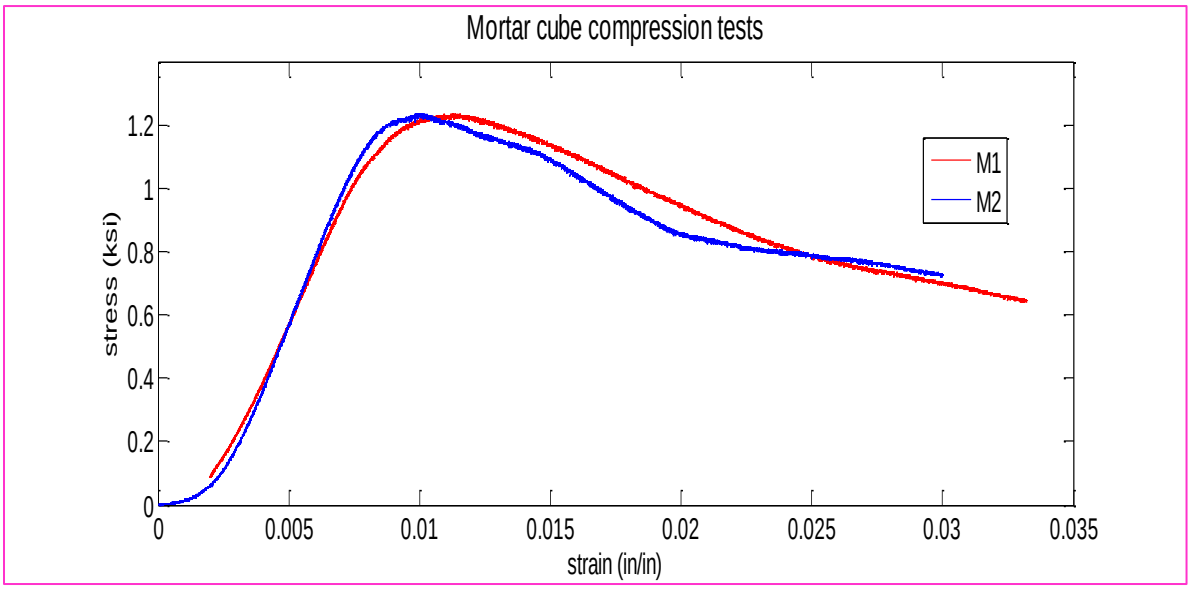


Figure 3-20. Mortar test at 28 days old

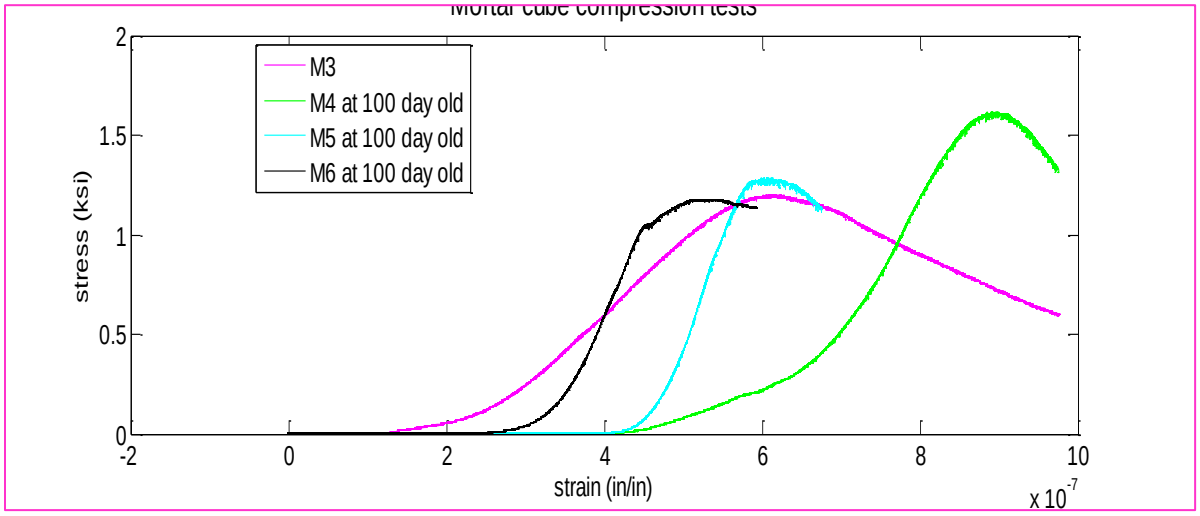


Figure 3-21. Mortar test at 100 days old

### 3.2.8 Compressive strength in concrete-confining elements

Concrete used for confining elements in CM structures is required to have a minimum compressive strength of 3000 psi [20.68 MPa] based on cylinder testing seen in Figure 3-22. The third cylinder from the same concrete batch was broken during the test setup, thus shown in Figure 3-22 are data for only two cylinder tests. As mentioned previously in the mortar section,

the component selection has to be consistent and compatible with the location of the design to better achieve the overall structural maximum capacity. The compatible material choices effect on structural capacity recommendations are based on study done by (Build Change, 2010). Concrete was poured onsite at the SML with the use of one ready mix load in a truck and 4 vibration applications per load, to ensure all voids were eliminated and the concrete was tightly filled to the toothed wall without breaking the cantilevered unit bricks.

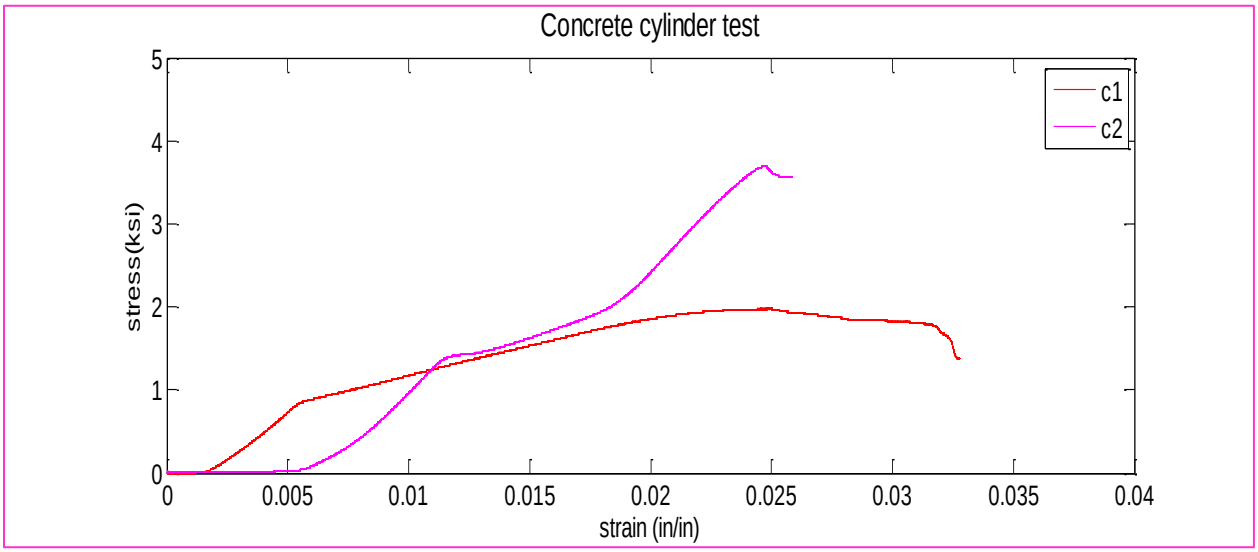


**Figure 3-22. Concrete compression test for tie elements**

### 3.2.9 Reinforcement

Reinforcing steel used in CM construction consists of deformed bars and joint reinforcement. Similar to reinforced masonry structures in the United States, deformed bars used in Mexico (the country with building codes for CM that was used mostly in this research) typically comply with either ASTM A615 or ASTM A706. ASTM A615 provides standard specification for plain carbon steel reinforcing bars that are most commonly used. ASTM A706 covers low alloy steel bars, which are used when more restrictive mechanical properties and chemical composition are required to enhance weld-ability and provide closer control of tensile properties.

Ties for confined elements could be either smooth or deformed steel bars. The commonly used types of joint reinforcement are placed horizontally in the mortar joints. Shown in Figure 3-23 is the smooth reinforcement bar #2 for confinement in tie elements and deformed bar #3 for longitudinal rebar used both in tie columns and tie beams. Tensile testing was not performed for reinforcement bars in this study due to the limitation of the SMT laboratory at the point of study. Specified material yield strength is 60 ksi [413.7MPa] for both axial threaded bars and smooth tie bars.

**Figure 3-23. Smooth bar #2 and Deformed bar #3**

### 3.2.10 Compressive test on prism

For structural engineers, the specified compressive strength $f'_m$ is probably the most important property for design of the masonry panel. Compressive strength $f'_m$ is the minimum compressive strength, expressed as a force per unit of a net cross-sectional area that is required by construction documents. For CM, the design $f'_m$ should preferably be determined by testing prism specimens made of the masonry units and mortar (seen in Figure 3-24). The masonry materials used in the experimental program were tested in compression to obtain properties used in numerical modeling. According to ASTM C1314-12, five prisms consisting of three unit bricks (see Figure 3-24) were built on the same day as the masonry wall panels. Using this type of

test specimen, correction factors as mentioned in ASTM C1314-12 Table 1 were applied to determine the modulus of elasticity for masonry prisms as well as for the compressive strength of the prisms themselves. Owning the knowledge from the literature review that the prism would fail in a brittle manner as compared to mortar, the loading rate was set to 0.0001 in/s [0.00254 mm/s] to gain a better post peak behavior (including the peak after yield point, and the peak at end of the hardening point) for this type of specimen. Figure 3-25 shows the stress-strain curves for prism 2, 4, and 5 tests; data for prism 1 and 3 unfortunately showed unstable values and thus are not shown in Figure 3-25. The values $f'_m$ for prism 2, 4, and 5 after account for correction factors are 1522 psi [10.49MPa], 1628 psi [11.22MPa], and 1994 psi [13.74MPa], respectively.


**Figure 3-24. Capped Prisms**

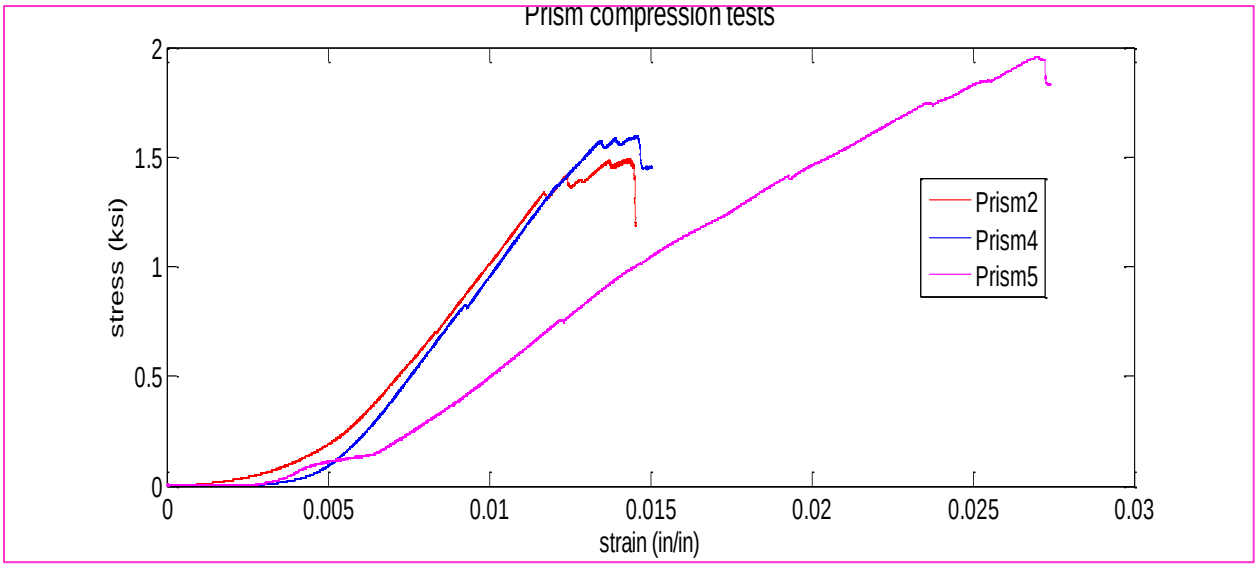


Figure 3-25. Stress-Strain curves in masonry prism

### 3.2.11 Basic shear strength test

A shear diagonal compression test for a square panel of masonry is as shown in Figure 3-26. It consists of subjecting the panel to compressive forces applied at two opposite corners along a diagonal until the panel cracks. Shear strength is inferred from diagonal compression forces based on the theoretical distribution of shear and normal stress for a homogeneous and elastic continuum.

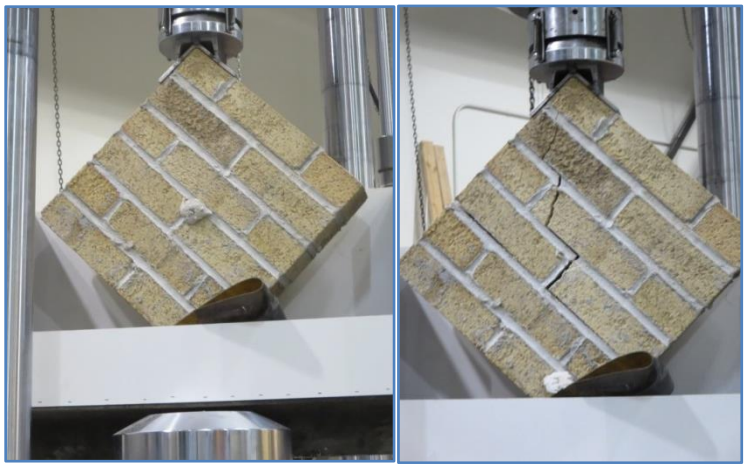

Figure 3-26. Diagonal Compressive Shear test

Because of the limitation in transporting heavy specimens and to avoid labor and cost intensive building the test set up for the shear diagonal panels, a set of five 16 in x 16 in [40.64 cm x 40.64 cm] square specimens were built according to the standards of NTC-404 (NTC-M, 2004). Two mild steel grade 60 ksi [413.67 MPa] loading shoes were designed and welded at the lab to prepare for this test. Shown in the following Figure 3-27 is the result of the test with 4 panels (panel 5 broke during transporting to the load frame), average shear strength available in a panel is 73.6 psi [0.507 MPa] (Appendix A).

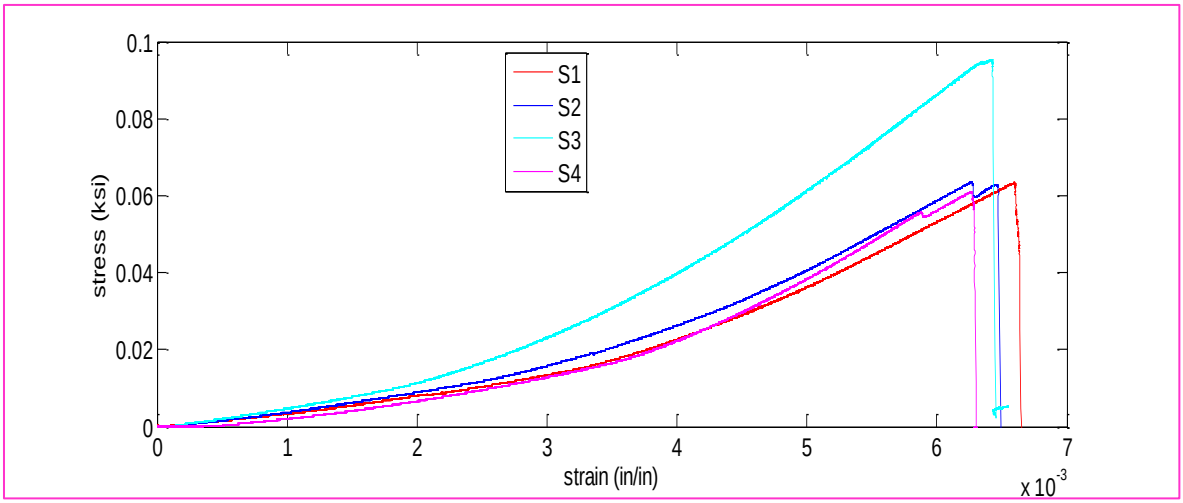


**Figure 3-27. Stress-Strain result from the diagonal compressive shear test**

### 3.2.12 Flexural tests on prism

Tensile flexural bond strength was tested by the bond wrench method of ASTM C1072. This test measures the bond strength between the unit and mortar joint in flexure by applying a combination of moment and axial force through a lever arm. Representative and constant values for all tests can be seen in the following Table 3-7.

| Average unit weight (lbf) | $P_l$ weight of loading arm without brick (lbf) | L distance from center of prism to loading point (in) | $L_l$ distance from center of prism to centroid of loading arm (in) |
|---|---|---|---|
| 5.3 | 14.9 | 16.5 | 0.75 |

Table 3-7. Bond wrench test typical values

Five prisms were built as shown in the following Figure 3-28. There were many variation factors observed in this test, the average flexural bond strength however was recorded 38 psi [0.26MPa], with standard deviation of 19 psi [0.13MPa], and coefficient of variation of 50%, as seen in Table 3-8.

Figure 3-28. Bond wrench test

| Joint # | P applied load (lbf) | b width (in) | d depth (in) | $F_g$ gross area flexural tensile strength (psi) |
|---|---|---|---|---|
| **1** | 75.2 | 7.64 | 3.65 | 71 |
| **2** | 26.8 | 7.74 | 3.70 | 24 |
| **3** | 34.7 | 7.75 | 3.63 | 33 |
| **4** | 5.6 | 7.68 | 3.62 | 5 |
| **5** | 60.2 | 7.70 | 3.67 | 55 |
| **6** | 67.4 | 7.73 | 3.64 | 63 |
| **7** | 46.1 | 7.69 | 3.73 | 41 |
| **8** | 73.3 | 7.70 | 3.65 | 68 |
| **9** | 47.1 | 7.67 | 3.70 | 43 |
| **10** | 24.9 | 7.71 | 3.71 | 22 |
| **11** | 24.5 | 7.64 | 3.68 | 23 |
| **12** | 27.8 | 7.66 | 3.69 | 26 |

| Joint # | P applied load (lbf) | b width (in) | d depth (in) | $F_g$ gross area flexural tensile strength (psi) |
|---|---|---|---|---|
| **13** | 34.7 | 7.70 | 3.69 | 32 |
| **14** | 52.0 | 7.71 | 3.62 | 49 |
| **15** | 27.5 | 7.65 | 3.73 | 25 |
| **16** | 26.2 | 7.66 | 3.64 | 25 |
| | | | **Average (psi)** | 38 [0.26MPa] |
| | | | **Standard Deviation** | 19[0.13MPa] |
| | | | **Coefficient of Variation** | 50% |

**Table 3-8. Bond wrench test result**

## 3.3 In plane test on CM walls

### 3.3.1 Test ppparatus and setup

Figure 3-29, Figure 3-31, and Figure 3-31 show the braced frame comprised of steel braces contacting the sides of the wall with a Teflon fabric interface used to minimize friction. This brace is to assure no out of plane movement and torsion occur during testing, and the shear wall will only be loaded in-plane. The Teflon interface ensures in-plane behavior without adding resistance due to friction. The setup for out of plane bracing can be seen in the following drawing and the actual test set up in the lab.

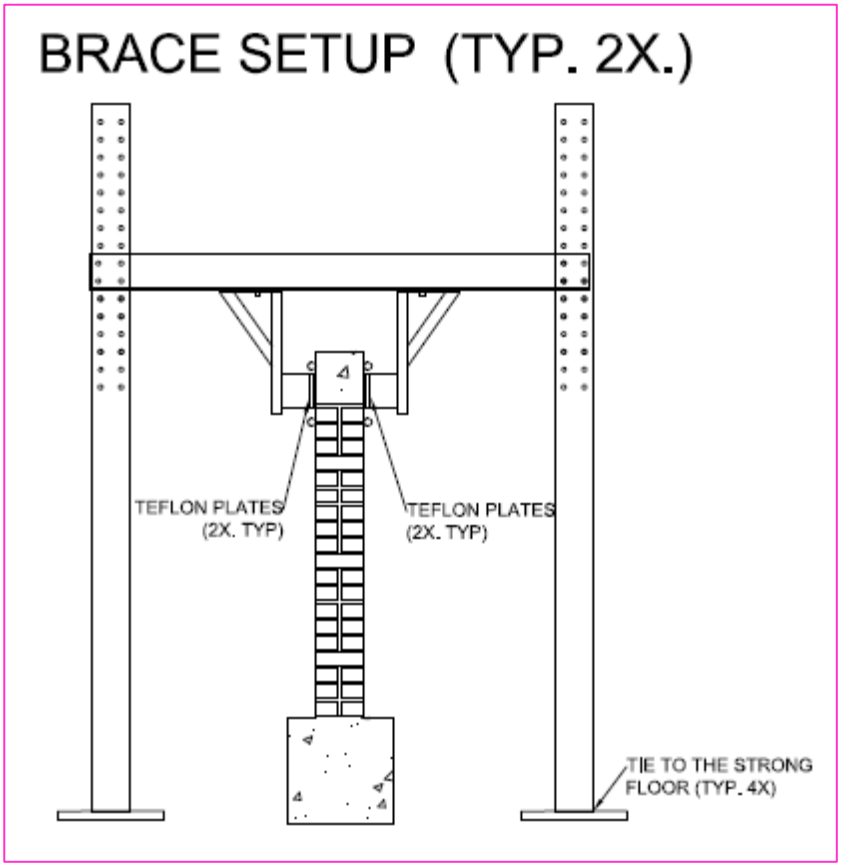


**Figure 3-29. Lateral brace frame**

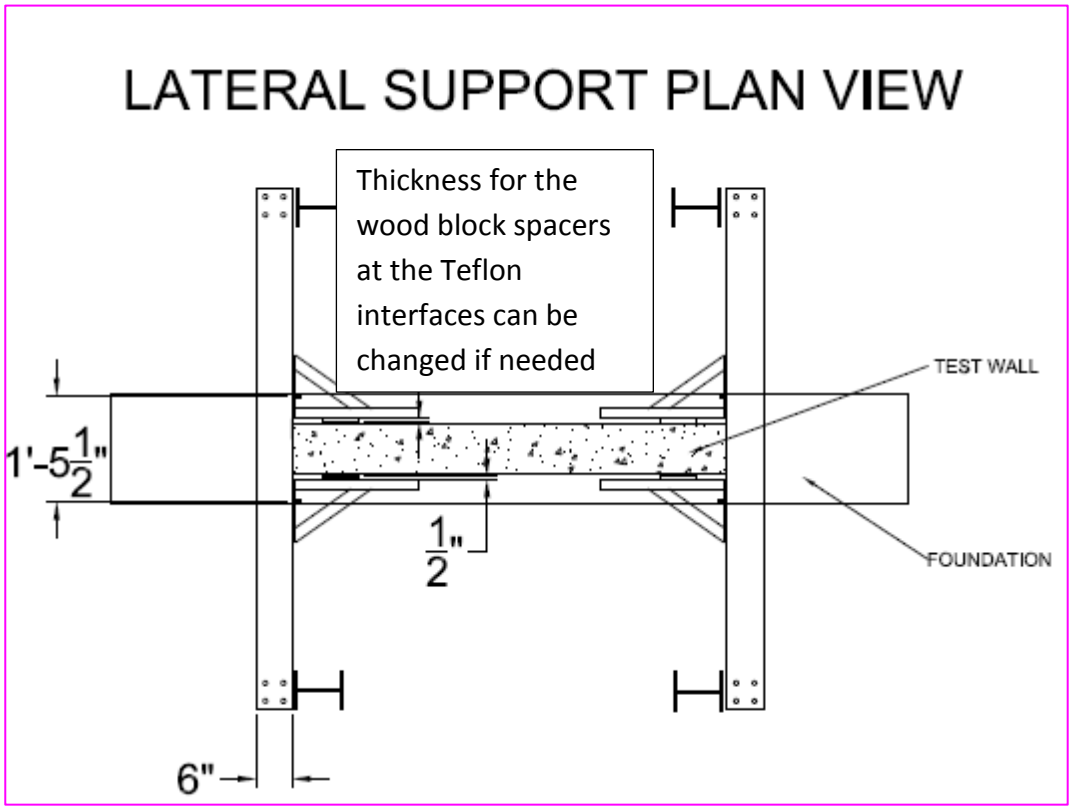


Figure 3-30. Lateral brace plan view

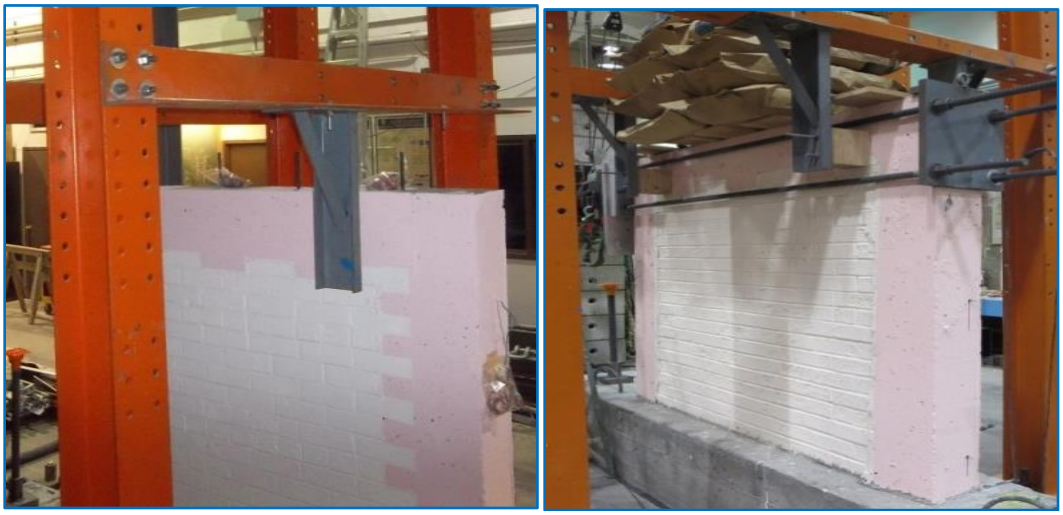

Figure 3-31. Lateral brace set up

The actuator head was attached to the end of the tie beam while the base of the actuator was attached to the reaction wall. The actuator was supported using a double pulley system and

two counter weights to ensure that the applied load purely acts laterally. The reaction wall is rigid and designed not to move during tests via the 90 kip posttensioning force on each bolt connecting the red I beam attached to the reaction wall and the end of the actuator. Figure 3-32 and Figure 3-33 show the complete counter weight assembly, the connection at loading point, and the rigid connection at the end of actuator to the red I beam and the reaction wall.

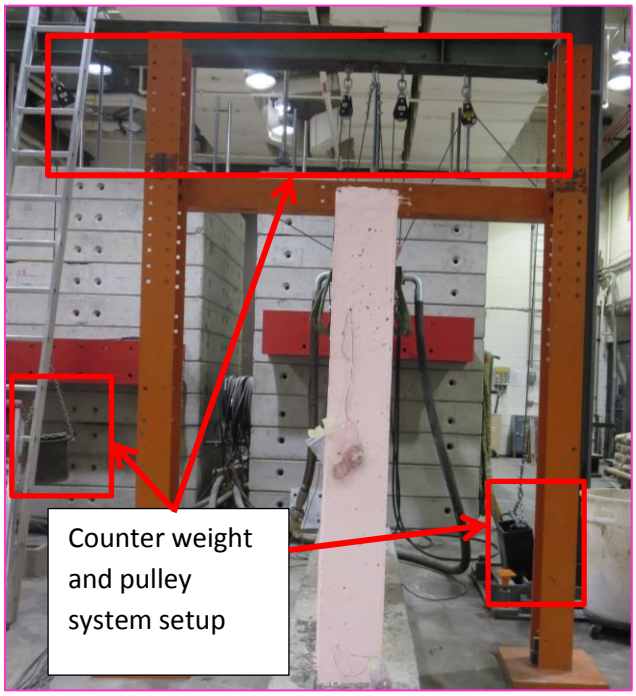


Figure 3-32. Counter weight and double pulley setup

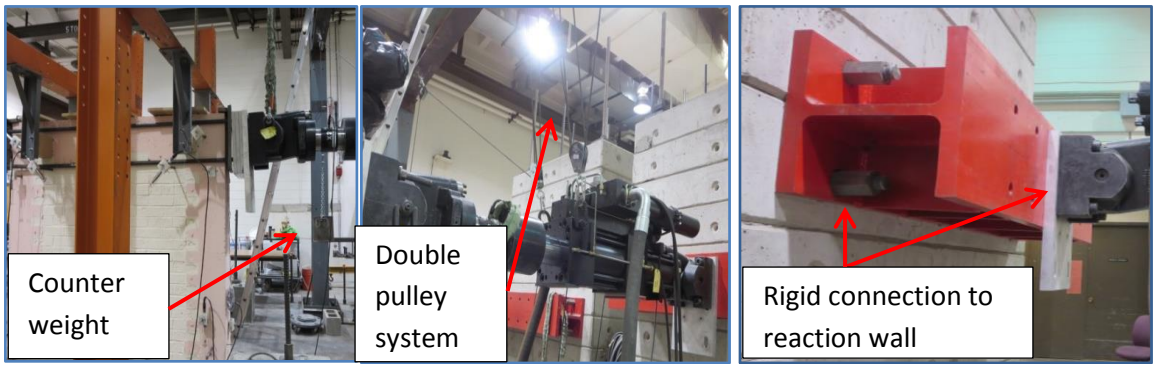


Figure 3-33. Counter weight setup, cap connection, and end connection

### 3.3.2 Instrumentation

The specimens were also instrumented with LVDTs and linear encoders to measure the movement of the specimen during the experiment, as illustrated in the following Figure 3-34 and Figure 3-35.

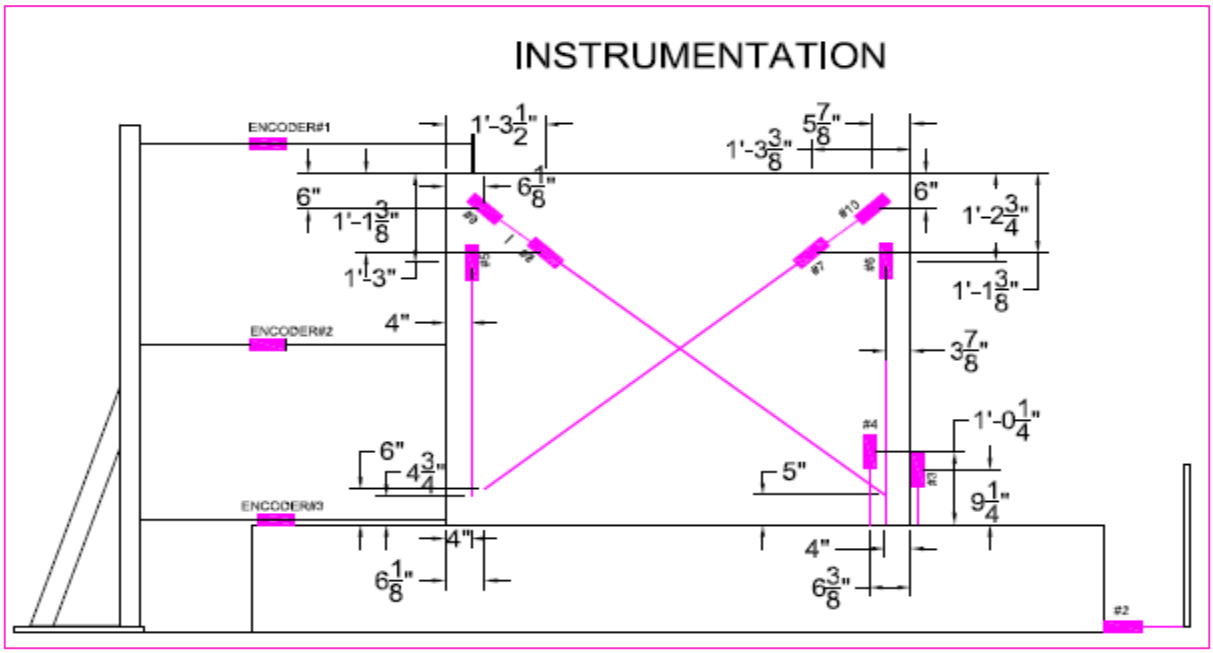


Figure 3-34. Instrumentation plan

Figure 3-35. Instrumentation

While the actuator provided the force readings and the displacement feedback, the displacements were also measured in multiple locations. The horizontal displacement at the top of the wall was measured with a linear encoder (encoder #1) placed at the tie beam level by gluing to the steel cap, and then verified using the LVDT of the actuator. Encoders were also placed at mid wall height (encoder #2) and at the level of the pedestal (encoder #3) to obtain intermediate lateral displacements or any slippage at the pedestal from the masonry interface. Sliding from the pedestal with respect to the strong floor also was measured using LVDT #2 mounted to the pedestal and the strong floor. Diagonal displacements of the wall and crack openings were measured using LVDT #8, #9, #7 and #10. The four LVDTs are placed in pairs diagonally to capture the diagonal movement of the wall panel for the concrete frame and for the masonry wall with respect to East ends of the wall and West end of the wall directions, respectively. The vertical displacement, uplift, and possible rotation at the end points of tie columns were measured using LVDT #3 and #4. Top vertical displacement on the column was measured by LVDT #5. The measurements from all of the instrumentation and equipment were recorded using the data acquisition equipment provided by the SML. The LVDT layout is illustrated in Figure 3-35 and Figure 3-36. Along with the notes taken and data recorded, the test was videotaped while noting the times of key observations. These measurements and notes were used to analyze the data and compare with estimated results.


Figure 3-36. LVDT and Encoders

### 3.3.3 Loading protocol

The load sequence for the cyclic testing is illustrated in the following Figure 3-37. The specimen was subject to increasing lateral displacements applied by a 110 kip hydraulic actuator at the tie beam. It was assumed that the lateral force was applied as a point load and evenly transferred to the specimen by the cap. The specimen was loaded at a displacement control at a rate of 0.001 inches per second [0.00254 cm/s], recording 256 force readings per second. The criteria used to end the test were predetermined as the occurrence of shear failure in the column. The loading rate was chosen so that the test is pseudo static. Literature has showed that a slower loading rate provides better accuracy in displacement measurement in a wall, and the impact effect is reduced by not using a fast loading rate (Bartolome & Quiun, 1992). As the displacements increased, failure modes became apparent and these were noted along with the corresponding load and displacement.

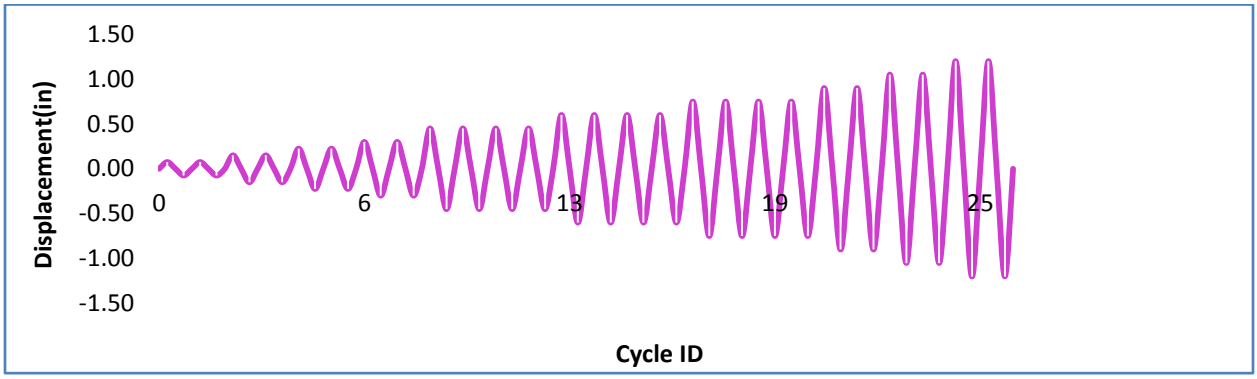


Figure 3-37. Loading protocol

### 3.3.4 Test set up

This section provides a description of half scale tests of two CM walls subjected to in-plane loading. A hydraulic MTS actuator applies lateral cyclic load to the wall by inducing pseudo static displacement incrementally increased onto top of the wall. Vertical and horizontal displacements

were monitored by 9 LVDTs mounted in the wall panel as well as by 2 LVDTs embedded in the loading actuators. In-plane loading was tested on two separate walls: one wall with a toothed configuration frame and another with a smooth configuration and rebar tied into the masonry panel. Detail drawings for these two walls can be seen in previously discussed Section 3.1, Figure 3-5, and Figure 3-7. Constant vertical load was applied on top of the wall by sand bags tightened to plywood boards to assure a roof load distribution on the wall. The purpose of using discrete sand bags is to permit the wall to behave as a free end cantilever wall (which is free to deflect on the top beam as for CM shear wall in single building houses) as seen in Figure 3-38. Strain gauges were attached to the vertical reinforcing steel with the intention of measuring the strain in the bars. Unfortunately, during the concrete pouring process, all of the strain gauges were damaged, and thus no strain data for rebar were recorded for the tests.

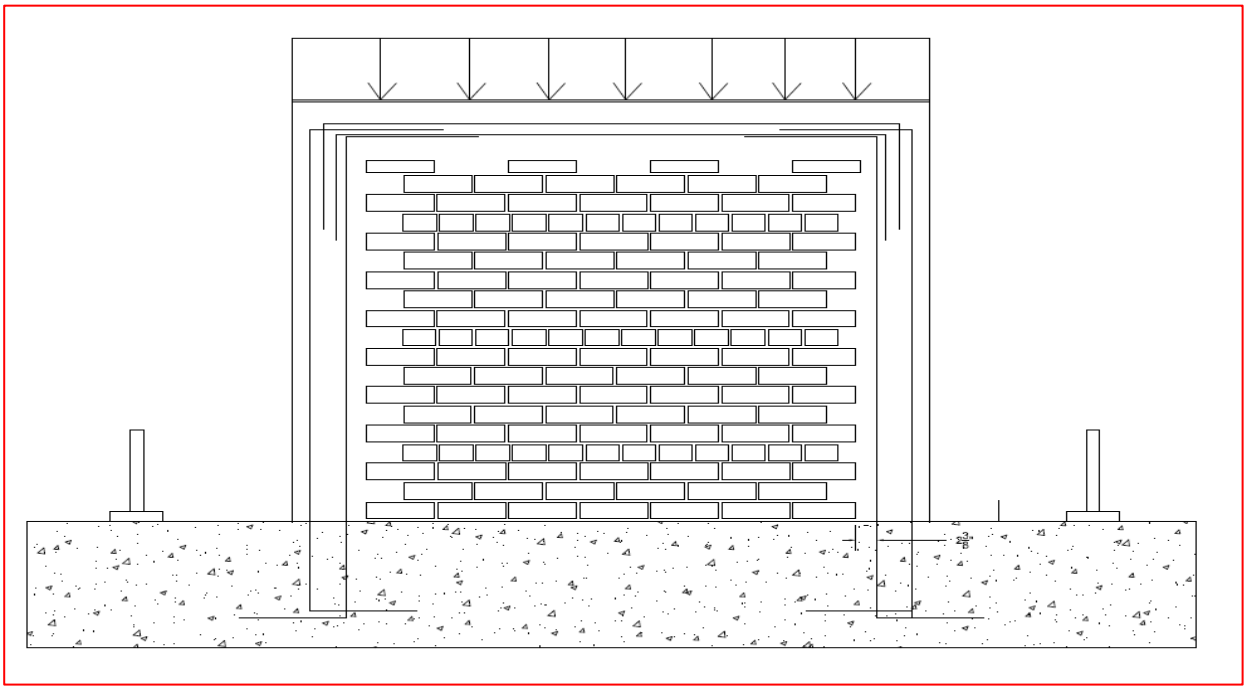

Figure 3-38. Distribute roof load

Shown in Figure 3-39 and Figure 3-39 are the sketches of how the test was set up including the layout of the testing space in CU structural lab. Each hole on the strong floor shown in the drawings is 3ft apart.

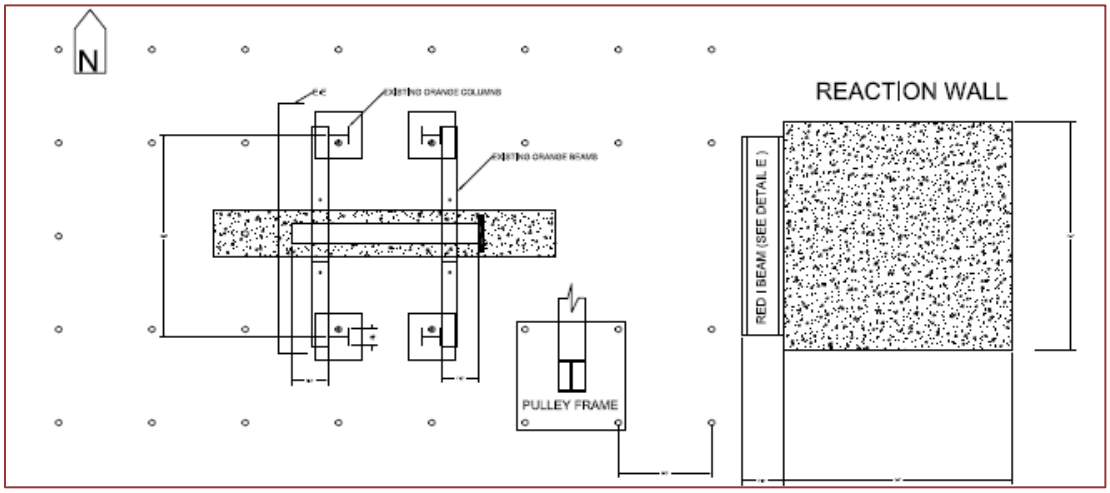


Figure 3-39. CU SML Testing layout

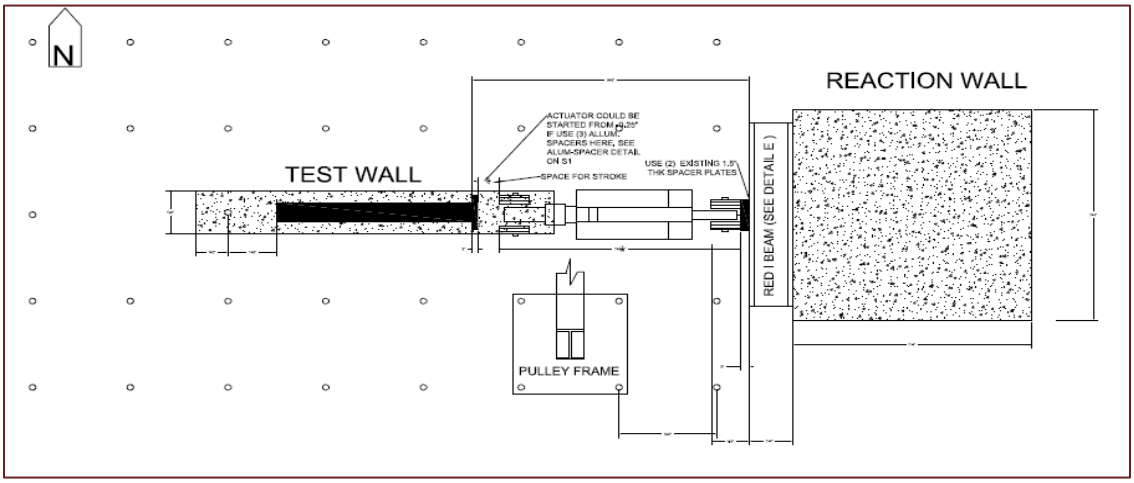


Figure 3-40. Assembly drawing for actuator setup

### 3.3.5 CM Wall 1 behavior

CM wall 1 was built with a toothed concrete tie frame cast around the unreinforced masonry panel as shown in the following Figure 3-41. Post tension was done with a force of 4kips per bolt at the connection point between steel cap and the actuator head. This post tension force at the

connection point is to ensure there is no slippage during testing. The wall was loaded at 0.001 in [0.00254 cm]/s rate for 6 continuous cycles, 0.002 in [0.00508 cm]/s for 1 cycle, 0.003 in [0.00762 cm]/s for 4 cycles, 0.005 in [0.00127 cm]/s for 3 cycles, and 0.01 in [0.0254 cm]/s for 6 cycles. Shown in the Figure 3-41 are the loading directions. The positive side denotes load towards East/pushing and the negative sign denotes load towards West/pulling.

**Figure 3-41. Test setup with sand bag as vertical roof load**

At cycle 17 when the loading rate was at 0.01in/s, the first shear crack propagated from the top right corner of the wall to the lower end of the masonry panel. This crack corresponds to the green mark drawn shown in Figure 3-42 on the wall panel and to the first red "kink" on the force-displacement curve. Loading on CM wall1 reached 39.2 kips [174.4 kN] at the first crack on the pushing/loading East direction. At the same loading rate of 0.01 in [0.0254 cm]/s, on cycle 19, the wall experienced the 2$^{nd}$ crack, shown in a red mark parallel to the 1$^{st}$ crack. The second crack formed at 40 kips [178 kN], shown on the force–displacement plot, and formed a diagonal strut with width of approximately 6 courses vertically from the first crack as seen in Figure 3-43.

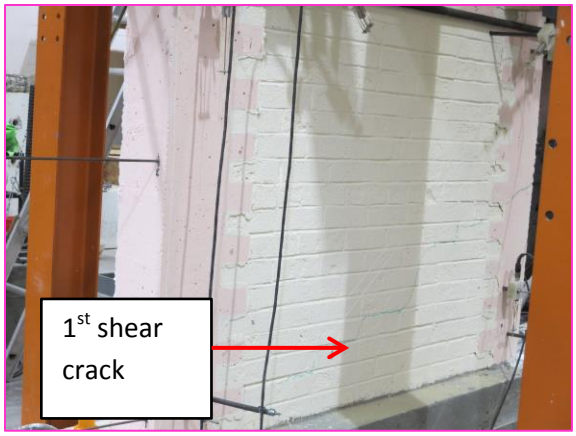


Figure 3-42. Nguyen CM Wall 1 1st shear crack

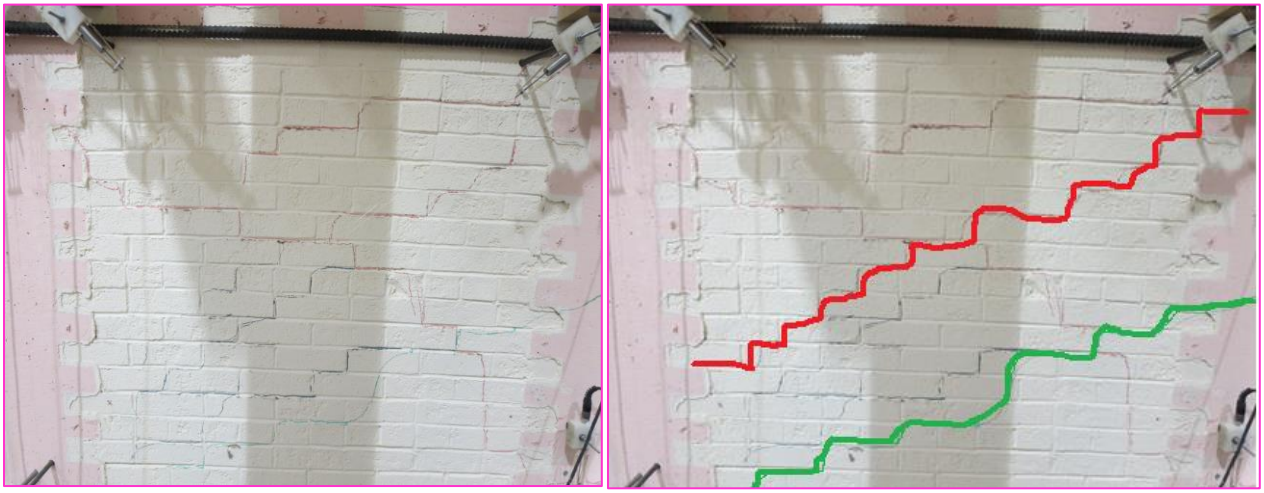

Figure 3-43. Nguyen CM Wall 1 shear cracks

In the pulling/negative/loading West direction, the wall seemed to exhibit less resistance and shear cracks formed diagonally, shown in the blue curve on the plot at 30 kips [133.45 kN]. At cycle 21 and 22, cracks formed at mid height of the tie column. Beam cracking occurred toward the end of the testing process as expected when the wall acts as a cantilever beam around maximum curvature as seen in Figure 3-44. The force resistance dropped dramatically from 42 kips [187 kN] to 30 kips [133.45 kN] at cycle 24. Shear failure occurred in the left column at a displacement of 1.5 in [3.81 cm]. At shear failure in the left column, the first crack was

measured to have a 0.5 inch [1.27 cm] opening and had completely separated away from adjacent mortar joints. Shear failure of the second column terminates the loading test. From cycle 17 to cycle 24, sliding at the base of the structure with respect to the strong floor was observed. The sliding measurement was captured by LVDT#2. 73000 points of raw data were processed using MATLAB to subtract this sliding measurement from the base of the wall with respect to the strong floor. It is important to recall here that the wall was tightened down to the strong floor at both side with a 79.2 kips [352.3kN] post tensioning force using the 1.5 inch [3.81 cm] diameter strong steel Dywidag rods as well as using fluid grout to fill in the gap between the strong floor and the lower end of the foundation. Fortunately, the sliding data was anticipated and captured by adding the instrumentation. However, future testing should consider the possible irregularity of the existing testing strong floor in the SML. The overall behavior of CM shear wall 1 can be illustrated as the following Figure 3-45.

**Figure 3-44. Nguyen CM Wall 1 experimental test result on column and beam**

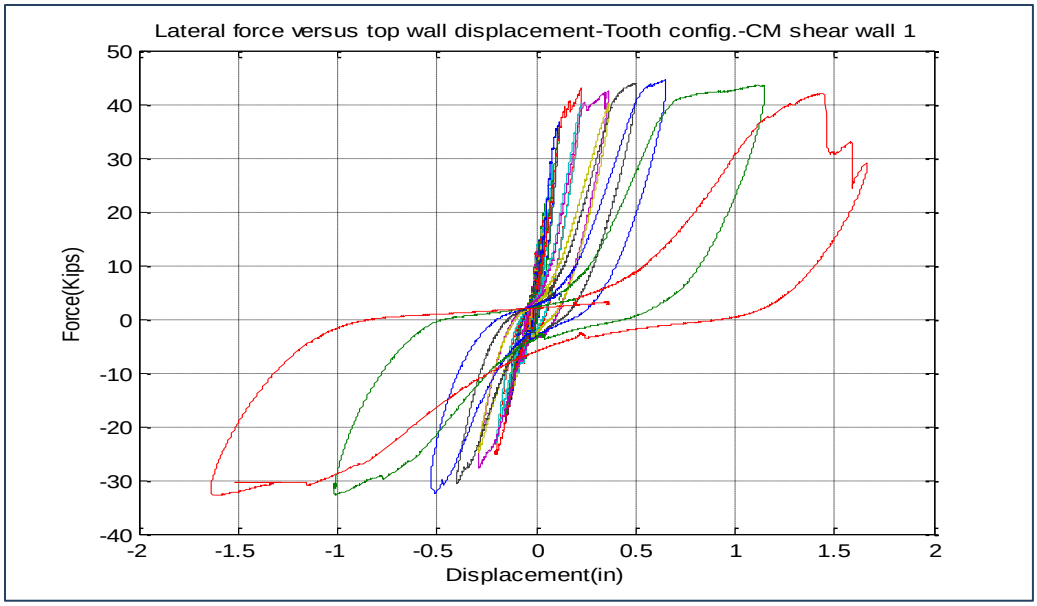


Figure 3-45. CM wall 1 force displacement hysteresis curve

### 3.3.6 CM Wall 2 behavior

CM shear wall 2 was tested 40 days after the first test with a better setup to prevent possible sliding at the foundation contact point. On both sides of the wall, post tensioning force was added as the same 79.2 kips [352.2 kN] in each Dywidag rod. A steel member was used as bracing on the West end of the wall to the reaction wall. On the East side of the wall, a stiffened I beam steel member was post tensioned down to the strong floor at 88 kips on each end of the member as shown in the Figure 3-46.

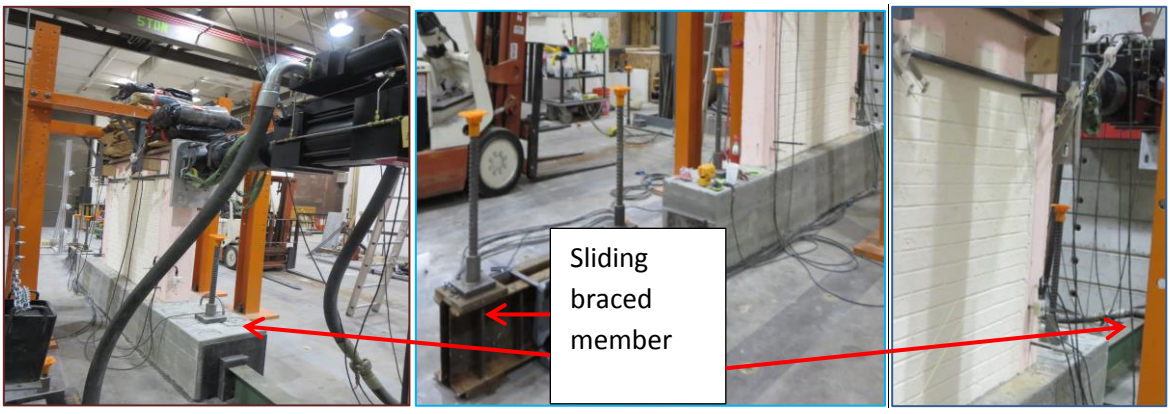


Figure 3-46. Braces to prevent sliding on both directions

The setup for test 2 in terms of instrumentation was done almost identically to the setup in CM wall 1 as seen in Figure 3-47. Testing on wall 2 was done at 0.001 in [0.00254 cm]/s for 14 continuous cycles, 0.003 in [0.00762 cm]/s for 6 cycles, 0.005 in [0.0127 cm]/s for 9 cycles, 0.01 in [0.0254 cm]/s for 1 cycle, 0.02 in [0.0508 cm]/s for 2 cycles, 0.04 in [0.102 cm]/s for 4 cycles, and 0.1 in [0.254 cm]/s for 2 cycles. Duration of 10 hours of testing was performed continuously in the SML.

**Figure 3-47. Nguyen CM Wall 2 experimental test setup**

Shown in the following Figure 3-48, the first crack drawn in green occurs at cycle 16 at a 0.003 in [0.00762 cm]/s loading rate in the pulling/ loading West direction. This shear diagonal crack takes place when the wall resisted 31.7 kips [141 kN]. The second crack takes place parallel to the 1$^{st}$, shown in also in green at 34.1 kips [152 kN], reaching ultimate shear capacity at cycle 18 when the loading rate was at 0.003 in [0.00762 cm]/s. The third crack formed on the opposite side diagonally marked in black on the wall panel and at the ultimate shear strength of 35.5 kips [158 kN] at cycle 29.

Figure 3-48. Nguyen CM Wall 2 shear cracks

The test went on and cracks formed in every cycle after that. Each crack is about 5 courses of bricks parallel to the previous one. Hardening in the wall was experienced and illustrated in the following force-displacement curve after an overall displacement of 1.25 in [3.175 cm]. The right column sheared off at 36.6 kips [162.8 kN] at the 31st cycle when loading was at 0.005 in [0.0127 cm]/s. The left joint experienced failure in CM wall 2 at cycle 27; this did not occur in wall 1. The left column sheared off at cycle 35, at 29.4 kips [130.8 kN]. 90000 points of raw data were processed using MATLAB for this wall. The overall lateral displacement in the smooth wall with steel reinforcement is 3 inches and is shown in the Figure 3-49. The test was terminated to be consistent with the predetermined shear failure of column as in test 1. However, the hardening in steel shows clearly on the last 3 cycles by the continuing increase in slope as shown in the Figure 3-49.

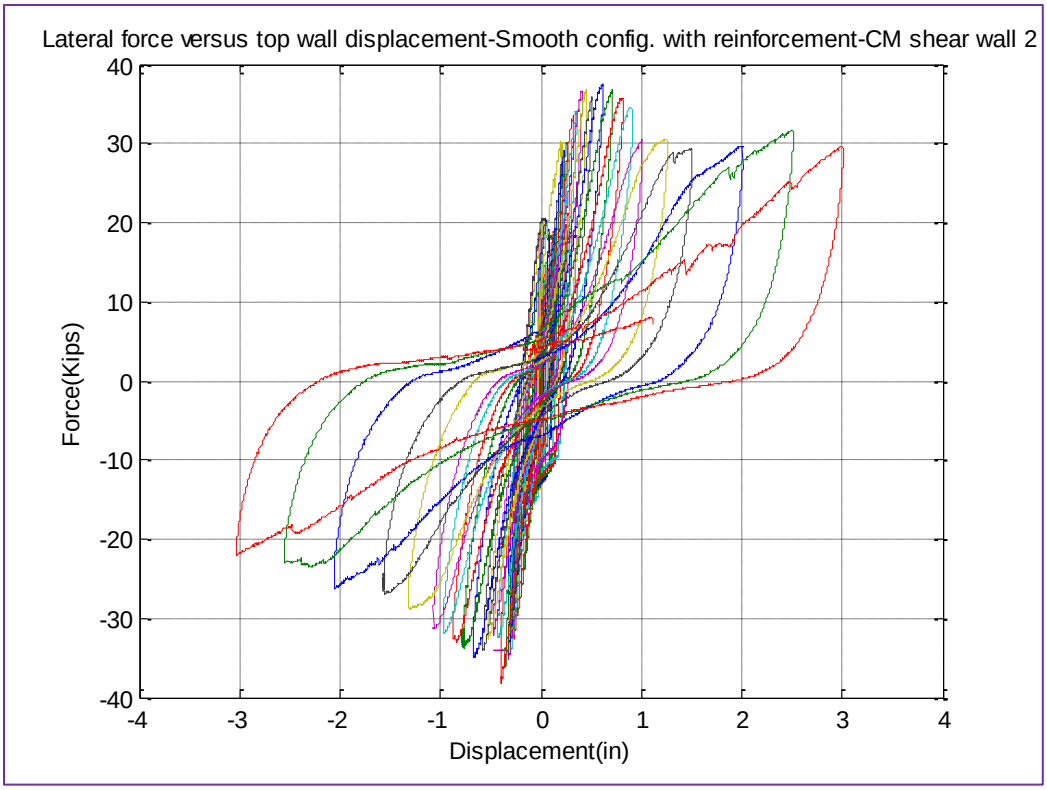


**Figure 3-49 Nguyen CM Wall 2 force displacement hysteresis curve**

## 3.4 In plane test results on CM walls

### 3.4.1 Force versus displacement comparison

Maximum lateral resistance force and horizontal displacement are plotted in the Figure 3-50 for both walls. As seen in this Figure 3-50, the tie frame concrete with a toothed configuration provides stronger shear strength in the CM wall. This is due to the shrinkage force with extra surface area bonding from the concrete frame to the wall panel. This shear strength difference is measured at the first crack, where the wall is considered to have ended its elastic behavior. The magnitude of difference in shear strength is up to 7.00 kips [31.14kN] which is approximately 20% of the wall's shear strength. While in the smooth wall configuration with dowel reinforcement, the ductility improves, this is shown by the lateral displacement improvement of 1.12in [2.85cm]. Drift ratio is calculated for both walls as a ratio of lateral displacement from yield point to

complete failure to wall height. In wall 1, the drift ratio is 2.39% while in wall 2 the drift ratio is 4.79%.

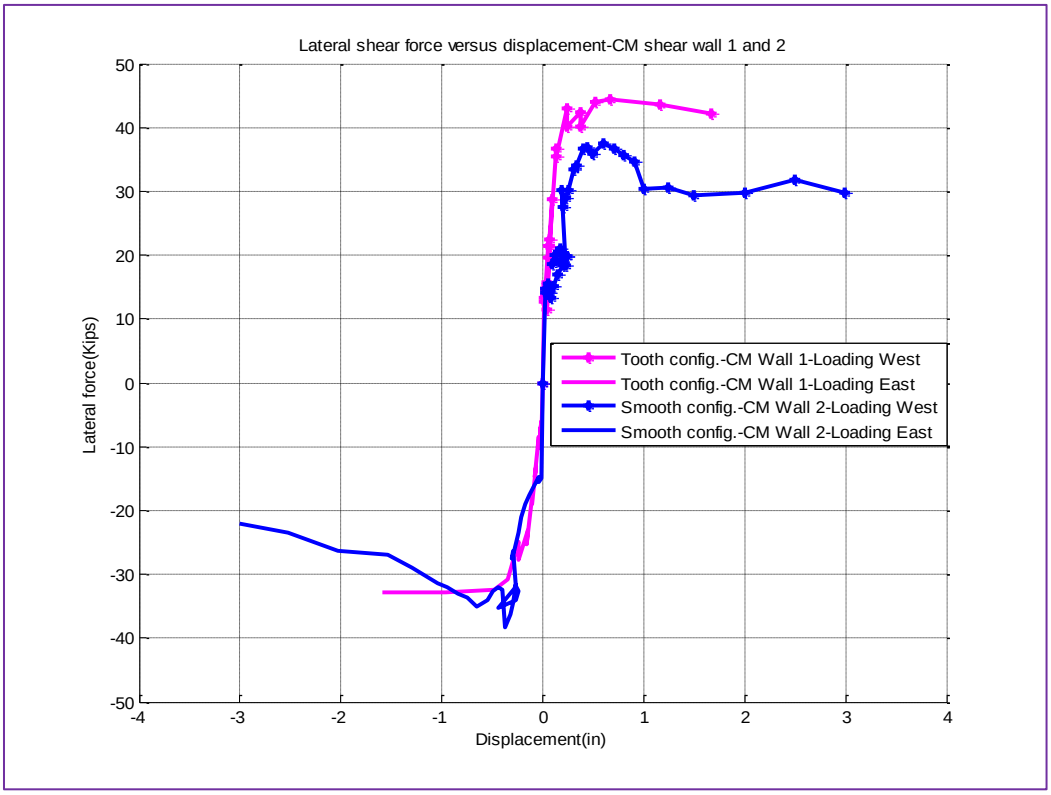


**Figure 3-50. Maximum force and displacement on 2 CM walls**

Plotted in black on the Figure 3-51 is the allowable displacement according to the MSJC 2011 for URM shear wall. As seen in this Figure 3-51, the Code value is at maximum displacement of the CM shear wall. As compared to CM wall 1, the code displacement is about 30% of the overall displacement on the wall. On CM wall2, the allowable code displacement is about 20% of the overall displacement on the wall as seen in Figure 3-51. On this figure, the ultimate displacements for CM wall 1 and 2 are plotted in red and cyan, respectively.

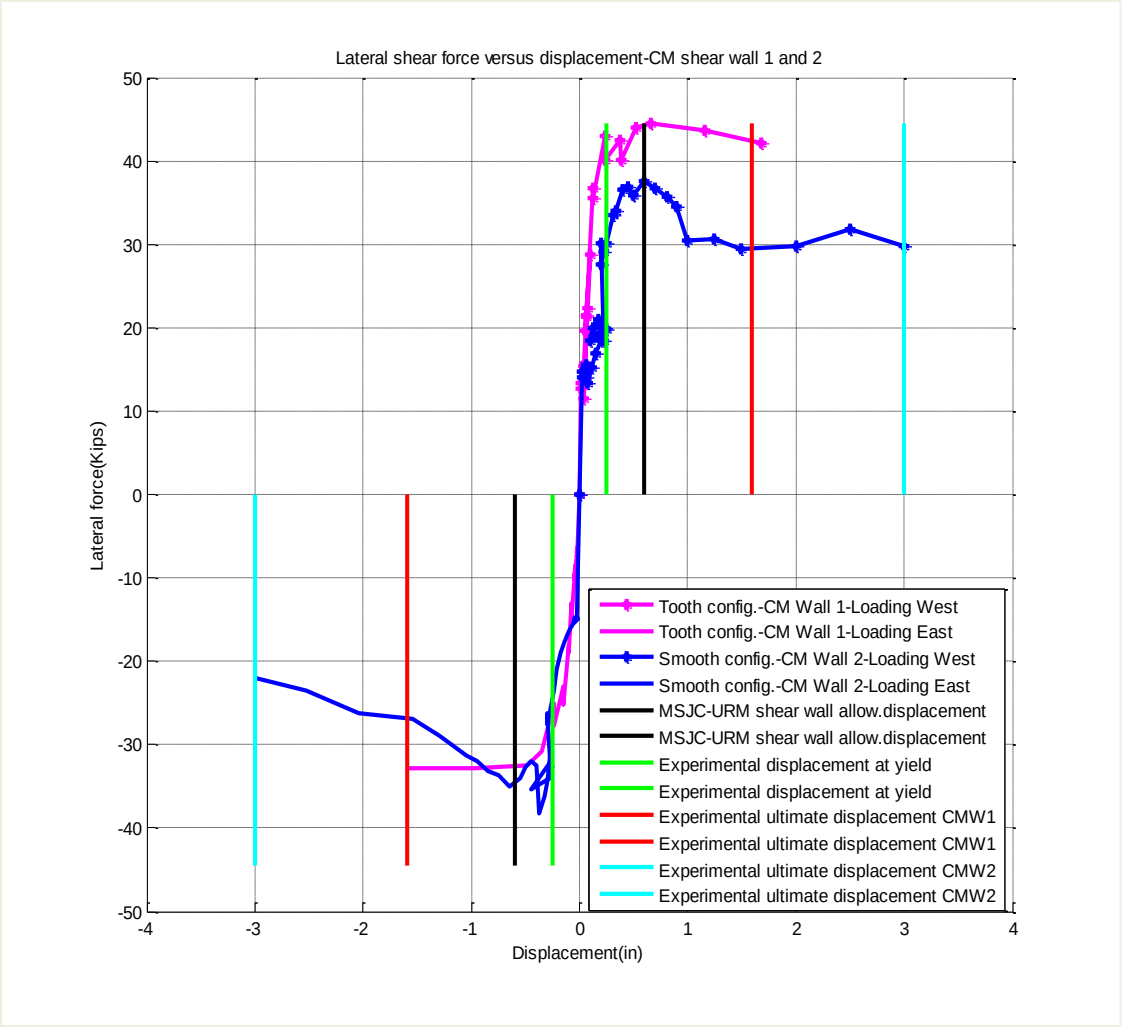


**Figure 3-51. Code value for allowable displacement on URM**

Plotted in green on Figure 3-52 and Figure 3-53 is the maximum shear strength according to the EERI 2011, NTC-2004, and in black MSJC for a CM shear wall and for URM shear wall, respectively. As seen in Figure 3-52 and Figure 3-53, the CM shear strength value is at the maximum shear strength of CM shear wall 1 in the West loading direction. As compared to CM wall 1 in the East loading direction, and maximum shear strength values on both loading directions of CM wall 2, the code shear value is about 7 kips less than CM wall 2 and 12 kips less than CM wall 1 in the pushing direction. The MSJC values for URM shear wall capacity is the most conservative value as seen in Figure 3-25 and Figure 3-53.

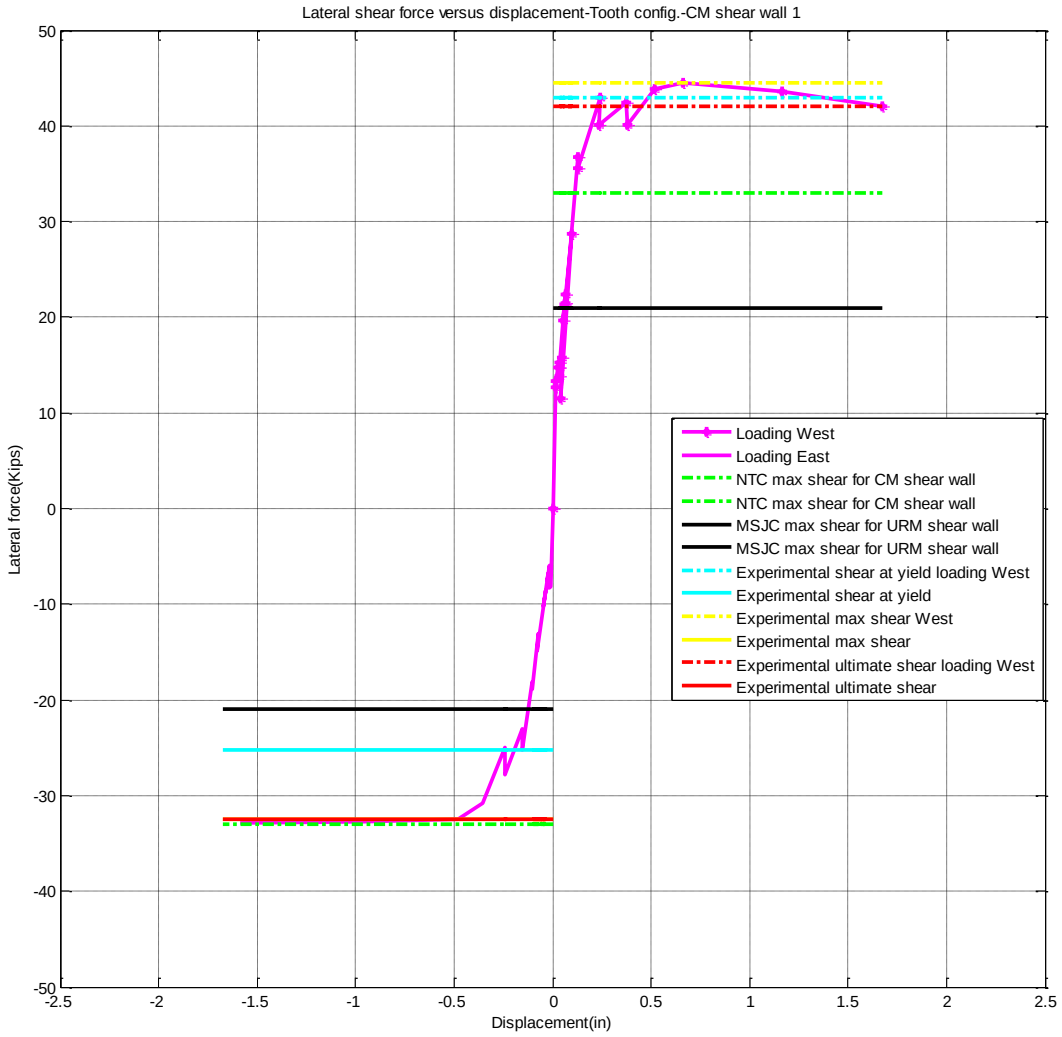


**Figure 3-52. Code shear force values comparison for CM wall 1**

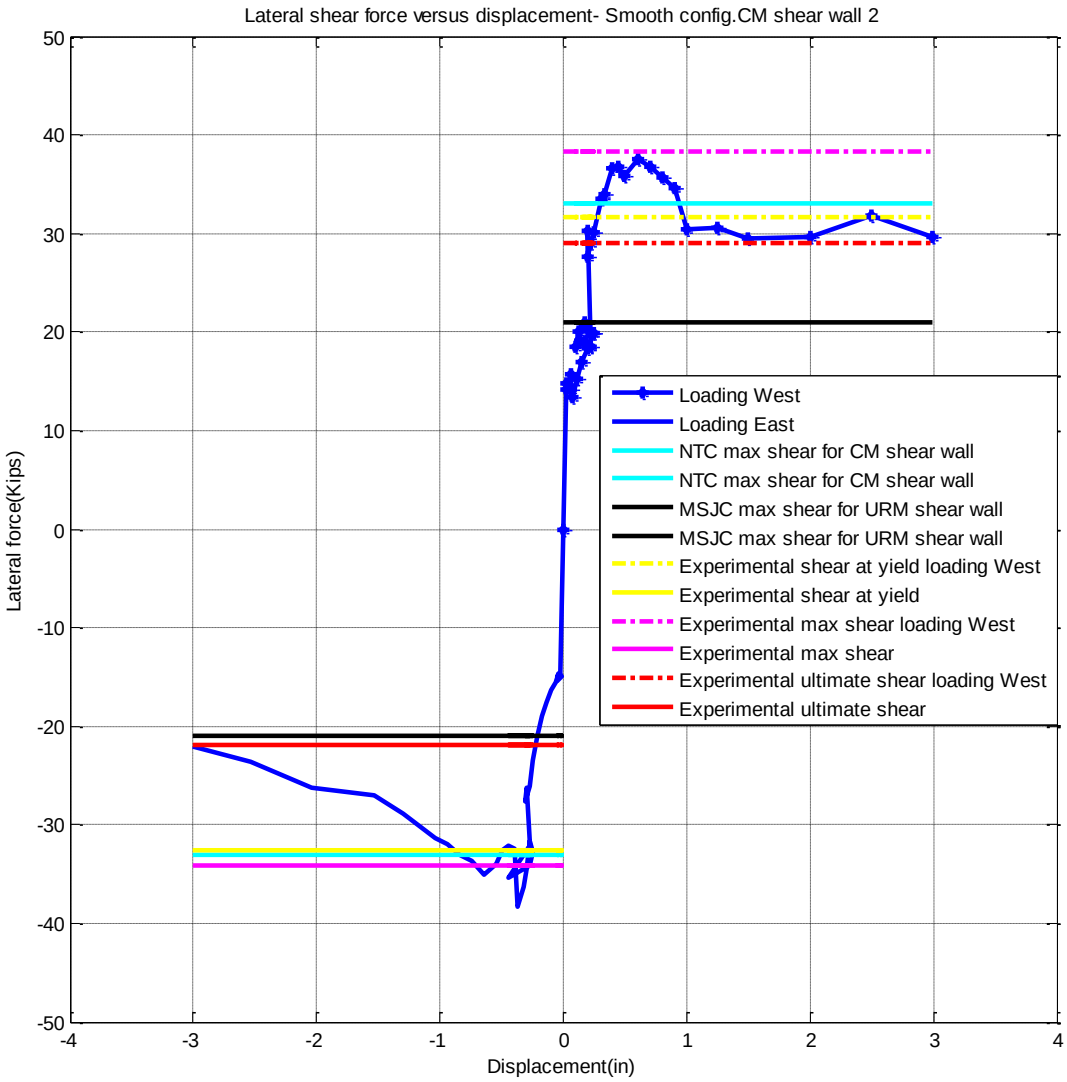


**Figure 3-53. Code shear force values comparison for CM wall 2**

### 3.4.2 Wall to tie element interface separation comparison

In both walls, the diagonal movement of the masonry wall panel with respect to the diagonal movement of the concrete tie elements was measured and plotted in the following Figure 3-54 and Figure 3-55. Shown in pink is the maximum diagonal displacement of the masonry wall panel at each cycle, while black shows the maximum diagonal displacement of the concrete frame. The

comparison cannot be made for the East direction loading due to the instrumentation of wall 1 malfunctioning during the test. For the West direction loading, one can see that the smooth masonry wall panel separated away from the concrete much earlier as compared to CM wall 1 with the toothed configuration. Once the separation takes place during the plastic region, under the same lateral force, the masonry wall panel seems to lose its resistance faster than the concrete frame, or the unit brick at the instrumentation point must be separated, therefore we see the pink curve has more displacement. This is somewhat unintuitive, but the consistency is apparent in both plots.

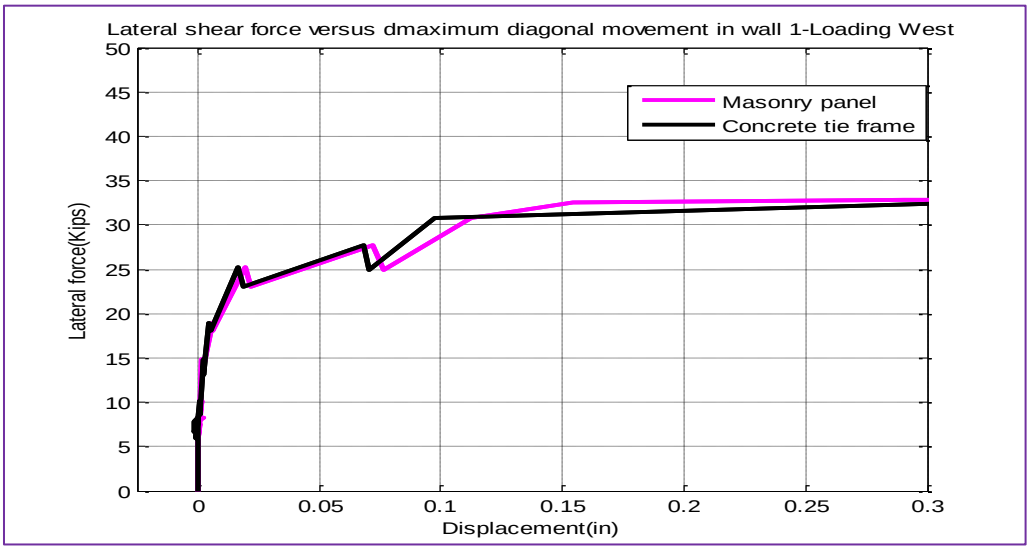


**Figure 3-54. Diagonal movement in CM wall 1 panel and surrounding tie element**

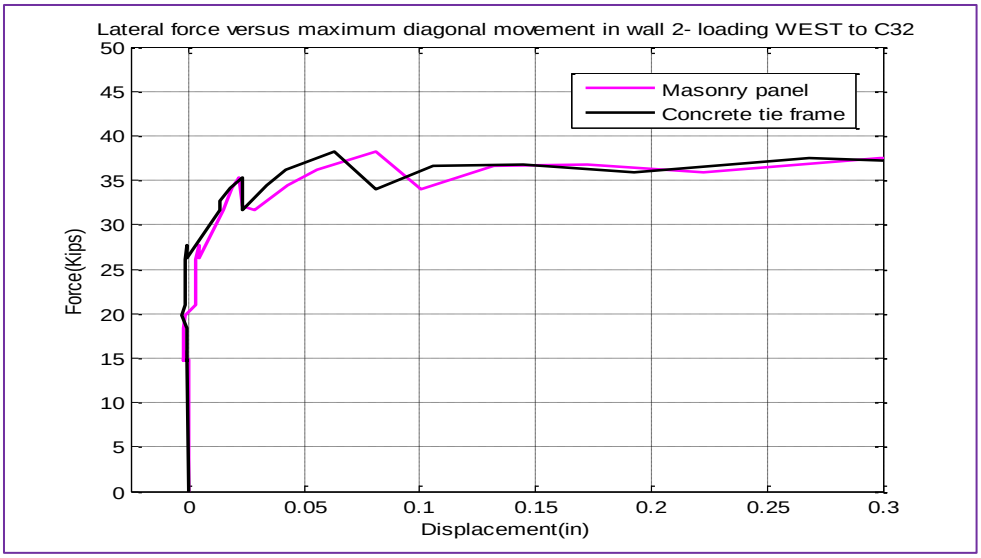


**Figure 3-55. Diagonal movement in CM wall 2 panel and surrounding tie element**

### 3.4.3 CM shear wall failure mechanism versus RCMI failure mechanism

In addition, it is important to note that the failure mechanism that occurred in both tests is different than all the failure mechanisms listed for reinforced concrete masonry infill walls. Shown below are the three failure mechanisms that (Mehrabi, Shing, Schuller, & Noland, 1994) observed on the structural performance of 14 half-scale single story RC frames masonry infill tested under in-plane loads. The RC frames had either a ductile or non-ductile design with two types of infill panels. One consisted of hollow concrete block weak infill and the other had solid concrete brick strong infill. Both panel types significantly increased the strength and stiffness of an RC frame. Failure mechanism 1 shown in Figure 3-56 is a frame with a weak infill tended to exhibit a relatively ductile behavior dominated by the sliding within the masonry bed joints over the height of the wall and the flexural yielding in the columns. This mechanism could also occur in a strong infill bounded by a relatively strong and ductile RC frame. Failure mechanism 1 shown in Figure 3-57 is characterized by a diagonal crack initiating in the infill near the loading point, the masonry wall panel then loses its resistance and the crack propagates to the adjacent RC column,

eventually shearing the column off. (Mehrabi, Shing, Schuller, & Noland, 1994) describe this as a brittle mechanism associated with a significant drop of the load carrying capacity, and it normally occurred in non-ductile RC frames with strong masonry infill. In the case of a strong RC frame, a third mechanism characterized by masonry infill corner crushing, as shown in Figure 3-58, could occur, as well as plastic hinge forming in the RC column (Mehrabi, Shing, Schuller, & Noland, 1994) and (Stavridis & Shing, 2010).

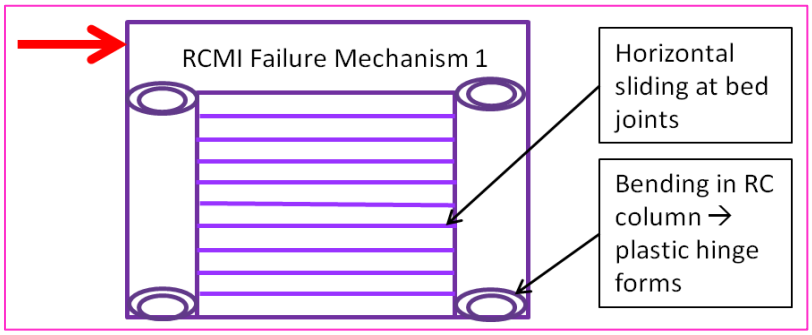


**Figure 3-56. RCMI failure mechanism 1**

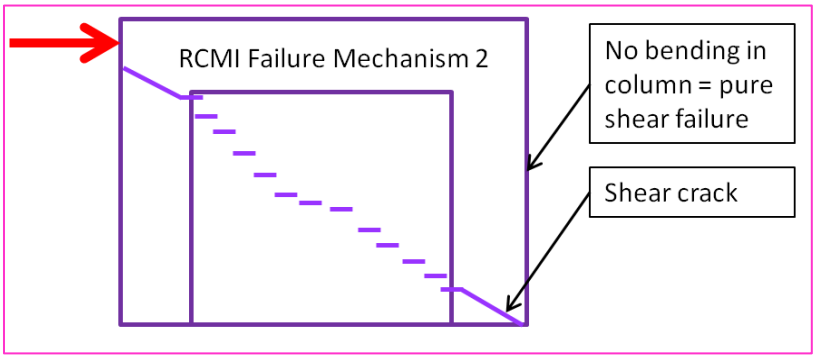


**Figure 3-57. RCMI failure mechanism 2**

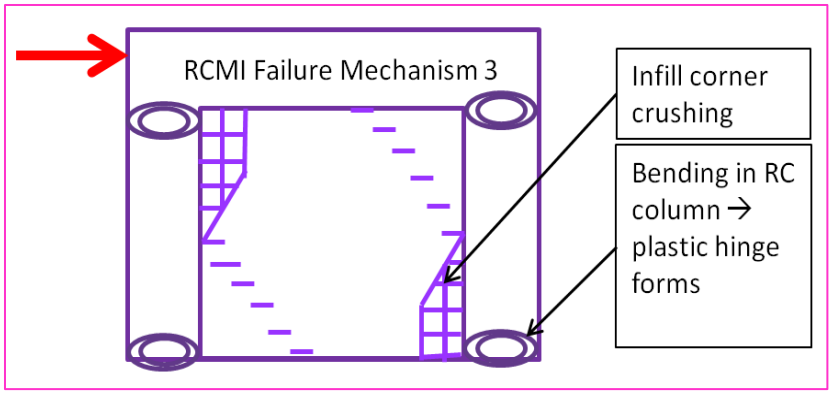


**Figure 3-58. RCMI failure mechanism 3**

For CM, after yielding, the masonry reaches its compressive strength at the compressive corner and a plastic hinge forms the adjacent column. The masonry panel and the surrounding frame act as a cantilever beam and move as one piece together. The column on the tensile side cracks due to bending, a shear crack propagates from the loaded column side, through the masonry panel, the column on compressive side bends first, then is finally subjected to shear crack failure. This failure mechanism is almost like a combination of RCMI failure mechanism 3 and 2 without the separation or crushing in masonry infill panel as seen in Figure 3-59 and Figure 3-60.

Figure 3-59. CM shear wall 1 failure mechanism

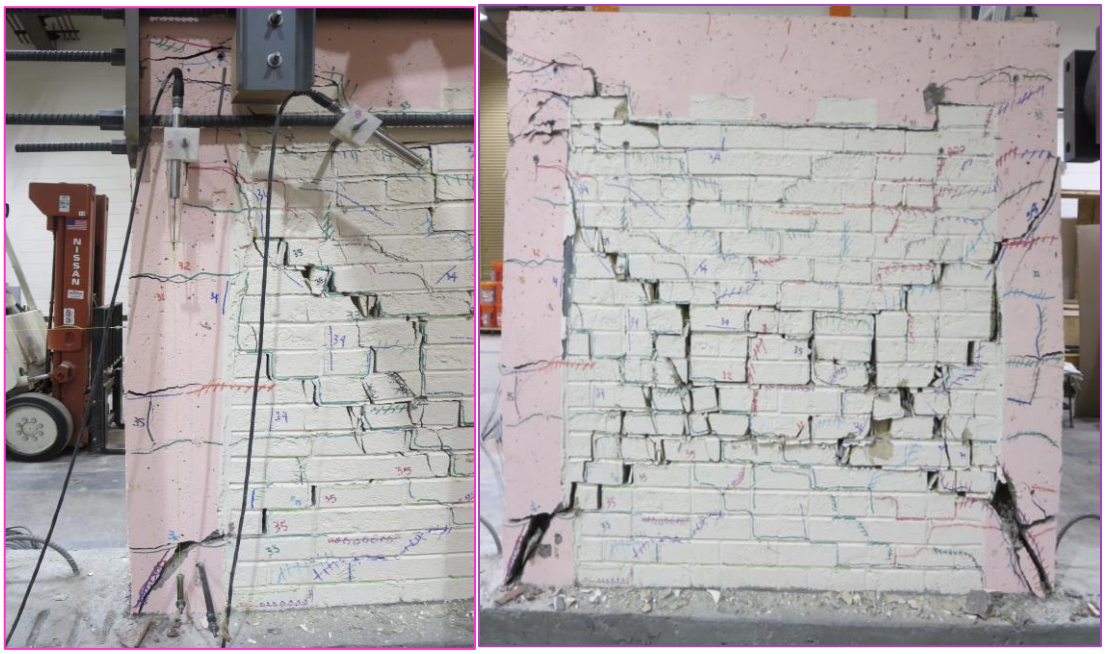

Figure 3-60. CM shear wall 2 failure mechanism

## 3.5 Chapter summary

This chapter lists out a detailed experimental test process from element testing to wall behaviors.

The results are shown in each figure and discussed throughout the section. A CM wall with a

toothed configuration moves rigidly along with the tie frame and provides greater shear strength as compared to the smooth wall with dowels. However, the strength sometimes is not the only focus for the seismic area. A CM smooth wall with dowels shows better ductility behavior, which should be considered for CM structures in seismic areas. The failure mechanism of a CM shear wall was also covered to distinguish the difference between failure in a CM shear wall and RCMI shear wall.

# Chapter 4.
# Finite Element Analysis of Confined Masonry

## 4.1 Choices of Finite Element Analysis Approach

### 4.1.1 Modeling Concepts

Masonry is an anisotropic composite material that consists of units and mortar. Accurate modeling of the masonry will require a thorough representation of nonlinear fracture mechanics as well as the properties of its constituents. In general, the modeling masonry approaches focus on 3 modeling methodologies: (1) detailed micro modeling, (2) intermediate (also known as simplified) micro modeling, and (3) macro modeling. In the micro-modeling joints, mortar layer, and units are represented separately, often mortar layer, and unit bricks are treated as continuum elements while the joints are treated as interface elements. Micro-models are well suited to understand the behavior of masonry since the Young's modulus, Poisson's ratio, and other inelastic properties of both unit and mortar are distinguished and taken into account within the model. The benefit of using such an approach is that all the different failure mechanisms can be considered and distinguished according to each material. This modeling approach treats the materials separately as illustrated in Figure 4-1, however, the approach is very intensive computationally and only suitable for small models (Lotfi and Shing, 1994).

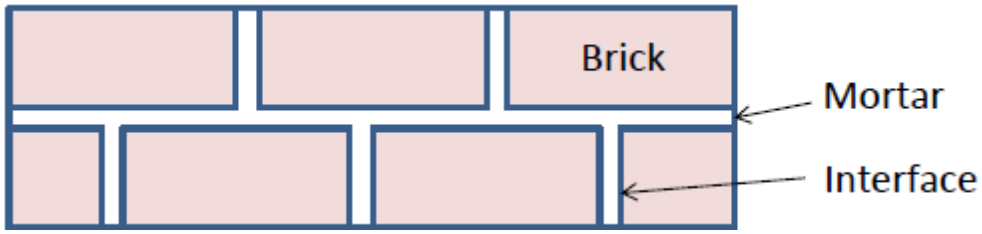


Figure 4-1. Micro model

An intermediate-simplified micro-modeling model is shown in Figure 4-2, with the units and partial size of mortar layer represented by continuum elements, and the behavior of the mortar joints and unit-mortar interface are lumped in the discontinuous elements. This approach can be compared with the discrete element method, originally proposed for use in the field of rock mechanics, where a special procedure is used for contact detection and contact force evaluation (Lotfi and Shing, 1994). In this approach, the interface elastic stiffness has to be calculated taking into account the properties of the interface at the joints as well as the mortar. Accuracy is lost since Poisson's effect of the mortar is not included.

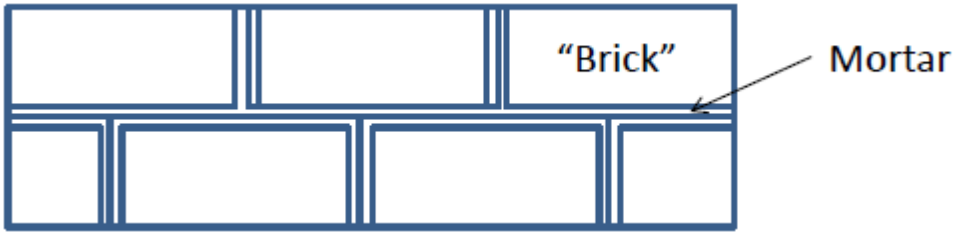


**Figure 4-2. Intermediate-simplified micro model**

The final model will be based on a macro-modeling strategy, in which the joints are smeared out in an anisotropic homogenized continuum. For some walls, when unit brick stiffness is similar to mortar stiffness, a homogenous model could be used homogeneous material law properties are applied to the composite material, and mortar joint effects are accounted for in an average sense as seen in Figure 4-3. Bricks, mortar, and the unit-mortar interface are smeared out in the continuum, and the masonry is treated as an anisotropic composite material. This methodology is relatively less time consuming than the previous ones, but still complex because of the brittle material behavior and the complexity of the "smearing" process itself. The appropriate applications of macro models are with large structures, subjected to loading and boundary conditions such that the state of stress and strain across a macro-length can be

assumed to be uniform. In this research, the macro model approach is used based on the compromise result found in the experiment for mortar, and masonry prism tests mentioned in Chapter3.

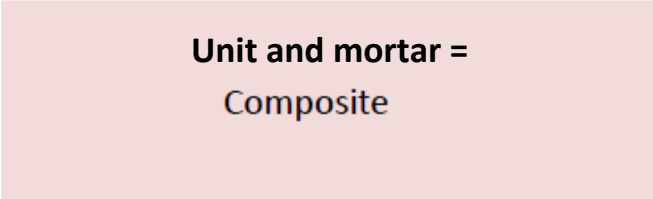


Figure 4-3. Macro model

### 4.1.2 Continuum Mechanics-Plasticity theory

In this section, a concept of plasticity in quasi brittle material is briefly discussed. The plasticity concept is not new, and for that reason, the discussion in this section serves as a transition part with some emphasis on areas that will be used in modeling masonry. Plasticity theory was originally developed to predict the behavior of metals subjected to loads exceeding their elastic limits. Basically, the theory of plasticity as it applies to a solid masonry panel is that after being subjected to a loading process, the material may sustain permanent deformation (also known as plastic deformation) when completely unloaded. This plastic deformation is then "converted" to the plastic strain, and since the deformation is permanent, the strain is irreversible. Similar models were developed later to calculate the irreversible strains in concrete, soils, and polymers. Some important phenomena properties can be identified prior to performing a plasticity model in solid material. The properties are: 1) Accept that there is an existence of an elastic domain, which is the range of stresses that is independent of plastic or permanent strain's evolution. This range has an upper limit often called "yield stress". 2) If the material is further loaded beyond the yield stress point, then the plastic yielding (also known as plastic flow which depends on the evolution of plastic strain) takes place. 3) Along with the evolution of the plastic strain, the

evolution of the yield stress itself is also observed, this phenomenon is known as hardening (Neto, Peric, & Owen, 2008). Therefore, it is customary in plasticity theory to decompose strains into elastic and plastic parts. Once the above three properties are accepted, then it is clear that a plasticity model includes (1) a yield criterion that predicts whether the material should respond elastically or plastically due to a loading increment, (2) decomposition of total strain (obviously one and two can switch places), (3) a plastic flow rule that determines the direction of the plastic strain increment caused by a stress increment in to the strain space, (4) a strain hardening or softening rule that controls the shape of the stress–strain response during plastic straining, and (5) the criterion of loading and unloading condition that defines when evolution of plastic strain and internal variables may occur (Helwany, 2007).

The outline of the topic coverage for an incremental constitutive relation for plasticity behavior in material modeling is briefly presented in equations forms as following:

1. Yield functions:

$$f(\sigma, \sigma_y) = |\sigma| - \sigma_y \qquad \text{(Equation 4.1)}$$

The meaning of the equation is straight forward: if $|\sigma| < \sigma_y$, $f < 0$ then the material is elastic. If $f = 0$, the material has yielded $|\sigma| = \sigma_y$. The absolute symbol implies that the loading could be either in compression or in tension. The function $f$ cannot be greater than 0 as the restriction of elastic domain, which means no stress level allowed above the current yield stress. Thus, this restriction leads to the limit of $f \leq 0$.

2. Kinematics decomposition of axial strain into elastic and plastic parts:

$$\varepsilon_{total} = \varepsilon^{elastic} + \varepsilon^{plastic} \qquad \text{(Equation 4.2)}$$

The kinematics of decomposition of axial strain into elastic and plastic can be visualized as in the following.

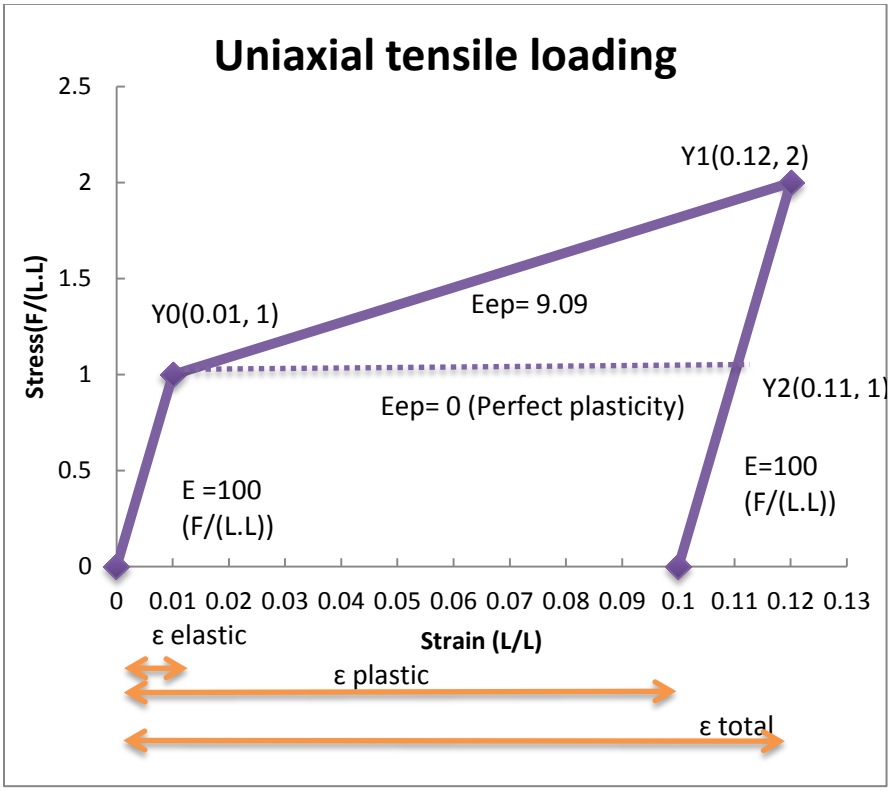


**Figure 4-4. The classical decomposition of strain into elastic and plastic parts**

Figure 4-4 shows the idealized stress–strain behavior obtained from a purely uniaxial tensile test. Plasticity commences at a uniaxial stress value Y0 of $\sigma_y$, after which the material strain hardens. It is called "hardening" because the stress is increasing relatively, also shown in from point Y0 to Y1, where the elastic-plastic slope is defined as elastoplastic modulus $E_{ep}$. If, at a strain of ε=0.12, the loading were to be reversed, the material would cease to deform plastically (at least in the absence of time-dependent effects) and would show a linearly decreasing stress with strain such that the gradient of this part of the stress–strain curve would be the Young Modulus, E. Once a stress of zero is achieved, at which the material recovers elastically amount of 0.02 in strain on a full reversal of the load, the strain remaining in the test specimen in the

plastic strain, $\varepsilon^p$. The arrow measures $\varepsilon^p$ from zero strain to indicate the deformation remains irreversibly in the material. In perfect plasticity, the elastic-plastic slope elastoplastic modulus $E_{ep}$ will be zero as shown in the dashed line. The total strain $\varepsilon_{total}$, is the sum of the two elastic strain and plastic strain: $\varepsilon^e$ and $\varepsilon^p$, respectively.

3. Plastic potential function and plastic flow rule:

The flow rule specifies the component of the plastic strain increment tensor or the direction of the plastic strain increment tensor into the strain space with respect to the increment of the stress tensor. A *plastic potential function* is often employed to describe a flow rule. A plastic potential function $g(\sigma_{ij})$ is a scalar function of stress tensor. The plastic strain increment vector corresponding to a given stress tensor $\sigma_{ij}$ is specified as a vector normal to the potential function $g(\sigma_{ij})$ at $\sigma_{ij}$.

$$d\varepsilon_{ij}^p = \mathrm{d}\lambda \frac{\mathrm{dg}}{d\sigma_{ij}} \qquad \text{(Equation 4.3)}$$

Where: $\mathrm{d}\lambda$ is a positive scalar, called plastic multiplier and has non-zero value during loading. The simplest case in selection of a plastic potential function for an elastic-perfect plastic material is to use the yield function as the potential function, i.e., $g = f$. Sometimes in literature, $\frac{\mathrm{dg}}{d\sigma_{ij}}$ is also defined as $\boldsymbol{N}$ and $\mathrm{d}\lambda$ is also defined as $\dot{\gamma}$

$$d\varepsilon_{ij}^p = \mathrm{d}\lambda \frac{\mathrm{df}}{d\sigma_{ij}} \qquad \text{(Equation 4.4)}$$

This is generally referred to as associate flow rule. Otherwise, it is referred to as non-associated flow rule. It is well-known that a non-associated formulation is required to account for pressure sensitivity of frictional material like concrete, rocks, masonry, etc. to avoid excessive plastic dilatancy (Amadei, Sture, Saeb, & Atkinson, 1989). Thus, in this study, a non-associated

formulation is used. The term $\frac{\mathrm{df}}{d\sigma_{ij}}$ is known as the gradient of the yield function with respect to the stress tensor.

4. Hardening and softening concepts:

Progression of plastic deformation alter the strain hardening parameters which include the hardening state variable(s) and its corresponding stress equivalent, and therefore modifies (sometimes even expands) the yield surface enforcing at the update value. In FEA and inelastic mechanics, the term "hardening" is understood as a numerical interpretation of a physical phenomenon. "Hardening" is due to an increase in dislocation density. Higher density of dislocations leads to greater intermingling and interlocking between particles. Once these dislocations interlock, and even if the material is unloaded, the updated value of the stress yield plus its corresponding stress equivalent is the new yield stress of the material dislocations.

The softening process could be generally understood as an opposed concept of hardening. Ortiz (1985) proposed an interesting model meant to describe general softening behavior in material. Bazant et al. summarized a simple model associated with strain softening by the mean of Rankine's plastic model. A side note to point out here is that Bazant's summary listed the concept of smear cracking and thus notation for strain included the fracturing part. The plastic Rankine model assumes total strain to be split into the elastic $\varepsilon^e$ and fracturing $e^f$ parts. Within the fracturing strain $e^f$, it is further assumed to be split into a term linear with respect to the stress and a permanent irreversible strain tensor $e^p$. Few softening rules are going to be covered here, but mostly the discussion is how to account for damage as the objectivity of the FEA. For instance, in linear degradation due to softening in tensile stress, the objectivity with respect to the finite element size is accounted for in the scaling of fracture energy $Gf$ to the average

element size (Bazant & Oh, 1983) as seen in the following Figure 4-5. In bilinear degradation, the stress-strain curve combines the elastic linear behavior and the plastic behavior of material undergone tensile stress. The last degradation due to tension stress is the exponential degradation law that is frequently used in the literature (Ozbolt & Ananiev, 2013).

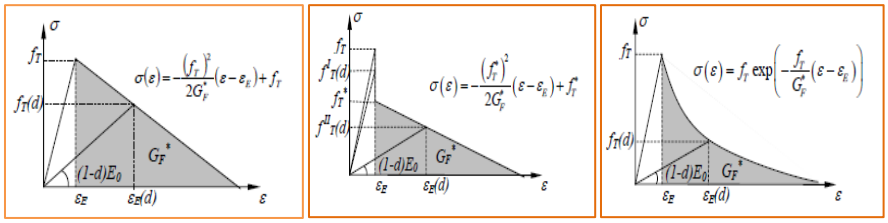


**Figure 4-5. Softening rules (Ozbolt & Ananiev, 2013)**

When the permanent deformation is the only concern (whether it is in softening or hardening), we then have a plastic deformation rate written in terms of a matrix. It is important to mention that the heart of constitutive equation for plasticity behavior in any material is a few of following phenomena in macroscopic plasticity: The nature of polycrystalline solid assumes that the solids are assumed to be isotropic and their yield criteria can be assumed to be independent of the hydrostatic pressure, and only depends on plastic slip. Additionally, there are few items to address in this macroscopic plasticity behavior: (1) plastic slip does not lead to volume change; this is so called the incompressibility condition of plasticity. (2) Plastic slip is a shearing process; hydrostatic stress, at the macro level, can often assume not to influence slip. This leads to an ideal (frictionless) fluid state of stress that measure the deviation of the state of stress from a hydrostatic stress state called the deviatoric stress tensor in plastic deformation. (3) In a polycrystalline, plastic yielding is often an isotropic process. For instance, the von Mises criterion, is which the initiation of macro scale yield is independent of hydrostatic stress. These phenomena help in explaining the concept of deriving the formulation of the yield criterion which

will only depend on the deviatoric components of stresses and furthermore, because of isotropy, the yield criterion will only depend on the magnitudes (not the directions) of the deviatoric stresses ($J$ elasto-plasticity or $J$ flow theory). This leads to the von Mises yield criterion (maximum distortion-energy criterion) where the yield criterion is given in a function of the invariants of the deviatoric stresses.

5. Loading and unloading criterion:

This step defines the sign whether or not nonlinear analysis is needed. It is stated as: if the yield function in step 1 $f \leq 0$ then loading has not yet passed the elastic domain, or else, $d\lambda \geq 0$, which means, the loading process is in the plastic space and plastic strain rate is now different than 0. The plastic strain rate is defined as the following:

$$\varepsilon^{p^{\cdot}} = d\lambda \mathrm{sign}(\sigma) \qquad \text{(Equation 4.5)}$$

$$\mathrm{sign(a)} = 1 \text{ if a} \geq 0, \text{and } \mathrm{sign(a)} = -1 \text{ if a} < 0 \qquad \text{(Equation 4.6)}$$

So the complementarity condition is satisfied as $d\lambda * \mathrm{f} = 0$.

This step ties into the loading/unloading criterion for any elastic-plastic model. That is, the constrains of: $f \leq 0, d\lambda \geq 0, \text{and } d\lambda * \mathrm{f} = 0$

The five steps listed above are the general frame work for any elastic-plastic model. The following discussion is the derivation for plastic multiplier, $d\lambda$.

Given the restriction $f \leq 0$ this implies that $\lambda = 0$ , this is known as the *consistency condition.*

### 4.1.3 Continuum Mechanics-Damage mechanics theory

As mentioned previously in 4.1.1, masonry structures can be modeled using fracture mechanics or continuum mechanic finite element approaches. In this study, CM is modeled using the second approach, the one that treats CM panel as a continuum panel. For clarification purposes,

a continuum mechanics finite element modeling approach can be done by two different methods: (1) smear cracked modeling and (2) damage plasticity modeling.

The smeared crack model approach was first introduced by Rashid in 1968; the model starts with the notion of stress and strain and permits a description in terms of stress-strain relationship. It has been stated by Rot et al. that a smeared representation is realistic considering the "band of micro–cracks" that blunt fracture in a matrix of aggregate composite such as in concrete or masonry. The idea of characterizing the softening behavior of quasi brittle material in a "smear" manner through a strain-softening constitutive relationship was then introduced by Bazant (1976) and further developed by Bazant and Cedolin (1979), and Bazant and Oh (1983). It is assumed that the micro cracks in the fracture process zone called zone $l$ are distributed over a band of width $h$, hence the name of crack band model (CBM). As the micro cracks are assumed to be smeared over the element, the whole element fractures when the uniaxial tensile strength limit, $ft$' is reached (Gambarotta & Lagomarsino, 1997). So, in a smeared crack model, material fracture energy $Gf$ is defined as the amount of energy which creates a unitary area of crack along the unit-mortar interface. Total strain now is related to the inelastic deformation and fracture energy $Gf$, and crack propagation is mainly controlled by the shape of the tensile softening diagram and fracture energy $Gf$, which is normalized by a characteristic element length $l_c$ (Bazant, Pan, & Pijaudier-Cabot, 1987).

Similar to the smeared crack model, the damage plasticity model also permits description in terms of stress-strain relationships for the continuum specimen. To expand this interpretation, it is known that material damage can be used to model specific void and crack surfaces (axial damage), specific crack and void volume (multi surface damage). The term "*material damaged*

*plasticity*" was used here to emphasize that masonry or concrete, is well-known as its low in tensile strength, and thus result in tensile cracking at very low stress as compared to compressive stress. The tensile cracking reduces the stiffness in the material structural components. Therefore, the use of continuum damage mechanics is necessary to accurately model the degradation occur within the material. Additionally, in high confining pressure, material also undergoes some irreversible deformations including plastic and damage. Because of that reason, the nonlinear behavior of the material can be captured by the mean of two distinct material mechanical processes: damage and plasticity (Neto, Peric, & Owen, 2008) (Taqieddin, 2008).

The first continuum damage mechanics model was proposed by Kachanov (1958). Without a clear physical meaning for damage, Kachanov introduced a scalar internal variable to model the creep failure of metals under uniaxial loads. A physical significance for the damage variable was given later by Rabotnov (1963) who proposed the reduction of the cross sectional area due to micro cracking as a suitable measure of the state of internal damage (Kachanov, 1986). In this context, denoting respectively by A and $A_0$ the effective loading bearing areas of the virgin and damage materials, the damage variable $D$ was introduced as:

$$D = \frac{\mathrm{A}-A_0}{\mathrm{A}} \qquad \text{(Equation 4.7)}$$

$D$ ranges from 0 to 1 corresponding to the virgin material and a total loss of load bearing capacity. In term of stress, Kachanov replaced the observed uniaxial stress σ with the *effective stress* $\sigma_{eff}$ :

$$\sigma_{eff} = \frac{\sigma}{1-\mathrm{D}} \qquad \text{(Equation 4.8)}$$

(Neto, Peric, & Owen, 2008) and (Taqieddin, 2008) provide through literature review information about the damage mechanics. Additionally, several studies have been performed

using isotropic/anisotropic continuum damage mechanics to better describe the behavior of various materials under different loading conditions (e.g., (Chow & Wang, 1988); (Simo & Ju, 1987); (Voyiadjis & Kattan, 1989). Anisotropic quantitative damage mechanics describing the number and distribution of micro cracks and their growth as well as statistical damage mechanics were also considered by many authors (e.g., (Ravindran, 2010)). Isotropic damage models (scalar based) with one or two (tension and compression) damage variables have been extensively studied by numerous authors (e.g., (Lubliner, 1990); (Lee & Fenves, 2001);. Within the theory of elasto-plasticity, Gurson (1977) proposed a model for ductile damage where the scalar damage variable if obtained from the consideration of microscopic spherical voids embedded in an elastoplastic matrix. Gurson's void growth theory has been shown to be particular suitable for the representation of the behavior of porous metals (Neto, Peric, & Owen, 2008). A scalar damage variable was also considered by Lemaitre (1983) in the definition of a purely phenomenological model for ductile isotropic damage in metals. By appealing to the hypothesis of strain equivalence, which states that "*the deformation behavior of the damaged material is represented by the constitutive laws of the virgin material with the true stress replaces by the effective stress"*, Lemaitre postulates the following elastic constitutive law for a damage material:

$$\sigma_{eff} = E_0 \varepsilon \qquad \text{(Equation 4.9)}$$

Or

$$\mathrm{E} = (1 - D) E_0 \qquad \text{(Equation 4.10)}$$

Lemaitre also found that $D$ ranges from 0.2 to 0.8 for metals. The constitutive model used in this research adopted the model found by Lemaitre's elasto plastic damage model for metals, as well as uncoupled elasticity models for concrete done by Lubliner, 1990, and Taqieddin, 2008.

For a three dimensional stress state, the above equation holds true, with the damage is the fourth order damage effect tensor. For better illustration, the tensor is shown below:

$$\begin{Bmatrix}\varepsilon_{11}\\ \varepsilon_{22}\\ \varepsilon_{12}\end{Bmatrix} = \begin{bmatrix}\frac{1}{(1-d1)E1} & \frac{-\nu 12}{E1} & 0\\ \frac{-\nu 21}{E2} & \frac{1}{(1-d2)E2} & 0\\ 0 & 0 & \frac{1}{(1-d12)2G12}\end{bmatrix}.\begin{Bmatrix}\sigma_{11}\\ \sigma_{22}\\ \sigma_{12}\end{Bmatrix} \qquad \text{(Equation 4.11)}$$

In a study for concrete modeling, (Taqieddin, 2008) derived the Helmholtz free energy as a set of state variables include: elastic strain tensor, a scalar internal variable associated with isotropic hardening and kinematic hardening. The two terms of isotropic hardening has been covered in 4.1.2 and isotropic damage and kinematic hardening will be covered latter. In a design perspective, it is reasonable to assume that damage only affects the elastic properties since local stresses are distributed to undamaged material over the effective area, and thus has a higher value as compared to the nominal stress. Simo and Ju 1987 also states: "The stress associated with a damage state under the applied strain is equivalent to the stress associated with its undamaged state under the effective strain". Hence, elastoplastic damage theory is set in a form of free energy as following:

$$\Psi^e\left(\varepsilon_{ij}^e, D\right) + \Psi^p(R, \boldsymbol{X}) \qquad \text{(Equation 4.12)}$$

Where: the two scalar damage variables for material under tension and compression are embedded in $D(\ dt, dc)$, and $(R, \boldsymbol{X})$ are the set of equivalent isotropic hardening, $R$, and $\boldsymbol{X}$ is the internal variable related to kinematic hardening, respectively.

The elastic-damage potential, also known as the elastic damage coupling is represented as the following form, according to (Neto, Peric, & Owen, 2008):

$$\bar{\rho}(\Psi^{ed}(\varepsilon^e, D) = \frac{1}{2}\varepsilon^e : (1-D)E^e : \varepsilon^e \qquad \text{(Equation 4.13)}$$

$$\sigma = \bar{\rho} d(\Psi^e)/d\varepsilon^e = (1 - D)E^e : \varepsilon^e \quad \text{(Equation 4.14)}$$

$$\sigma_{eff} = E^e : \varepsilon^e \quad \text{(Equation 4.15)}$$

$$\sigma_{eff} = \frac{1}{1-D}\sigma \quad \text{(Equation 4.16)}$$

The thermo dynamical force conjugates to the damage internal variable is given as:

$$Y = \frac{\bar{\rho} d(\Psi^e)}{dD} = \frac{-1}{2}\varepsilon^e : E^e : \varepsilon^e \quad \text{(Equation 4.17)}$$

With the inverse of the elastic stress/strain law:

$$Y = \frac{-q^2}{6G(1-D)^2} - \frac{p^2}{2K(1-D)^2} \quad \text{(Equation 4.18)}$$

The remark to make here is that plastic damaged model has been carried out on concrete by the group of researchers (Lubliner, 1990), (Oller, Oliver, Onate, & Lubliner, 1990). The model was then modified by (Lee & Fenves, 2001). These models were based on the Barcelona Model (BM) and were used successfully modeling seismic behavior of concrete dam structures. One of the most well-known examples for this numerical simulation of seismic effects on concrete dam structures is the Koyna dam, demonstrating the damage, degradation, and stability of a dam. This model then was adapted as one of the benchmark problems in the FE software ABAQUS. For clarification purposes, the BM includes two damage variables, one for tensile damage and other for compressive damage, to account for several damage states in quasi brittle material such as concrete. The uniaxial strength functions are factorized into two parts to represent the effective stress and degradation of elastic stiffness (Lee and Fenves, 1998). Two main failure mechanisms are specified in damaged plasticity modeling methods: tensile cracking and compressive crushing stress train relationships. The two failure mechanisms indicate that given a composite material specimen, FEA can effectively capture the failures of that specimen under certain loading

conditions using its uniaxial tension and uniaxial compression behaviors. A model assumes that the uniaxial tensile and compressive response of a quasi-brittle material is characterized by the damage plasticity concept, as shown below:

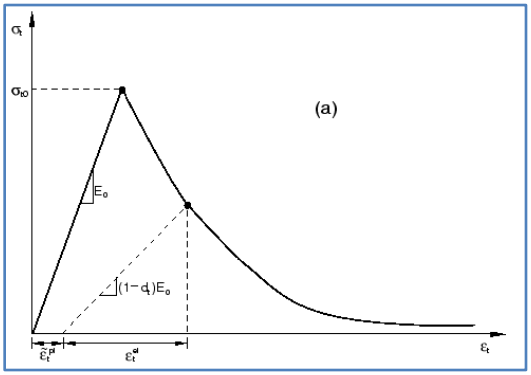


**Figure 4-6. Uniaxial tension (Abaqus, 2009)**

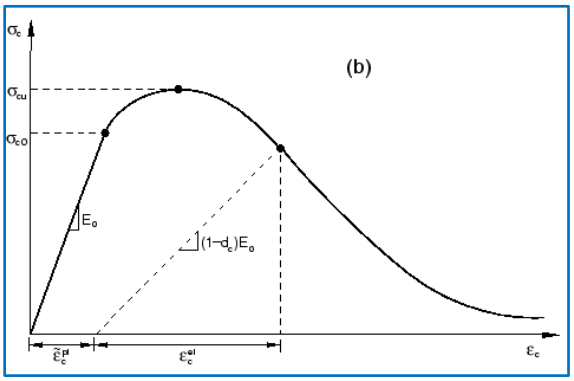


**Figure 4-7. Uniaxial compression (Abaqus, 2009)**

Where: $E_0$: Elastic modulus of material.

$\varepsilon_t^{pl}$ and $\varepsilon_c^{pl:}$ are hardening variables with respect to tension and compression loading, respectively.

$dt$ and $dc$ are the two scalar damage variables written within the form of $D$ with respect to tensile cracking and compression crushing, respectively.

As seen in Figure 4-6 and Figure 4-7 when concrete or other quasi brittle material is unloaded from any point in the strain softening branch of the stress-strain curves, the unloading

response is observed to be weakened: the elastic stiffness of the material appears to be damaged or degraded. The degradation of the elastic stiffness is significantly different between tension and compression tests. For concrete and masonry, the damage is experienced quickly after the yielding point in tensile loading, while in compression loading, the materials experienced a significant amount of plastic strain and hardening stress before the damage and degradation takes place. In other words, at the moment damage takes place during tensile loading, the tensile plastic strain is not the same magnitude as of the tensile compression plastic strain. In either case, the effect is more pronounced as the plastic strain increases. The degraded responses of concrete in particular and of quasi brittle material in general are characterized by two independent uniaxial damage variables: $d_t$ and $d_c$, which are functions of the plastic strain, temperature, and internal state variables as mentioned previously in Section 4.1.2

The plastic–damage model assumes that the elastic stiffness degradation is isotropic and characterized by a single scalar variable, $D$. The definition of the scalar degradation variable $D$ must be consistent with the uniaxial monotonic response, (i.e. whether the loading is in compression or in tension, thus the variables are defined as $dt$ or $dc$, respectively), and it should also capture the effect associated with the degradation mechanism in cyclic loading as well. In both scenarios, the contribution of the damage variable to the elastic modulus $E_0^{el}$ is as follows:

$$E^{el} = (1 - D)E_0^{el} \quad with \ 0 < D < 1 \qquad \text{(Equation 4.19)}$$

where $E^{el}$ is the damaged elastic molulus, the linear slope of the stress-strain curve at any point of unloading once the damage takes place in the material panel.

As a conclusion for the elastoplasticity with damage couple modeling process, it is then reasonable to draw out the procedure as follows:

1. Decomposition of strain tensor, notice that this is similar to step 2 in Section 4.1.2

2. Define free energy function, in this study it is set as:

$$\Psi^e\left(\varepsilon_{ij}^e, D\right) + \Psi^p(R, \boldsymbol{X}) \qquad \text{(Equation 4.20)}$$

In general, (D, R,X) is an α set of state internal variables

3. Compute stress and set the equation for thermodynamic force A

$$\sigma = \bar{\rho} d(\Psi^e)/d\varepsilon^e \qquad \text{(Equation 4.21)}$$

$$A = \bar{\rho} d(\Psi)/d\alpha \qquad \text{(Equation 4.22)}$$

4. Yield function

$$\Phi = \Phi(\sigma, A) \qquad \text{(Equation 4.23)}$$

5. Plastic flow rule and hardening rule:

$$\dot{\varepsilon_p} = \dot{\gamma}\mathrm{N}(\sigma, A) \qquad \text{(Equation 4.24)}$$

$$\dot{\alpha} = \dot{\gamma} H(\sigma, A) \qquad \text{(Equation 4.25)}$$

$$\mathrm{N} = \frac{d\Psi}{d\sigma} \qquad \text{(Equation 4.26)}$$

$$\mathrm{H} = -\frac{d\Psi}{dA} \qquad \text{(Equation 4.27)}$$

6. Loading and unloading criterion

$$\Phi \leq 0,\ \dot{\gamma} \geq 0,\ \dot{\gamma}\Phi = 0 \qquad \text{(Equation 4.28)}$$

The elastoplasticity with damage couple modeling process is not new. The theory and the steps were used by many studies referenced in Section 3.13 including in some commercial FE software. For example, ABAQUS has a built in damage plasticity model for concrete, called: concrete damage plasticity. The built in model was used at the starting point of the study and has validated the software's robustness of the built-in element in number of the CM shear wall examples. However, to be able to use the built in mode in ABAQUS, constitutive stress-strain for

the wall panel has to be pre-calculated and fed to the software such that the software has the path to "drive" the material behavior. For instance, an exponential relationship of stress and crack displacement is plotted below for the tensile behavior, where crack displacement is calculated as plastic strain multiplied by characteristic element length. Recall that the damaged plasticity modeling is a "smear" process where mesh size chosen in analysis is critical and this still holds true for the built-in model in the case here where a user-written computational code will be used instead of the algorithm contained in ABAQUS. In FE modeling, characteristic element length is measured relatively by the chosen mesh size. So, if cracks were assumed to happen within an element, and the element chosen is a quadratic element type, then the characteristic length, $lc$ is the square root of the summation from vertical and axial sizes of the element. If the crack displacement is assumed to be in more than one element then characteristic length is rounded up to the square root of the summation from the vertical and axial size of the summation of elements. Figure 4-8 plots the exponential behavior of uniaxial stresses versus the crack displacement. The blue curve shows $h$ is determined as a damage region, and $lc$ is an element characteristic length. As the plastic strain increases, the curve gets flatter when the damaged region is assumed to happen in more than one element and vice versa.

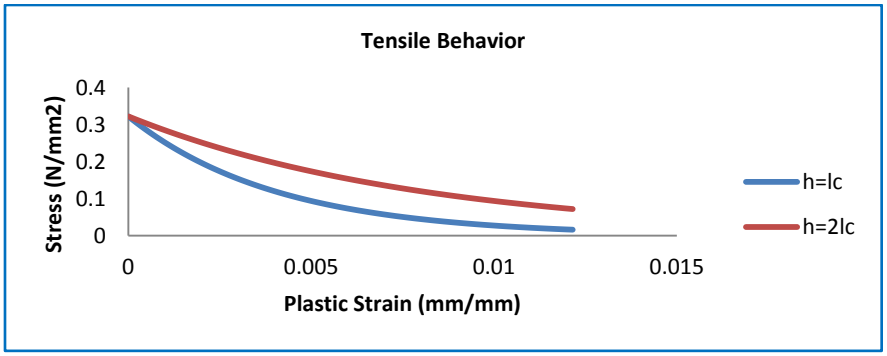


**Figure 4-8. Uniaxial tensile behavior of masonry.**

When a masonry assembly prism is under compression, past the yielding load, lateral expansion of the mortar introduces a lateral tensile stress on the brick, which in turn provides confining stress on the mortar (Hilsdorf, 1969). As compression load increases, it often leads to tensile splitting of the brick in a plane perpendicular to the bed joints. This tensile splitting behavior of a brick unit could be understood using Figure 4-9 below, showing the deformation of a specimen undergoing vertical load. The confinement direction and the expansion direction are illustrated in the segment perpendicular to the direction of applied load. Figure 4-9 shows a failure captured in the prism compression test, which captures the tensile splitting of the brick as well. The line drawn on the figure shows the crack pattern experienced at failure.

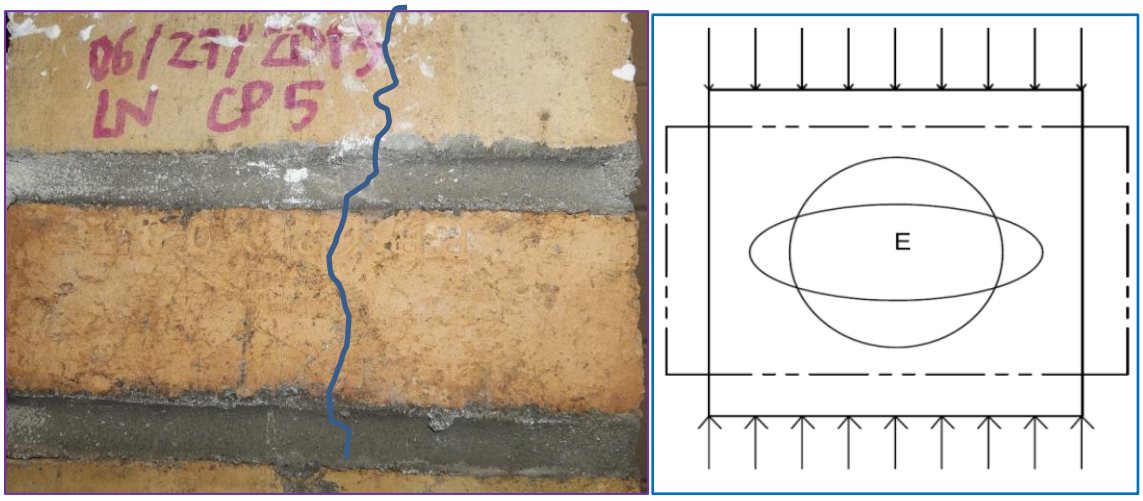


**Figure 4-9. Uniaxial compression behavior in quasi brittle material (Left photo: Nguyen, 2013)-(Right sketch: (Ozbolt, Li, & Kozar, 2001)**

A uniaxial compression stress-strain constitutive relationship is plotted adopting the constitutive relationship studied by (Lourenco, 1998) is shown in Figure 4-10. An interesting observation when the assumed length of damaged elements varies, the behavior of the stress-strain curve over the softening region shifts to the right of the chart, allows plastic strains to be greater than the one with crack displacement assumed to be within the element.

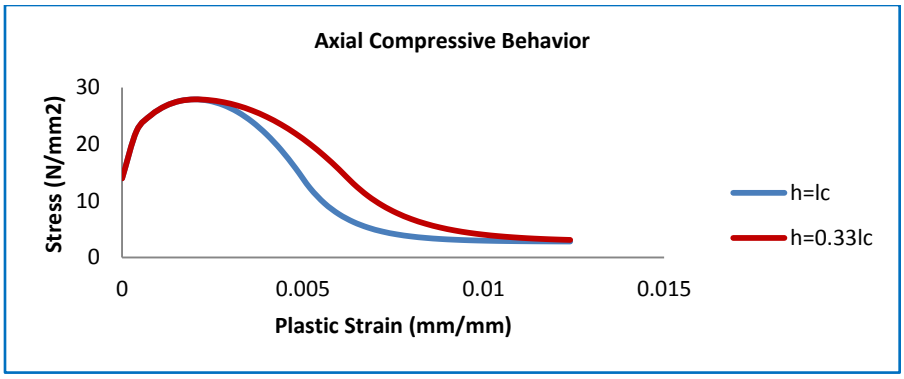


Figure 4-10. Compressive stress-strain behavior.

Having a built in model in ABAQUS is an advantage to cross check the analytical solution, as well as for providing good illustration (i.e. stress contour after deformation) in any FE modeling. Unfortunately, sometimes is also a limitation when using a commercial program, is that calibration strictly depends on the "choice" of a "complete" stress-strain constitutive path point to point. This difficulty is even greater for modeling nonlinear behavior in solid material since the material's stress-strain constitute path is not well defined. In addition, it is advantageous to be able to control the algorithm of the model in the process of finding the complicated behavior. In this study, a FE algorithm using elastoplasticity with damage couple modeling written based on finite strain theory is used. The algorithm is then implemented to a user subroutine defined as UMAT option ABAQUS.

### 4.1.4 Finite strain elastoplasticity

Section 4.1.2 and Section 4.1.3 have covered the background for plasticity and damage mechanics in continuum elements. Those sections are based on small-strain theory, which could capture inelastic behavior in solids as long as the strains and rotations remain sufficiently small. In many applications exhibiting plasticity, however, the infinitesimal deformation hypothesis cannot be introduced without significant loss of accuracy (Neto, Peric, & Owen, 2008). Using the

damage theories covered previously in Section 4.1.3 and the finite strain elastoplasticity that will be covered in this section, damage will be shown within the masonry panel continuum media.

Assume that the "movement" of a continuum solid element within a CM shear wall undergoing in-plane loading can be captured in multiple time stages. In the travel process from one stage of loading to the next, there are deformations that could reflect a developing mortar crack pattern, rigid deformation experienced by the white continuum unit brick and its surrounding mortar layers, and deformation internal to the brick, which is assumed not to be undergoing damage within its volume.

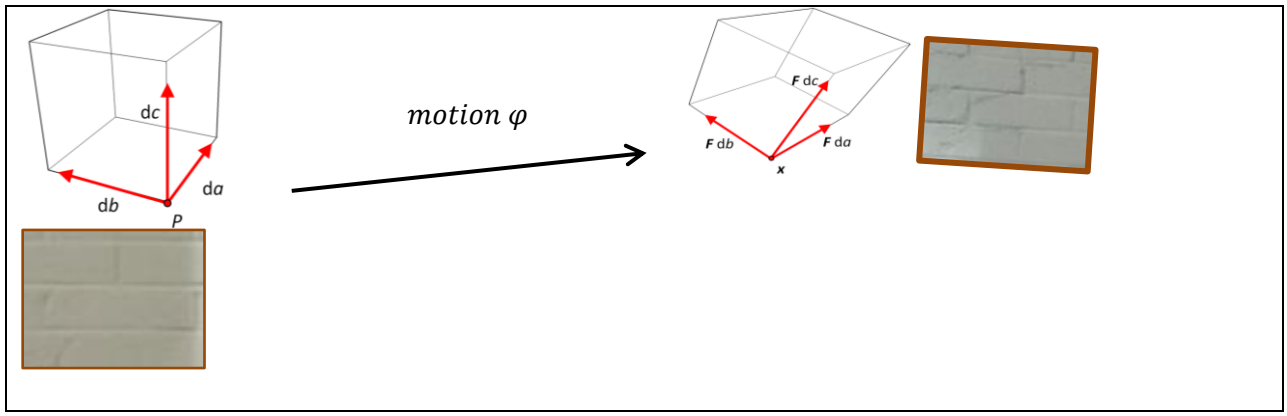


**Figure 4-11. Deformation of mortar and continuum unit brick in multi time stages**

The travel process is called *motion* $\varphi$ in finite strain theory. The deformation within the continuum material is described by a second order tensor $F$, referred to as the deformation gradient tensor. Under any deformation possibly occurring during the "*motion* $\varphi$", F maps the change of $x$ with respect to the change of the original position of particle $p$. So, x is the position of material particle $p$ at time $t$.

$$F(x,p) = \frac{\partial x_t}{\partial p} \qquad \text{(Equation 4.29)}$$

The deformed infinitesimal volume is given by:

$$dv = (F\ da\ \times F\ db).F\ dc \qquad \text{(Equation 4.30)}$$

The volume after deformation per unit reference volume is defined as:

$$\det F = \frac{dv}{dv_0} \qquad \text{(Equation 4.31)}$$

We adopt the notation as used in literature by setting the determinant of the deformation gradient to $J$:

$$\det F = \frac{dv}{dv_0} \equiv J \qquad \text{(Equation 4.32)}$$

Physically speaking, the volume of solid is not allowed to penetrate itself, so if there is no deformation in the *motion* $\varphi$, then $F = I$, which means $J = 1$, and in any deformed configuration of a body, $J$ satisfies the fact that $J > 0$. Within the *motion* $\varphi$*, isochoric deformations* are deformations that produce no changes in volume. A locally isochoric deformation is characterized as $J = 1$. In addition, volumetric deformation are deformations consisting of purely uniform contraction/dilation in all directions, $F = \alpha I$ , where $\alpha$ is the corresponding contraction/dilation ratio in all directions within the body.

The outline of the topic coverage for an incremental constitutive relation for plasticity behavior in material modeling under finite strain theory is presented in steps as following:

1. Isochoric and volumetric split of deformation gradient.

$$F = F_{iso}F_v \qquad \text{(Equation 4.33)}$$

$$F_v = (\det F)^{1/3} I \qquad \text{(Equation 4.34)}$$

$$F_{iso} = (\det F)^{-1/3} F \qquad \text{(Equation 4.35)}$$

$F_v$ represents deformation gradient for volumetric deformation, pure contraction or dilation in all directions

$F_{iso}$ represents the deformation gradient for volumetric preservation which are deformations that do not produce the change in volume.

For our study, we applied the multiplication decomposition for the deformation gradient, it is written as:

$$F = F_e F_p F_d \qquad \text{(Equation 4.37)}$$

With $e,\ d,\ p$,standing for elastic, damage, and plastic, respectively.

The Jacobian tensor, which also described as the determinant of the deformation gradient matrix $F,\ J$ corresponding to this multiplication is thus broken down to elastic, damage, and plastic parts:

$$\det F_e \equiv J_e \qquad \text{(Equation 4.38)}$$

$$\det F_d = \frac{dv}{dv_d} \overset{\text{def}}{=} \frac{1}{1-\emptyset} \equiv J_d \qquad \text{(Equation 4.39)}$$

Solving backward from this definition, we have:

$$F_d = \frac{1}{(1-\emptyset)^{1/3}} \qquad \text{(Equation 4.40)}$$

The derivation for $F_p$ involves the time derivative for both spinning and stretching motion in a body. In the final form,

$$F_p = F^{iso}{}_e L^p F^{iso\,(-1)}{}_e \qquad \text{(Equation 4.41)}$$

$$L^p = \dot{F}_p {F_p}^{-1} \qquad \text{(Equation 4.42)}$$

2. Polar decomposition. Stretch and rotation

   The movement of the body essentially is broken down to a process that includes: deformation, rigid translation, and rigid rotation. In which,

$$F = RU = VR \qquad \text{(Equation 4.43)}$$

$$U = \sqrt{C} \qquad \text{(Equation 4.44)}$$

$$V = \sqrt{B} \qquad \text{(Equation 4.45)}$$

$$C = F^T F \qquad \text{(Equation 4.46)}$$

$$B = F F^T \qquad \text{(Equation 4.47)}$$

   $R$ is a rotation tensor:

$$R = \begin{bmatrix} \cos\alpha & -\sin\alpha \\ \sin\alpha & \cos\alpha \end{bmatrix} \qquad \text{Equation 4.48)}$$

3. The strain measures:

With the similar concept of strain decomposition for covered in Section 4.1.2, the infinitesimal isochoric and volumetric split of the strain tensor is given by:

$$\varepsilon_{total} = \varepsilon^d + \varepsilon^v \qquad \text{(Equation 4.49)}$$

   $\varepsilon^d$is the isochoric component, known as the strain deviator or deviatoric strain, which measures the pure infinitesimal distortion.

   $\varepsilon^v$ is the infinitestimal volumetric strain tensor. An infinitesimal strain $\varepsilon^v$= 0 if the volume is preserving during the “motion”

4. Deviatoric and hydrostatic stresses:

Section 4.1.2, step 5 discussed the split of the stress tensor into hydrostatic and deviatoric stresses. The finite strain theory treats this split identically. The stress tensor is split into the sum of the spherical and traceless components:

$$\bar{\sigma} = \bar{s} + \bar{p}\boldsymbol{I} \qquad \text{(Equation 4.50)}$$

$$\bar{p} = \frac{1}{3}\mathrm{tr}(\bar{\sigma}) \qquad \text{(Equation 4.51)}$$

$$\bar{S} = \bar{\sigma} - \bar{p}\boldsymbol{I} \qquad \text{(Equation 4.52)}$$

The connection from the Cauchy stress tensor $\bar{\sigma}$ listed above to the deformation gradient $F$ can be understood by the first Piola Kirchhoff stress. By definition, at the point of interest, the first Piola Kirchhoff stress measures the force that acts across any surface in the deformed configuration per unit reference area. Consider a surface $da$, corresponding to the deformed area element that has $n$ as a normal vector. Under deformation, the tangent vector $dp1$ and $dp2$ are mapped, into $F\ dp1$, and $F\ dp2$. So, the changed $da$ with respect to the reference surface area $da_0$ that has a unit vector $m$ is equivalent to:

$$\frac{da}{da_0}n = JF^{-T}m \qquad \text{(Equation 4.53)}$$

The Piola transformation, stress mapping is

$$\sigma = \frac{FSF^T}{J} \qquad \text{(Equation 4.54)}$$

For the elastic deformation gradient, the stress mapping is as following:

$$\sigma = \frac{F_eSF^T{}_e}{J^e} \qquad \text{(Equation 4.55)}$$

And by definition of effective undamaged stress state, we have:

$$\sigma_{eff} = \frac{F_d \sigma_{eff} {F_d}^T}{J^d} \qquad \text{(Equation 4.56)}$$

$$\sigma_p = \frac{F_p \hat{S} {F^T}_p}{J^p} \qquad \text{(Equation 4.57)}$$

A more in depth mechanics theory for finite strain can be found in (Neto, Peric, & Owen, 2008). In brief, a set of mechanical constitutive equations for nonlinear continuum solid modeling based on finite strain theory is then summarized down to the following:

$$\left\{ \begin{array}{c} \Psi = \Psi(F, \alpha) \\ P = \bar{\rho} \frac{\partial \Psi}{\partial F} = J \overline{\sigma F^{-T}} \\ \dot{\alpha} = f(F, \alpha) \end{array} \right\} \qquad \text{(Equation 4.58)}$$

The numerical algorithm work in this section is developed based on the framework of finite strain deformation theory. The plastic deformations are computed in the effective stress space, which is independent for the damage. For clarification purpose, reader is referred to Section 4.1.3, where we assumed that the damage is only effect of the elastic deformation. The model comprises Ducker-Prager type yielding surfaces for loading adopted from the work originally done by (Regueiro, 2014). Building upon the formulation, the plastic modeling is done for the compression loading in this study to account for the hardening in the masonry panel. The theory of modeling formulation in compression loading is based on the study done by (Taqieddin, 2008) for modeling concrete behavior. Combined the two background findings from the two references above, an algorithm is made with coupling tensile and compression behavior for modeling CM masonry wall. One of the new steps in this formulation is providing the damage evolution in accordance with the relationship of degradation cohesion and plastic strain. As mentioned previously in Section 4.1.3, during tensile loading, the strength of material reduces

exponentially with respect to plastic strain (See also in Figure 4-8). On the other hand, we also discussed that damage increases as plastic strain increases, and the damage variable is from 0 to 0.8 (for illustration purpose, we plot damage variable from 0 to 1 in this plot). The damage evolution and plastic strain relationship is plot shown in Figure 4-12.

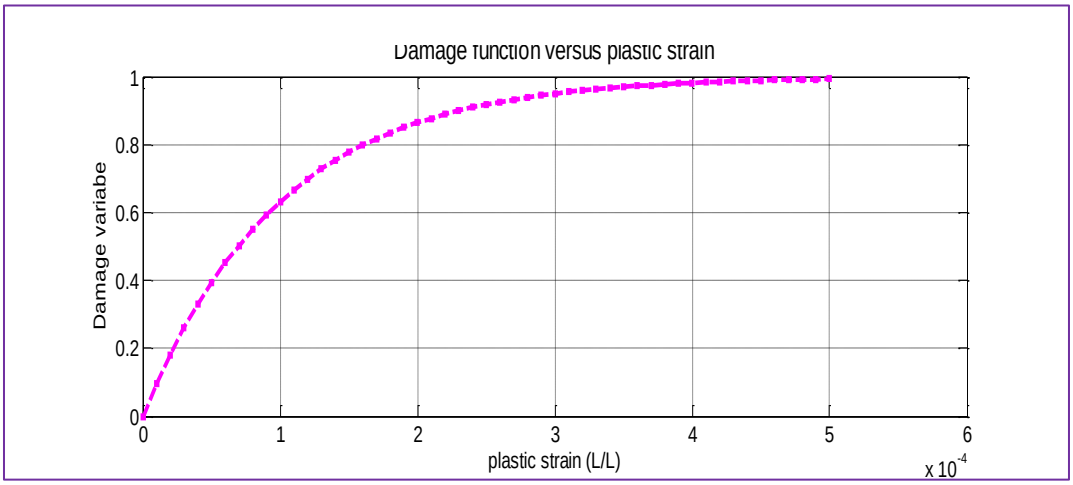


**Figure 4-12. Damage variable versus plastic strain**

The procedure for an incremental constitutive relation for plasticity behavior in material modeling is presented in equation form as the following:

1. The general Drucker-Prager yielding surface is as follows:

$$F(\bar{\sigma}, \bar{\varepsilon}^{pl}) = \sqrt{J_2(\bar{S}(\bar{\sigma}))} + \eta\bar{p} - c(\bar{\varepsilon}^{pl}{}_c) \leq 0 \qquad \text{(Equation 4.59)}$$

Where:

$$\bar{p} = \frac{1}{3}\bar{\sigma}: I \qquad \text{(Equation 4.60)}$$

$\bar{p}$ is the effective hydrostatic pressure.

$J_2$ is the Von Mises equivalent stress: $J_2 = \frac{1}{2}\bar{S}: \bar{S}$ (Equation 4.61)

$\bar{S}$ is the effective deviatoric stress, the deviatoric part of the Cauchy stress $\bar{\sigma}$ tensor

$$\bar{S} = \bar{\sigma} - \bar{p} \qquad \text{(Equation 4.62)}$$

The $\eta$ parameter is a dimensionless constant given by Lubliner et. al. [1989], and in tension is defined as:

$$\eta = \frac{f_c - f_t}{\sqrt{3}(f_c + f_t)} \qquad \text{(Equation 4.62)}$$

$c(\tilde{\varepsilon}^{pl})$ is a cohesion function with respect to plastic strain. The expression for cohesion with respect to plastic strain rate due to compression was used by (Taqieddin, 2008) in concrete modeling. Since concrete and masonry behavior in compression is more ductile as compared to tension (Taqieddin, 2008), the expression is adopted in this study. The compressive cohesion hardening function $c^-$ is defined by the following exponential law:

$$c^- = f_0^c + Q(1 - \exp(-\omega \varepsilon_c^{pl})) \qquad \text{(Equation 4.63)}$$

Where: $Q$ and $\omega$ are the two material constants related to the function hardening of the material.

For tension loading, the expression for cohesion with respect to tensile loading plastic strain rate is as follows (as used in (Neto, Peric, & Owen, 2008):

$$c^+ = f_0^t + h(\varepsilon_{ct}^{pl}) \qquad \text{(Equation 4.64)}$$

Where: $h$ is the hardening modulus.

2. The flow potential equation is of the following form:

$$g = \frac{\bar{S}}{2\sqrt{J_2(\bar{S}(\bar{\sigma}))}} + \frac{\eta}{3}\boldsymbol{I} \qquad \text{(Equation 4.65)}$$

$f_0^t$ is the uniaxial tensile stress at failure; in this study, the value is the flexural stress taken from the bond wrench test result.

$f_0^c$ is the uniaxial compression stress at failure; in this study, the value is the compression stress taken from the compression prism test result.

The plastic strain rate is defined as:

$$\dot{\varepsilon_p} = \dot{\gamma}\mathrm{g} \qquad \text{(Equation 4.66)}$$

3. The evolution equations involved for updating damage according to (Neto, Peric, & Owen, 2008) is defined as

$$\dot{D} = \dot{\gamma}\frac{1}{1-D}\left(\frac{-Y}{r}\right)^{s} \qquad \text{(Equation 4.67)}$$

With Y defined previously in Section 3.1.3. Parameter s and r are the two material constants

Seen in equation 4.67, the damage evolution is a function of plastic strain rate $\dot{\gamma}$, damage variable D, and material constant. A study done by (Regueiro, 2014) introduced a damage evolution that is a function of effective stress and the rate of the effective stress with respect to time:

$$\dot{D} = D_{max}\left(-epx\left(\frac{-\langle\bar{p}\rangle}{P_{sat}}\right)\left(\frac{1}{P_{sat}}\right)\frac{1}{2}(sign(\bar{p})+1)\frac{d\langle\bar{p}\rangle}{dt}\right) \qquad \text{(Equation 4.68)}$$

The damage evolution used in our study is based on (Regueiro, 2014), but instead of having a damage evolution changes with respect to the stress rate, it is an evolution changes with respect to plastic strain rate as plotted in Figure 4-12. For instance, (Taqieddin, 2008) and (Lourenco, 1998) have shown the maximum plastic strain rate at lowest tensile loading is 0.0005 in/in. We consider the maximum plastic strain rate $k_{max}$due to tensile loading is at 0.0005in/in. If the maximum damage is 1, the plastic strain rate is 0 at maximum tensile load, and lowest tensile loading is $k_{max}$. Then, equation 4.68 in terms of damage function becomes:

$$D = D_{max}\left(1-\frac{\dot{\gamma}}{k_{max}}\right) \qquad \text{(Equation 4.69)}$$

Recall that the back stress updating step is to return to the yield surface as a requirement of the restriction mentioned in outline number 1 in Section 4.1.2. It is defined as:

$$\boldsymbol{\alpha} = \dot{\gamma}\frac{\bar{S}}{\|\bar{S}\|}h^{\alpha} \qquad \text{(Equation 4.70)}$$

With $h^{\alpha}$ can be understood as the parameter accounts for the kinematic hardening.

4. Loading and unloading criterion: $F \leq 0;\ \dot{\gamma} \geq 0;\ F\dot{\gamma} = 0$

### 4.1.5 FE implementation algorithm used in this study

The FE implementation algorithm developed in this section beside the studying purpose, it is also to accomplish three objectives. They are:

1. To have fully control of the material behavior following plasticity rules mentioned in Section 4.1.2 and damage rules mentioned in Section 4.1.3.
2. To capture any damage in the deformation within one element by the use of finite strain.
3. To serve as a validation method for the experimental test reported previously in Chapter 3.

The user subroutine implemented into ABAQUS for this study consists of the implicit method and a set of internal state variables. For clarification purpose, an implicit method that can be described as finding a solution from current time step to the $(n+1)^{\text{th}}$ time step using information from that $(n+1)^{\text{th}}$ step. Using an implicit method, one has to solve a nonlinear equation for $x(t+\Delta t)$. The main disadvantage of using implicit methods is the formation of the stiffness matrix with return mapping algorithm. In the other words, when choosing the implicit method, the time cost in any finite element analysis is a disadvantage (it takes longer to process) because in each step of solving a nonlinear equation, the algorithm needs to map back to the current time step solution. A fundamental decision that needs to be made in the numerical

analysis is whether to utilize an implicit or explicit integration scheme (ABAQUS, 2009). The former has several advantages, a primary one of which is that convergence to accurate results is generally assured. The method, however, may be numerically expensive due to the requirement of solving nonlinear equations at each step, which necessitates the reformulation of the stiffness matrix. In addition, the implicit method may not always converge in the case of nonlinear brittle materials. The Explicit method has the disadvantage of requiring very small increment steps and that may lead to incorrect results, and also the results can be difficult to interpret. The decision was made to use the implicit approach in this study, but a concern was that with highly nonlinear or brittle material, the implicit method may fail to converge. Implicit methods generally use the Newton-Raphson scheme or a modified Newton algorithm. Due to the brittle material used for this study, the stiffness matrix may not be well-conditioned, and to prevent divergence a line search algorithm and arc-length method (also known as the Riks method) was used.

It is important to note that ABAQUS has the deformation gradient $F$ tensor embedded in the user subroutine with the use of implicit method called UMAT. The deformation gradient $F$ tensor at the initial time step and the trial deformation gradient $F$ tensor at the next time step thus are given. The algebraic steps involve in the numerical implementation for plane stress elements are as listed below:

Step 1. Call out deformation gradient F tensor in UMAT

Step 2. Calculate the Jacobian determinant with respect to initial time step and the next time step.

$$J_n = \det[\mathrm{F}_0]$$

With $[\mathrm{F}_0]$ and its tensor provided by ABAQUS

$$J_{n+1} = \det[\mathrm{F}_1]$$

With $[\mathrm{F}_1]$ and its tensor provided by ABAQUS

Step 3. Create a place holder for the internal state variables, including the change of the Jacobian tensor. These place holders will be updated after every time step. For instance, cohesion is a function of plastic strain rate. In terms of increment step, call the cohesion rate with respect to plastic strain rate, $dc = f(d\varepsilon^{pl})$

Step 4. Introduce all the elastic parameters. For instance, in the FE model, define Young's modulus, E, Poisson ratio, etc.

Step 5. Define all constants involved in the calculation.

Step 6. Calculate mean stress and deviatoric stress at the initial time step ($t_n$)

With $[\bar{\sigma}_0]$ and its tensor place holder provided by ABAQUS

$$\bar{p} = \frac{1}{3}\bar{\sigma}$$

$$\bar{S} = \bar{\sigma} - \bar{p}$$

Step 7. Designate the place holder for elastic tangent modulus in the matrix form.

Step 8. Assign elastic value to elastic tangent modulus matrix.

Step 9. Calculate the trial effective deviatoric stress using strain increment

With $[\varepsilon_0]$ and its tensor place holder is provided by ABAQUS

$$\overline{\bar{\sigma}} = \bar{\sigma}_n + E\Delta\varepsilon$$

Step 10. First check: $F\left(\overline{\bar{\sigma}}\right) < 0$

Step 11. If $F\left(\overline{\bar{\sigma}}\right) < 0, \bar{\sigma}_{n+1}$=$\overline{\bar{\sigma}}$ and $\varepsilon_{n+1}$=$\varepsilon_{n,}$ go to Step 16

Step 12. If $F(\bar{\bar{\sigma}}) \geq 0$, calculate plastic multiplier $\dot{\gamma}$, $\dot{\varepsilon}_p$, calculate trial effective stress using plastic strain rate $\dot{\varepsilon}_p$,since the yield function involves cohesion, update cohesion.

Step 13. Update trial mean effective stress

Step 14. Update damage

Step 15. Check consistency condition, if all is correct, update damage, and calculate undamaged stress.

Step 16. Update the Jacobian tensor

Step 17. Update the Elasto-plastic tangent with the new stress

Step 18. Store internal state variables in the place holder

Step 19. Proceed to the next time step, by returning to step 1.

## 4.2 Plasticity Concepts in Reinforcement Bars

Typical stress-strain curves for reinforcing steel bars used in concrete and masonry construction are obtained from experiments which load bars monotonically in tension. For all practical purposes, steel exhibits the same stress-strain curve in compression as in tension. The steel stress-strain relation exhibits an initial linear elastic portion, a yield plateau, a strain hardening range in which stress again increases with strain and, finally, a range in which the stress drops off until fracture occurs. The extent of the yield plateau is a function of the tensile strength of steel. High-strength, high-carbon steels, generally, has a much shorter yield plateau than relatively low-strength, low-carbon steels. For FE modeling, isotropic hardening Von Mises is ideally for perfect plastic behavior of the reinforcement steel. In this modeling analysis, the bond between surrounding material and the steel rebar is assumed to be perfect, thus damage around the

surface area of the interface between reinforcement steel bar and the material environment is neglected.

## 4.3 Finite Element Models

Before applying the user subroutine developed in section 4.1.5, it is essential to understand all the modelling stages involved in ABAQUS. Numerical issues could either caused from developing mesh size, or convergence issue, etc. The following three models are served as the introduction in modeling using ABAQUS software built in damage plasticity model. At each modeling stage, the observation will be reported and use to further assist the last two models which will be discussed in Section 4.3.4 and Section 4.3.5.

### 4.3.1 Model 1: CM shear wall

Three full-scale one story CM house models were built and tested on the shaking table at the Laboratory of Structures at the Pontifical Catholic University of Peru in 2008 led by Quiun. House models consisted of four walls with one confining tie-column at each of the four corners and a top confining tie-beam on top of each wall. For simplicity, this chapter models solely the in-plane loading behavior of one shear wall without openings and one with an opening from the aforementioned experiment in lieu of the whole house model. Both analyses were done by using the built in damage plasticity model in the FEA software ABAQUS. Model features included 1440 shell elements for both the concrete tie element frame and the masonry panel. Plasticity behavior in the wall was represented by the use of plasticity model and finite strain modeling was used for large deformation in mortar behavior as discussed in Section 4.1. The FE model used parameters similar to those described in Quiun's test in 2011, and was solely to capture the crack behavior under shear loading conditions, and to emphasize the effectiveness of modeling

between Implicit and Explicit methods. Adjustment was made to the concrete compressive strength in the model due to the limited range of provided fracture energy in the ABAQUS material library. For clarification, ABAQUS material library gives a range of available materials with corresponding to the range of fracture energies. Prior to modeling, the adjustment according to the material properties has to be done to ensure the model parameter is within the range of given values. This adjustment benefits the convergence in numerical analysis using ABAQUS, but seems less intuitive for the engineer to visualize the effect of the analysis upon using different material properties in general. For instance, steel used in Quiun's test had yield strength of 535 MPa (78ksi) while the concrete and masonry used were considerably weaker. The adjusted steel's strength in this model used yield strength of 400 MPa (58 ksi) for compatibility purposes. This adjustment, again, is to get convergence as part of the requirement of the commercial software. Parameters can be seen in the following Table 4-1 and Table 4-2:

| Wall Properties | cm | in |
|---|---|---|
| Tie column to ties column | 300 | 118 |
| Wall thickness | 15 | 6 |
| Ties beam to tie beam | 300 | 118 |
| Wall area | 90 (x cm) | 35 |
| Column width | 15 | 6 |
| Column thickness | 15 | 6 |
| Column height | 300 | 118 |
| Longitudinal bar diameter | 0.8 | 0 |
| Quantity | 4 (bars) | |
| Tie spacing | 25 | 10 |
| Beam width | 15 | 6 |
| Beam thickness | 15 | 6 |
| Beam depth | 20 | 8 |
| Brick unit length | 21 | 8 |
| Brick unit width | 10.5 | 4 |
| Brick unit height | 6.5 | 3 |

**Table 4-1. Material parameters used in ABAQUS model**

| Material Properties | $N/mm^2$ | psi |
|---|---|---|
| Masonry compressive strength | 6.44 | 934 |
| Masonry Young modulus | 1820 | 265000 |
| Concrete compressive strength | 25 | 3630 |
| Concrete Young modulus | 257400 | 3730000 |
| Concrete Poisson ratio | 0.2(unit less) | 0.2(unit less) |
| Weight on the whole floor | 97.5 (kg) | 214.5 (lbm) |
| Dead load on roof | 146000 | 21200000 |
| Bar yield strength | 400 | 58000 |
| Steel Poisson ratio | 0.3 (unit less) | 0.3 (unit less) |

**Table 4-2. Material parameters used in ABAQUS model (continue)**

The ABAQUS modeling analysis, shown in Figure 4-13, was able to simulate the crack pattern similar to the mechanism illustrated above as well as in Quiun's study. From left to right of the figure are the load application sequence, strain resistance from corner of the CM wall, and the shear crack observation on the wall. It is interesting to point out here that wall movement appears first to be resisted by the corners of the confining elements, causing strain at the tip of the wall as well as at the wall toe. Diagonal shear cracks occur as horizontal load reaches the maximum value.

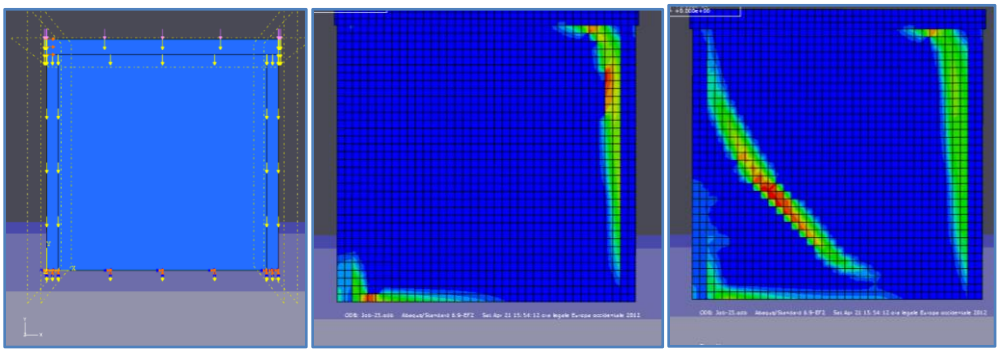

**Figure 4-13. FEM for CM shear wall**

The damage plasticity model was carried out in the finite element model for the solid shear wall tested by Quiun. Top displacement was recorded as 10mm on the top right of the wall. Figure 4-14 shows the base shear versus lateral top wall displacement.

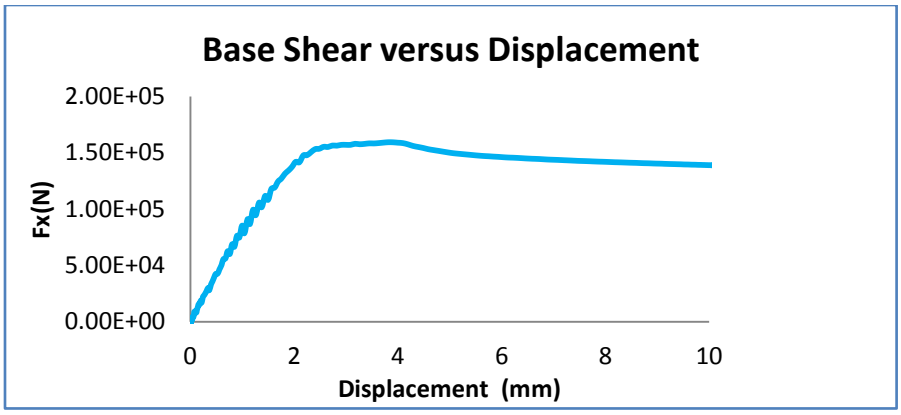


Figure 4-14. Base Shear versus displacement

Through this example/model 1, one important observation is made. It is the caution of material properties input.

### 4.3.2 Model 2: CM shear wall with opening

An analysis was also performed for a CM shear wall with an opening using ABAQUS FEA built in damage plasticity model. Parameters used in this model are the same as the ones listed on Table 4-2. The wall configuration was built to simulate the damage experienced and reported in the test done by Quiun. The experimental wall and the FE model included two confining tie-columns, one confining tie-beam, and one concrete lintel, as shown in Figure 4-15.

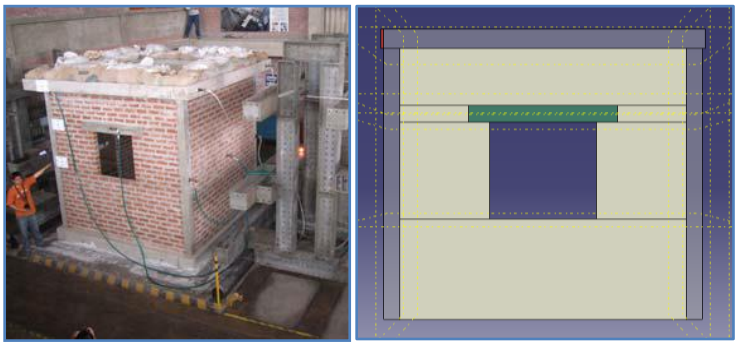

Figure 4-15. CM shear wall with opening.

In this model, a monotonic load was induced on the top wall so that top wall displacement achieved 5mm horizontally. The maximum displacement is measured at the top right corner of the wall, while shearing is experienced across the base. Figure 4-16 shows the wall response with tensile stresses form along a diagonal line resulting from the FE and from the experiment, respectively.

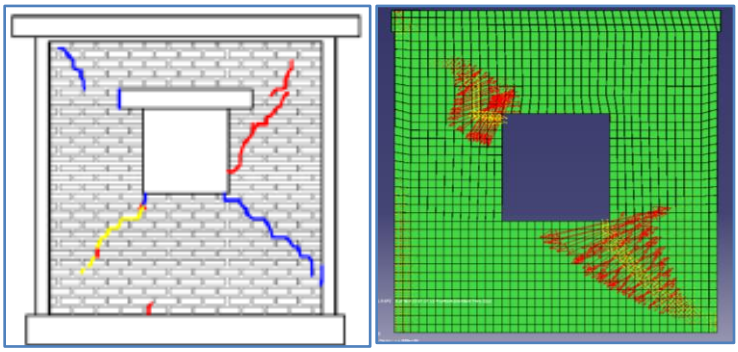

**Figure 4-16. Crack pattern observed from experiment and from FE model**

The ABAQUS FE result, shown in Figure 4-16, was able to produce the crack pattern similar to the mechanism illustrated on the left as reported in Quiun's study. The red arrows shown in Figure 4-16 on the right represent the tensile stresses when the measured displacement reached 5mm at the top right of the wall. The displacement used here is the top wall movement, which is typically much less than the base of wall movement during seismic activity for these types of structures.

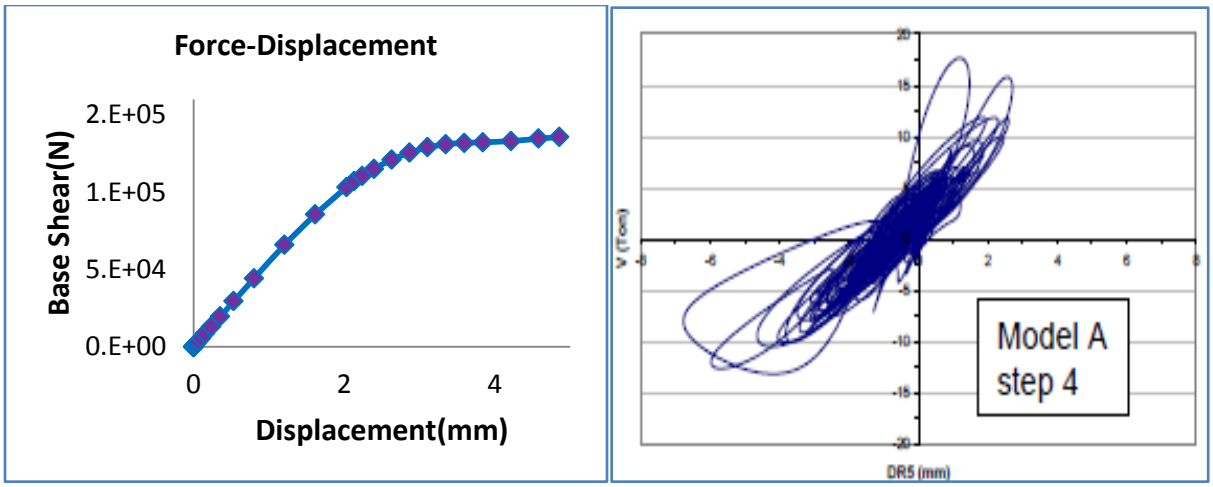


Figure 4-17. Shear capacity from FE model (left) and from experiment (right)

Lateral force in the numerical model was 136 kN [30 kips] shown in Figure 4-17 (left), while the experimental lateral force in Quiun's test was 150 KN [34 kips], as shown in Figure 4-17 (right). A numerical difference in value is reported in Table 4-3. This difference of 11% is likely accounted for by the extra stiffness given from the two perpendicular walls in Quiun's test. The adjustment made in reducing steel strength followed the observation mentioned in Section 4.3.1. This adjustment again is used solely for convergence purpose. Intuitively, if the model converges with the real steel strength, the difference in shear capacity could be less.

| | Experimental | Numerical Result | Difference |
|---|---|---|---|
| Maximum Base Shear (kN) | 151 | 136 | 11.0% |

Table 4-3. Model 2 result

The goal of this analysis is to seek the damage pattern, shown in the Figure 4-18. By enforcing the damage evolution introduced and discussed previously in Section 4.1.3 (also shown in Figure 4-12), the damage was captured for the model. Damage propagates through the wall in the same diagonal pattern distributed throughout the wall, as expected. This result enhances the validation of the damage evolution.

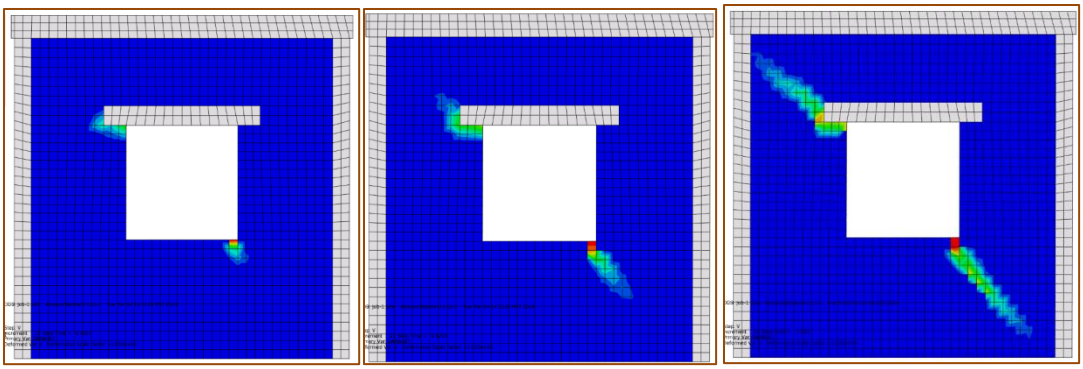

Figure 4-18. Damage propagates diagonally through the shear wall

### 4.3.3 Model 3: Scaled down CM shear wall

Seismic behavior of CM structures was investigated in 1997 by cooperation between the University of Ljublina, Slovenia and Universidad de Chile in Santiago, Chile. The study considered a relationship between prototype (a real structure) and model (a scaled down model to be tested) in such a way that in the model, masonry material should be prepared with the strength reduced at the geometric scale. By keeping other physical properties such as strain, specific mass, and damping equal to the original structure, the model should exhibit properties similar to the prototype. Using this scaling method for the stress-strain curve, the peak stress for the prototype and the peak stress of the testing model are related by a scaling factor, while the corresponding strain values at both peak stresses should be the same. It is important to note that by forcing such a relationship in a scaled down method, the principal requirement for modeling the dynamic behavior and failure mechanism of the test structure are automatically fulfilled, including similarity of mass and stiffness and similarity of failure mechanism (Tomazevic & Klemenc, 1997). Tomazevic and Klement presented the experimental results of scaled down modeling for a three story residentail building, and it has been considerd as a basis for the design

of the tested model, originally constructed in the Renca district, Santiago de Chile. Table 4-4 and Table 4-5 list the modeling factors, and material parameters used in their study, respectively.

| Physical quantity | Modeling factor |
|---|---|
| Length | 5 |
| Strength | 5 |
| Strain | 1 |
| Specific Weight | 1 |
| Displacement | 5 |
| Force | 125 |
| Time | 2.24 |
| Frequency | 0.45 |
| Velocity | 2.24 |
| Acceleration | 1 |

**Table 4-4. Scaling down factors used in modeling CM residential building in Chile, 1997**

| Wall Properties | mm | in |
|---|---|---|
| Tie column to ties column | 240 | 9.5 |
| Wall thickness | 50 | 2.0 |
| Ties beam to tie beam | 366 | 14.4 |
| Column width | 50 | 2 |
| Column thickness | 50 | 2 |
| Beam width | 50 | 2 |
| Beam thickness | 50 | 2 |
| Axial reinforcement bar | 2 (bars) | 2 (bars) |
| Rebar diameter | 3.2 | 0.125 |
| Horizontal reinforcement bar | 4 (bar) | 4 (bar) |
| Rebar yield strength | 199000 (MPa) | 28800000 (psi) |

**Table 4-5. Wall properties used in ABAQUS or scale down model.**

Based on this study by Tomazevic and Klemenc, a scaled down CM shear wall model finite element analysis was developed. The main purpose is to apply Lourenco's stress-strain material behavior into the scaled down model. Shown in Figure 4-19 is the analytical model (without the mesh displayed, mesh displayed with direction of movement, and finally, crack pattern diagonally distributed on the wall), consisting of two reinforced concrete tie elements, one reinforced concrete tie beam, and a confined masonry panel on a rigid reinforced concrete foundation.

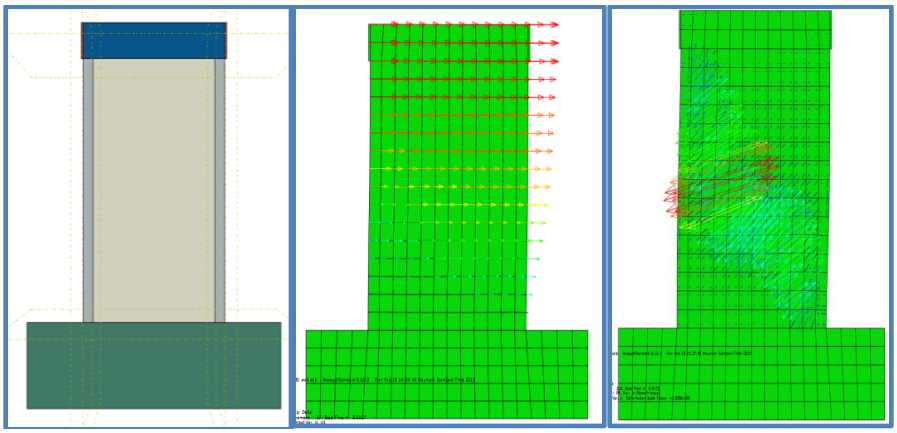

Figure 4-19. FE model for the scaled down CM shear wall

In the experimental scaled down model, compressive strength of the masonry panel was measured at 1.89 MPa [274 psi], tensile strength of masonry at 0.23 MPa [33.4 psi], and concrete compressive strength at 10 MPa [1450 psi]. Monotonic displacement was achieved by pushing on the top wall to a maximum of 4 mm [1.575 inch]. The aforementioned parameters and top wall displacement were used in the finite element analysis in this study. It was found that using the method from Lourenco (2004), the finite element model converged and reported a lateral force of 2.5 kN [0.56 kips], which is 9% different from the 2.29 kN [0.52 kips] measured in the experiment by Tomazevic and Klement. The overall results are reasonable for this type of material, and the finite element analysis model captured the complete crack pattern observed in the experiment. The FE model result, however, is stiffer than the one in the experiment. The explanation for this behavior is the possible sensitivity that occurs when forcing the plasticity behavior on the overall panel, while in reality, the plasticity behavior mostly occurs on the mortar layer itself. One positive observation from this model is that by using the mesh size approximately equals to half of the unit brick, the result seems not much deviate from the experimental result.

### 4.3.4 Model 4: FEA for scaled down Nguyen's CM shear wall 1

The analysis is conducted with 384 elements. Each element is a 4-node two-dimensional plane stress solid element available in the ABAQUS library, which has two integration points to provide the output. The surrounding concrete tie element in Nguyen's CM 1 is colored in pink to emphasize the difference in design as compared to the later mentioned CM2. Wall dimensions are listed in Table 3-2. Configuration for wall 1 is shown in Figure 4-20. Mesh size was created such that the element size is as close to half of unit brick and its surrounding mortar layer as possible. This mesh size follows the recommendation for continuum elements in composite masonry material according to (Lourenco, 1998) and also follows the observation discussed in Section 4.3.3. For instance, a half of the unit brick is about 3 inch by 3 inch, the mortar layer thickness is 0.375 inch, and the mesh built in the model then chosen based on 3.4 inch, 4 node elements. Cyclic in-plane shear load in terms of displacement control feeds to the FE model 0.001 in [0.00254 cm] per second for 1 cycles, 0.002 in [0.0051 cm]/s for 1 cycle, and 0.003 in [0.00762 cm]/s for 1 cycles. The reason for this loading input is to replicate the actual experiment process at the initial stage. The analysis did not apply the larger displacement rate (0.05 in [0.127 cm]/s for 3 cycles) as used in the experiment, due to the convergence limitation of the FEA. The pulling action from the actuator creates a wall movement that is shown by red arrows in Figure 4-20 c.

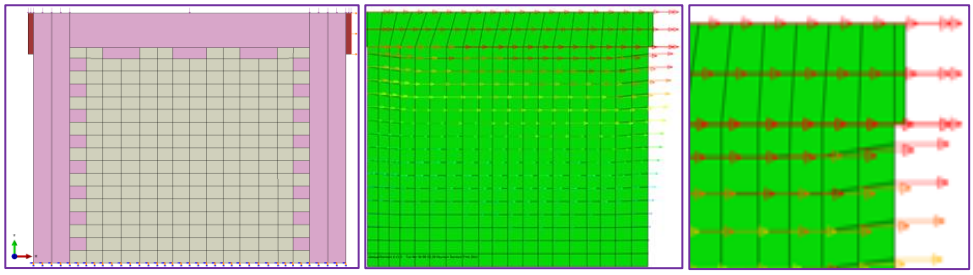

Figure 4-20 (a, b, and c). Nguyen CM wall 1 FE model

Material parameters used in FE model include internal state variables as listed in the following Table 4-6. The compression strength for the masonry prism is taken as 85% the average $f'm$ listed in Section 3.2.10, as a conservative value in modeling, and also as recommended by (Lourenco, 1998). The cohesion function serves as the damage evolution as stated in Section 4.1.3 for compression and tension.

| Material Properties | Psi | MPa | Source/Notes |
|---|---|---|---|
| Masonry compressive strength | 1400 | 9.65 | $0.85f'_m$ (Chen, 1982) |
| Masonry Young modulus | 680000 | 4690 | Average(Experimental value, and Code value 700*f'm) |
| Concrete compressive strength | 3000 | 20.77 | Experimental value |
| Concrete Young modulus | 3120000 | 21500 | Code value |
| Concrete Poisson ratio | 0.2(unit less) | 0.2(unit less) | |
| Distributed sand bags | 1500 (lbs-total) | 682(kg) | Roof load |
| Bar yield strength | 60000 | 414.00 | Factory/Mill sert specified value |
| Steel Poisson ratio | 0.2 (unit less) | 0.2 (unit less) | |
| Maximum tensile plastic strain rate | 0.0005 | 0.0005 | (Taqieddin, 2008) and (Ravindran, 2010) |
| Kinematic hardening modulus | 0 | 0 | Experimental $f'_m$ vs strain curve-$E_{ep}$ slope |

**Table 4-6. Material properties for FEA Nguyen CM Wall 1**

A computational FORTRAN language program was implemented for the ABAQUS UMAT option for an isotropic kinematic elastoplasticity using finite strain with damage. It is important to note here that for continuum models, the failure pattern characterized particularly on the mortar layer cannot be directly included because the unit and mortar geometries are not discretized in this chosen modeling analysis. The failure pattern, however, can be illustrated by the contour of the plastic strain upon deformation. For example, in tension loading, the observed failure pattern is in the crack direction defined by the perpendicular plane associated with the direction of the principal plastic strain. By introducing a damage variable as the internal state

variable, with the relationship between damage and plastic strain, the path when the damage travels will be captured.

As shown in the Figure 4-21, the damage pattern proceeds from the upper corner of the wall to the right end of the right hand side tie column. Since the masonry panel is of interest in this study, the figure solely shows the crack pattern in the masonry wall panel. As one can see, the model was able to capture the damage that occurs within one element. Thus, the model also shows the neighbor masonry units are not damaged as much. The illustration explains better the strut mechanism of the masonry panel after the yielding load is reached. In other words, by capturing the damage within an element, the stress is by definition now redistributed into the non-damaged media. From a design point of view, the non-damaged area is the "strut" that forms during plastic loading in the masonry panel. Follow the stress contour, the diagonal strut element is found to be $\frac{1}{3}$ of the masonry wall panel height according to the FE stress contour output shown in this Figure 4-21. This strut carries the plastic load in compression over its cross sectional area.

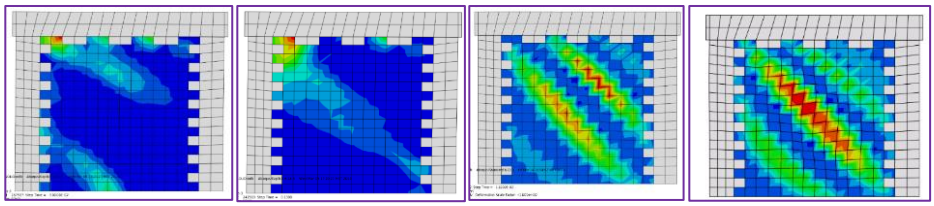

**Figure 4-21. Damage experienced in tensile loading for Nguyen's CM wall 1**

A study done by (Neto, Peric, & Owen, 2008) mentioned the complexity in numerical convergence for a FE model of damage coupled elastic-plastic behavior in solid mechanics. Recall in the built-in damage plasticity in ABAQUS, discussed in Section 4.1.3, it was found that in order to get convergence in numerical analysis, the damage would have to be forced to occur in the

length of more than one element. This in turn leads to the illutration of the entire "strut" being damaged, as shown in the following Figure 4-22, when tensile loading is applied in the opposite direction as compared to the previous example. The overall width of a strut that formed during the wall test upon loading generally aggreed with the one shown in Figure 4-21.

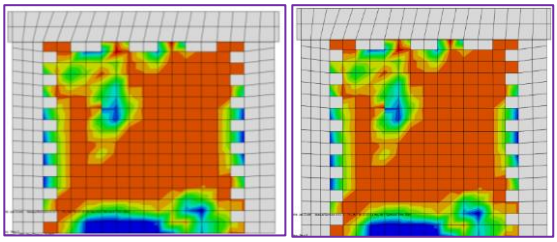

**Figure 4-22. Damage pattern forms in ABAQUS by using damage plasticity built in model**

The force-displacement curve is plotted as a result of this analysis. Figure 4-23 shows the shear resistance due to displacement loading of 0.001 inch [0.00254 cm]/s in the increment of 0.001 inch [0.00254 cm] within a time step. The shear resistance is 44 kips [195.7 kN] at 0.02 inch [0.05 cm] displacement, which is 4.8 kips [21.4 kN] stronger than the experimental test on the pushing/loading East direction. This is 14 kips stronger as compared to the experimental test on the pulling/loading West direction. The model was able to converge through 1.375 in [3.49cm] top wall displacement.

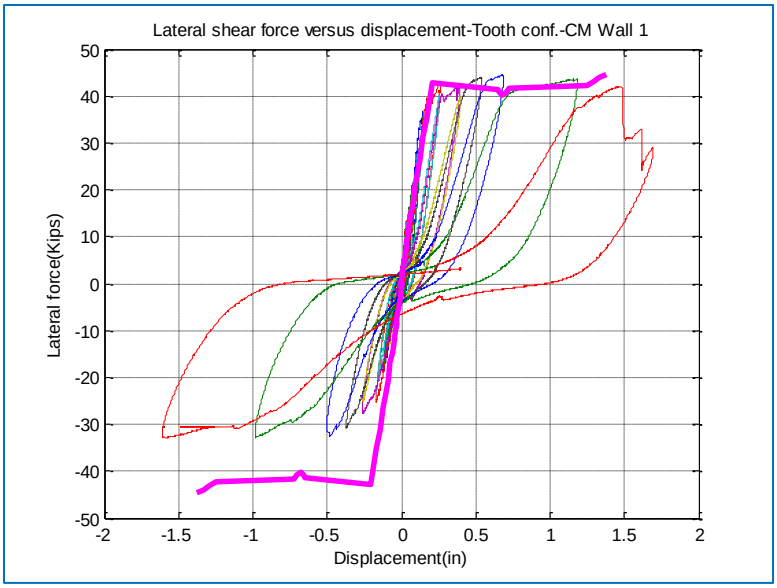


**Figure 4-23. FE model result on Nguyen CM Wall 1**

FEA was performed to apply two loading cycles at 0.001 inch [0.00254 cm] in 100 increments and 0.00125 inch [0.003175 cm] in 100 increments. The result is plotted on the following Figure 4-24. Showing on the left of Figure 4-24 is the comparison of the full two cycles (plotted in pink) and the wall hysteresis performance from experimental test results. Force resistance from the FE result is stronger in the loading West/pulling action while at the pushing/loading West, the result seems agrees with the experimental data. The positive observation from the FE cyclic loading is that the slope of the force decrease as expected due to damage occurrence, which again validate the FE model. The FEA, however, stops converging after two loading cycles.

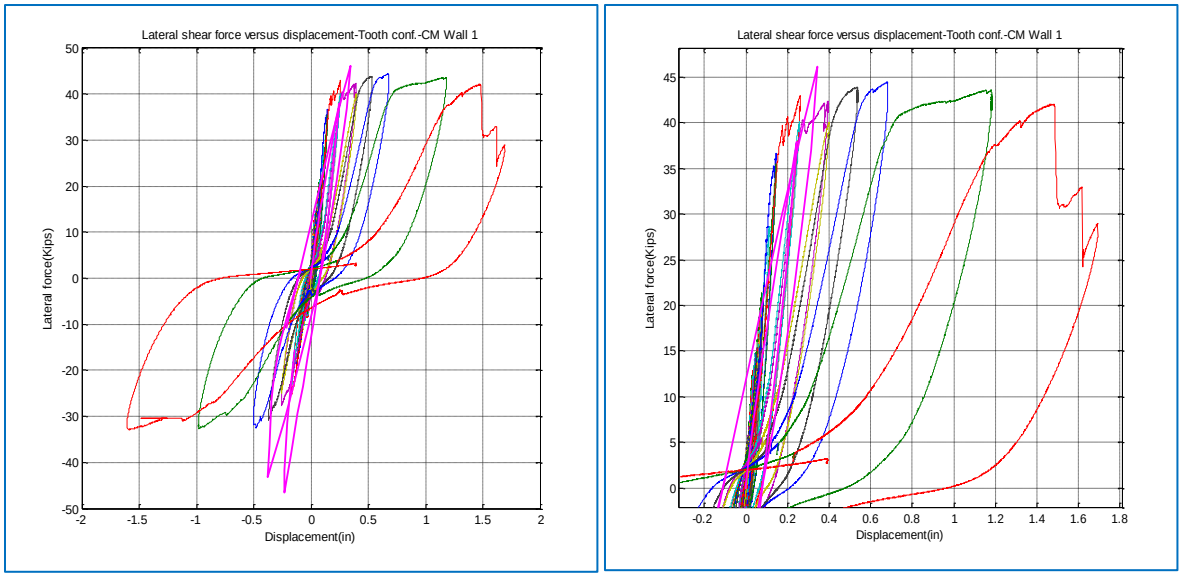


**Figure 4-24. FE model result -cyclic loading (left) and zoomed in result (right) for CM wall1**

### 4.3.5 Model 5: FEA for scaled down Nguyen's CM shear wall2

The second FE analysis carried out for CM wall 2 with 402 solid two dimensional plane stress elements. The difference in this model is the configuration of the tie elements, and the steel reinforcement. Shown in the following Figure 4-25 is the FE model set for CM wall 2. The masonry panel is surrounded by the concrete frame, and the loading steel cap is modeled as the two steel plates on both side of the top wall. Full contact is assumed between the loading plate and wall corner. As discussed in Chapter 4, it will be found that this assumption is valid. The same material properties listed in Table 4-6 are used. For simplicity, the reinforcement in the masonry wall panel was chosen to consist of solid continuum elements. The plane stress thickness for the reinforcement bars is the rebar diameter, while for the whole model the plane stress thickness is the thickness of the double wythe masonry wall, 7.625 inches [19.4 cm]. Figure 4-25 shows the image of the model and the reinforcement bar embedded into the model, respectively.

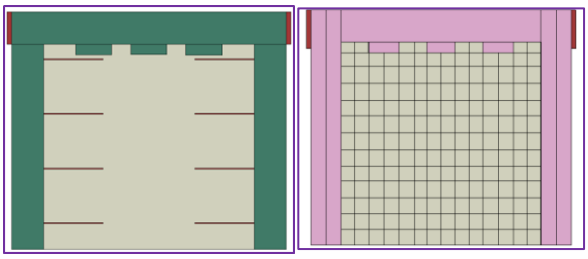

Figure 4-25. Nguyen CM wall 2 FE model

During tension loading, the FE model was able to capture the damage propagating diagonally through the masonry wall panel. The following Figure 4-26 illutrates a the tensile damage due to tensile loading in the analysis

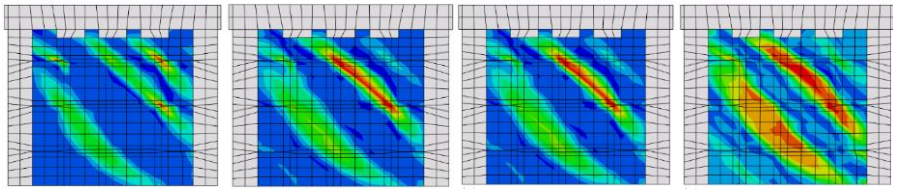

Figure 4-26. Damage experienced in tensile loading for Nguyen's CM wall 2

The experimental results for the CM wall will again be discussed later. Plotted here in Figure 4-27 is the force versus displacement chart from the resistance base shear due to lateral displacement on top of the wall. The model applied the displacement of 0.001 inch [0.00254 cm] and 0.003 inch [0.00762 cm] in each second in 1000 increments. The sum of these increments in turn allows the final for displacement to be represented and equivalent to a total displacement of 2.15 inch [0.5461 cm] in the test. This method of calibration is used by (Willam & Citto 2008) and (Teiquidinn 2008). As one can see, the homogenized solid continuum model provides a stiffer capacity for the wall. With the reinforcement bar and the mesh size significantly different in the model, as compared to CM1, the numerical analysis took much longer in converging time. However, the trend of steel hardening can be seen in the modeling result.

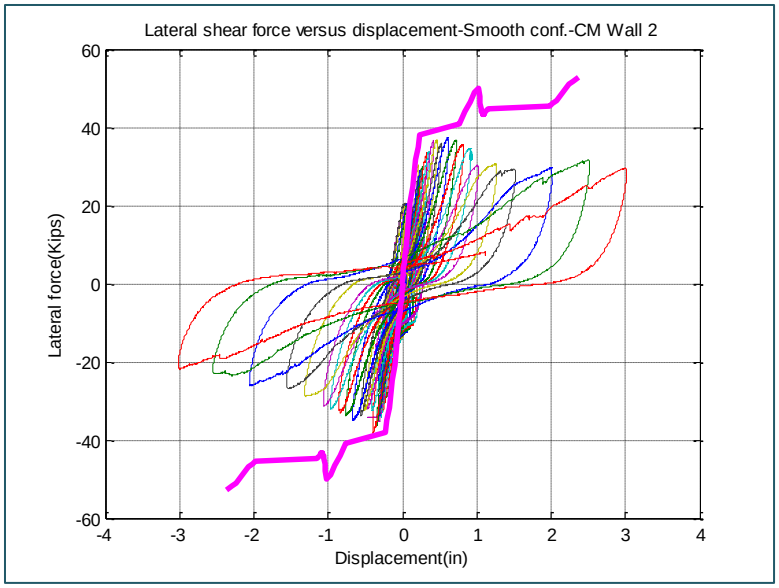


**Figure 4-27. FE model result on Nguyen CM Wall 2**

The FEA was further carried out with treating reinforcement as perfectly plastic and thus no strain hardening is input for steel properties. Figure 4-28 shows a better result in terms of force capacity between the model and the experimental result, the FEA maximum shear force result is 5 kips less than the shear force from the experimental result. The model, however, stopped converged as lateral displacement reached 1.75in. The hardening slope from displacement of 1.0 in to 1.75 in seems to agree with the hardening slope in steel in the experimental result. However, with plasticity in the reinforcement bar given perfectly plastic behavior, this hardening more so seems like a gradual increase of the effective stress in the masonry panel and the result from the rebar yielding.

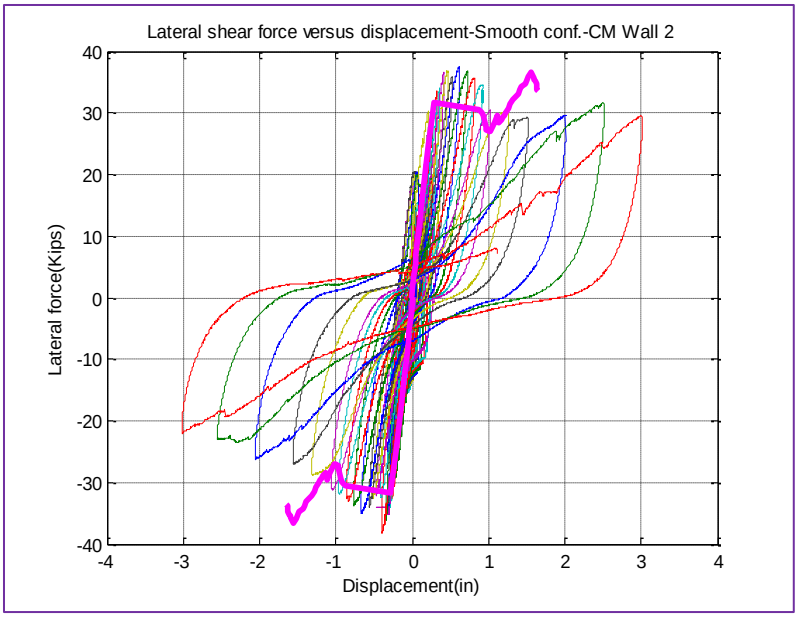


**Figure 4-28. FE model result on Nguyen CM Wall 2 with perfect plasticity behavior on steel**

The FE model was made for cyclic loading at 0.001 inch [0.00254 cm] in 100 increments and 0.003 inch [0.00762 cm] in 100 increments for CM wall2 as well. The result is shown in Figure 4-29. As one can see, the FE model result agrees well with the experimental. Variation on the loading West direction is consistent throughout the analysis. The FEA for this wall in cyclic loading also stops its convergence after two loading cycles.

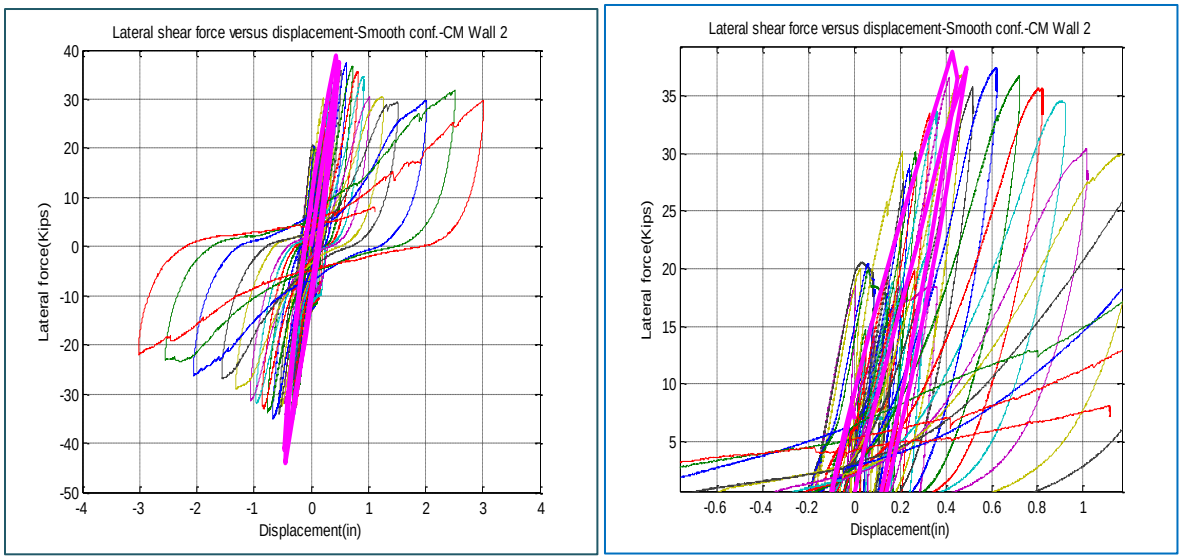


**Figure 4-29. FE model result -cyclic loading (left) and zoomed in result (right) for CM wall2**

### 4.3.6 Chapter summary

In this chapter, we analyze the behavior of the CM shear wall by the use of finite strain with damage contributing to the elastic domain and coupled to the plastic domain of a nonlinear material. By implementing into UMAT in ABAQUS a set of FORTRAN algorithms, the behavior of the CMs subjected to in plane loading was introduced. Numerical analysis seems much more straightforward by using step by step derivation. The plastic strain in the deformed configuration was able to be captured with the use of deformation gradient matrix multiplication. The damage pattern was able to be captured within one element, thus it can specify the location of crack patterns within the masonry panel. The FE analysis showed good agreement between numerical analysis and experimental tests. The damage variable shows a clear result on the tensile loading region. However, the maximum plastic strain rate for the damage function carried out for the analysis is 0.0005 in/in according to the observation from experimental tests and literature review for concrete modeling (Taqieddin, 2008) and (Ravindran, 2010). More investigation should be conducted to obtain better values for the upper limit of ultimate plastic strain for

tensile cracking in masonry prisms, as well as compression crushing plastic strain in masonry prisms. While the validation for an unreinforced masonry panel shows good agreement, the result for the reinforced masonry panel shows stronger shear capacity compared to the experimental result. Despite the fact that the second analysis in CM Wall 2 shows the better agreement in term of shear force, the hardening region remains as an open question. Originally, the effort of modeling using the continuum approach is to benefit the designer in terms of practice or to link the gap between complicated modeling and simple design. However, it is stressed to recognize that the micro modeling approach would perhaps provide the improved benefit of showing damage at each element, particularly at mortar joints. In addition, the effort put forth into calibrating the continuum panel using finite strain is relatively costly. A recommendation for future analysis is to start with the continuum solid brick, and continuum mortar with micro modeling approach. Future FE masonry micro modeling can apply this methodology to investigate the behavior of the mortar interface by treating the interface as the entire continuum with damage, rather than a “zero” thickness interface. Also, damage can be introduced to the stiffness degradation and can also be “decoupled” from the plastic analysis itself. Numerical complexity thus can be simplified. As for practical designer, the FORTRAN compiler might not be a “user friendly” tool. The good news is, for the code written for this CM model could be used in any masonry panel, with some regulation, of course. Material parameters, for instance, have to be input into the FE model in the order so that the sub-routine can correctly take the right value. Once again, the concept of using finite strain and damage is not new; however, in modeling homogenized brick prism none of the literature listed in this study has used this concept. Therefore, the analysis may not accomplish the best mechanic techniques

in capturing the model's behavior or in the computational coding. Future investigation thus should be dedicated to these findings, as well as investigate damage variable caused by plastic deformation.

# Chapter 5.
# Structural Reliability

## 5.1 General Concept in Reliability

Every engineering problem involves uncertainties, so engineers make use of the *theory of probability* (Benjamin & Cornell, 1970). The reliability of a structure is defined as the probability that it will not fail during a specified period of time under a given state of loading. The primary purpose of structural reliability is to control and manage the risk of failure, keeping it to acceptable levels.

A general probability of failure is defined as:

$$P_f = P(R \leq S) \qquad \text{Equation 5.1}$$

Under the view of the general limit state, G, the equation is then written as follows:

$$G = P(R, S) \qquad \text{Equation 5.2}$$

$$R = G(\boldsymbol{X}_i) \qquad \text{Equation 5.3}$$

$$S = G(\boldsymbol{Y}_i) \qquad \text{Equation 5.4}$$

Where, resistance is a function of $\boldsymbol{X}$, and loading effect is a function of $\boldsymbol{Y}$, both of which are vectors (indicated in boldface) in general. If the safety margin $M$ is the difference between the resistance factor $R$ and the demand/load $S$, (i.e., $M = R - S$) then the measurement of the reliability index of a structure, $\beta$,can be expressed in terms of the number of standard deviations, $\sigma_M$, between $\overline{M}$, the mean value of $M$, and $M = 0$.

$$\beta = \frac{\overline{\overline{M}}}{\sigma_M} \qquad \text{Equation 5.5}$$

The reliability analysis of a structure or the structural system then requires:

1. Identification of the basic random variables ***X,Y*** representing uncertainty as well as variability that influence the performance of the structures.
2. From equation (2), the definition of limit state function *G(R,S)* should be described in terms of basic random variables.
3. Estimation of a reliability measurement $\beta$ or determine the probability of failure of the structure or the system.

## 5.2 Case Study 1: Material Resistance Factor of Unit Brick under Concentric Compression Loading

Recent structural reliability analysis performed by Kazemi et al. on concrete masonry under concentric axial compression examined the reliability levels for masonry buildings constructed according to the process used in Canadian masonry standard CSA S304.1-04 [8]. As a result of this analysis, adjustments to the material resistance factor, $\phi_m$ were proposed. An increase from 0.6 to 0.65 was proposed for the factor regarding reinforced masonry (RM) and a decrease was proposed from 0.6 to 0.55 for unreinforced masonry (URM), which compare with the empirical values used in the *Building Code Requirements and Specifications for Masonry Structures* (MSJC, 2011). Kazemi's study used a separation function approach. A reasonable probability of failure is selected in comparison to an acceptable level of risk in other human activities. Thus, the reliability index β was first selected, as well as the corresponding mean and coefficient of variation for resistance and load so that proper combination of the material resistance factor and load factor is determined. The first order second moment method (FOSM) was used in the study.

The proposed factors reflect differing reliability indices found during the research of β=3.5 and β=3.8 for RM and URM, respectively. Statistical parameters for masonry resistance under compression according to (Kazemi, Mahoutian, Moosavi, & Korany, 2011) are expressed as:

$$\frac{R}{R_n} = \frac{G}{G_n} * \sqrt{\frac{M}{M_n}} * P * K \qquad \text{Equation 5.6}$$

$$V_R = \sqrt{V_G^2 + \frac{1}{4}V_M^2 + V_P^2 + V_K^2} \qquad \text{Equation 5.7}$$

where:

- *R* and $R_n$ are the average and the nominal member strengths, respectively.
- *G* and $G_n$ are the average and the nominal geometries, respectively.
- *M* and $M_n$ are the average and the nominal material strength, respectively.
- *P* is a professional ratio, and it includes the variations of the test procedure and specimen variability in addition to the model inaccuracy. Variability in *P* is expressed as a difference of the variation in the measured load due to the inaccuracy in the test measurement and the uncertainties with regard to the test measurement and the actual parameter of the test specimens.
- The workmanship factor K was taken in this analysis as 0.8 for unreinforced masonry and 0.9 for reinforced masonry with a coefficient of variation of 0.15 for both.

- $V_G$, $V_M$, $V_P$, and $V_K$ are the coefficients of variation for geometry, material, professional, and workmanship factors.

There are three sources of data that used in this present case study:

- the data provided by the experimental test carried out for a box building comprised of four CM walls led by Quiun in Peru (Quiun, 2011)
- the data recorded for the same unit bricks used in a series of the RCM test led by Blackard and Willam at the University of Colorado in 2008
- the material test data conducted in the current (Nguyen's) research.

The relationship between resistance factor and material coefficient variation is listed as following:

$$\emptyset = C\,\frac{R}{R_n}\,e^{-0.75\beta V_x} \qquad \text{Equation 5.8}$$

In Kazemi et al.'s study, the average and the nominal member strength $R/R_n$ was obtained from average material strength and average geometry of unit brick test. C is a correction factor that has a relationship with index β, live load and dead load (in this parametric study, live load and dead load ratio is set as 0.9). The expression of C is as followed:

$$C = \frac{1.086(1.0933+1.3936L/D)}{e^{0.0275\beta[1+0.03111\beta+(1+0.0311\beta)(L/D)]}} \qquad \text{Equation 5.9}$$

Using data adopted from concentric testing provided by Quiun's study in 2011, an effective variation on the material resistance factor $V_x$ is shown below, with the reliability index β first selected to range from 3.5 to 3.8 for reinforcement masonry (RM) and unreinforced masonry (URM), as assigned by the Canadian masonry standard CSA S304.1-04 (CSA, 2004). The assumption made in the current research is that the reliability index for CM structures will be

within the range from 3.5 to 3.8, or slightly higher, which seems reasonable since CM performance is better than URM structural performance (Riahi, 2007).

A few observations can be made from Figure 5-1. Since tests done by Quiun were performed on solely one type of masonry assemblage, the standard deviation is much lower compared to the large spread of standard deviation in the Kazemi et al. study. The resistance factor ranges from 0.84 to 0.89 for the hand-molded fired clay masonry units used in Quiun's test for CM structures. Since more data and experiments are needed for different types of masonry in order to understand the variability better, Figure 5-1 lists the standard deviations, which range from 0.09 to 0.18. As seen in Figure 5-1, the resistance factor behavior decreases with ascending value of standard deviation of material. It is worth pointing out here that the unit bricks used in Blackard's test in 2008 are the same as those used in Nguyen's test 2013, but results show a considerable wide range of capped brick material resistance, from 0.76 to 0.91 at the reliability index value of 3.5, as shown in Figure 5-1.

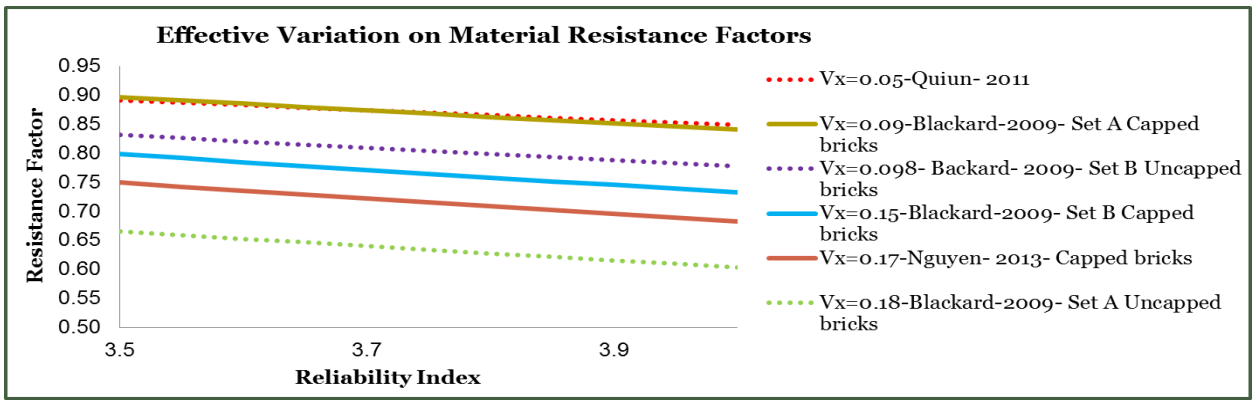


**Figure 5-1. Effect of material variability on calculated material resistance factor**

## 5.3 Case Study 2: Damage indexes and stiffness degradation for CM shear wall building

There are very few results available for CM wall testing, especially for experimental tests done for CM in single story or two story buildings. The lack of available data is a constraint to produce a

firm conclusion for a CM shear wall building under earthquake excitation. Fortunately, in work done by (Riahi, 2007) he reported the portfolio of 357 CM tests with given data for material properties, reinforcement details used in the tie elements, and in the wall panels. In Riahi's work, a macro force displacement curve for shear strength design in CM for single shear wall behavior was also proposed. The methodology used in Riahi's approach in proposing an estimate for shear stress in a CM shear wall is as follows:

First, several graphical and analytical tools were utilized to select the design variables for CM walls and to set the functional forms that appropriately relate them to the model parameters for the proposed shear strength capacity. Then, a visual search for relationships between model parameters such as cracking, maximum shear strength, and design variables (including: panel aspect ratio, tie column and transverse reinforcement, axial stress, etc.) was conducted in a series of plots that included all pairs of parameters versus design variables to search for trends.

The major limitation of such methodology for a scarce database of CM specimens is that trends are often obscure and hard to detect due to varying loading protocols, testing procedures, and diverse panel and confining elements variables. Such plots, in fact, only reveal trends when all variables other than the variable of interest are kept nearly constant. A method for separating data in test series with only a few changing variables was implemented by Haselton to develop an empirical model for reinforced concrete columns (Haselton, 2006). From Haselton's study, masonry shear strength was predicted on the basis of its compressive strength $f'_m$, considering 197 diagonal compression and masonry compression data from additional testing programs. Based on Haselton's approach, Riahi also found that geometry and reinforcement detailing of the panel and confining elements, loading protocol, the level of axial stress applied to the specimens,

scaling factors, recorded hysteretic responses, damage pattern, and failure mode are among the most important parameters included in the database to determine variables for the proposed equation for shear strength in CM walls (Riahi, 2007)

In this section, the data are taken from Riahi's report but solely focus on 22 single-story CM shear walls built with solid brick in order to match the same type of unit brick used in the experimental tests.

The data for 22 CM shear walls built by solid bricks are selected by excluding the following:

1. Specimens with more than two tie columns. This is to ensure that a single CM shear wall panel is to be analyzed.
2. Specimens with openings. This is to ensure a solid shear wall is analyzed
3. Specimens with simplified reinforcement detailing in tie columns, such as a single longitudinal rebar, spiral hoops, and panel reinforcement. This is to focus on common constructional practices used in placing reinforcement in tie columns for CM wall panels.

Constraints for the selection method (+) and criteria for the removal of data (-) in the CM model are listed as follows:

1. (-) Anomalies in recorded data
2. (+) Complete similitude of laws
3. (-) Unspecified or unclear parameters
4. (-) Unusual testing procedures
5. (+) Predetermined crack pattern/ only diagonal shear crack

6. (+) Set limit for axial stress
7. (-) Large aspect ratio
8. (+) Low column reinforcement ratio
9. (-) Other specimens: designs with interior columns and no column transverse reinforcement were not considered in the development of the model. This is also the case for specimens with hollow unit brick, which were excluded, since they indicated substantial different ultimate deformation capacities compared to the rest of the specimens according to Riahi's study.

Using these criteria and applying the constraints, the following set of data is listed to compare the calibrating methodology for shear capacity of CM walls with solid clay brick subjected to cyclic loading (the abbreviation "NG" indicates the data information was not applicable to the analysis).

| Aspect ratio h/L | Shear Strength $v_m$(MPa) [psi] | Maximum Shear Strength $v_{max}$(MPa) [psi] | Compression Stress $f'_m$(MPa) [psi] | Axial Stress $\sigma_v$(Mpa) [psi] | Concrete Compression Stress $f'_c$(Mpa) [psi] | Vertical Steel Tensile Strength $\rho_{vc}.f_{yvc}$(Mpa) [psi] | Confineed Steel Tensile Strength $\rho_{vc}.f_{yhc}$(Mpa) [psi] | Shear Strength at crack $v_{cr}$(Mpa) [psi] |
|---|---|---|---|---|---|---|---|---|
| 1 | 0.38[55] | 0.294[43] | 3.6[522] | 0.49[71] | 27.47[3984] | 6.81[988] | 0.59[86] | 0.31[45] |
| 0.9 | 1.11[161] | 0.320[46] | 5.6[812] | 0.2[29] | NG | 1.06[154] | 0.24[35] | 0.4[58] |
| 1.2 | 1.05[152] | 0.409[59] | 12.0[1740] | 0.408[59] | 20[2901] | 8.241195] | 1.49[216] | 0.68[99] |
| 0.7 | 0.44[64] | 0.350[51] | 2.6[377] | 0 | NG | NG | NG | 0.35[51] |
| 0.7 | 0.44[64] | 0.230[33] | 2.6[377] | 0 | NG | NG | NG | 0.23[33] |
| 0.7 | 0.44[64] | 0.140[20] | 2.6[377] | 0 | NG | NG | NG | 0.14[20] |
| 0.7 | 0.88[128] | 0.290[42] | 12.8[1856] | 0 | NG | NG | NG | 0.29[42] |
| 0.6 | 0.55[80] | 0.151[22] | 6.9[1001] | 0 | 23.9[3466] | 6.21[901] | 1.49[216] | 0.29[42] |
| 0.6 | 0.55[80] | 0.151[22] | 6.9[1001] | 0 | 23.9[3466] | 6.21[901] | 1.49[216] | 0.25[36[] |
| 1 | 0.69[100] | 0.193[28] | 10.0[1450] | 0 | 14.7[2132] | 11.8[1711] | 0.54[78] | 0.13[19] |
| 1 | 0.69[100] | 0.365[53] | 10.0[1450] | 0.472[68] | 14.7[2132] | 11.8[1711] | 0.54[78] | 0.34[49] |
| 1 | 0.38[55] | 0.128[19] | 5.1[740] | 0 | NG | 11.8[1711] | 1.66[241] | 0.19[28] |
| 1 | 0.38[55] | 0.130[19] | 5.1[740] | 0 | NG | 12.4[1789] | 3.5[508] | 0.22[32] |

| | | | | | | | | |
|---|---|---|---|---|---|---|---|---|
| 1 | 0.9[131] | 0.37[54] | 8.3[1204] | 0 | NG | NG | NG | 0.37[54] |
| 1.1 | 0.8[116] | 0.75[67] | 6.9[1001] | 0.907[132] | NG | NG | NG | 0.75[109] |
| 1 | 1.06[154] | 0.46[70] | 7.7[1117] | 0 | NG | NG | NG | 0.46[67] |
| 1 | 0.98[142] | 0.48[81] | 7.8[1131] | 0 | NG | NG | NG | 0.48[70] |
| 1 | 1.09[158] | 0.56[81] | 10.1[1465] | 0 | NG | NG | NG | 0.56[81] |
| 1 | 1.07[155] | 0.5[73] | 9.42[1366] | 0 | NG | NG | NG | 0.5[73] |

**Table 5-1. Material properties in CM walls with unit clay brick subjected to cyclic loading. Data source: (Riahi, 2007)**

Masonry compressive strength plays an important role in determining design shear strength. For example, in the allowable stress design approach for URM wall, the in-plane shear stress in a masonry wall according to the (MSJC, 2011) is the smallest value of $1.5f'_m{}^{0.5}$, 827 kPa [120 psi], or 0.255 MPa [37 psi]+ 0.45 $N_v/A_n$ for masonry laid in running bond, with $N_v$ is the axial load and $A_n$ is the loaded net area. This type of relationship holds true for CM structures. The following Table 5-2 lists the required shear strength for CM wall with respect to compressive strength:

| Country | Shear strength |
|---|---|
| Colombia | $f'_m{}^{0.5}$ |
| Mexico | $0.25*f'_m{}^{0.5}$ |
| Indonesia | $f'_m{}^{0.5}$ |

**Table 5-2. Shear Strength with respect to compressive strength**

The relationship between masonry shear strength and its compressive strength is shown in the green in Figure 5-2. This plot shows the real data and a green trend line. The analysis carried out by Riahi proposed a conservative relationship, predicting the shear strength shown by the red trend line. As one can see, there is still considerable scatter in the real data for solid unit

bricks as well as with the predicted relationship proposed by (Riahi, 2007). Data from this research is plotted in the red dots, which seems agree with the first data set in green.

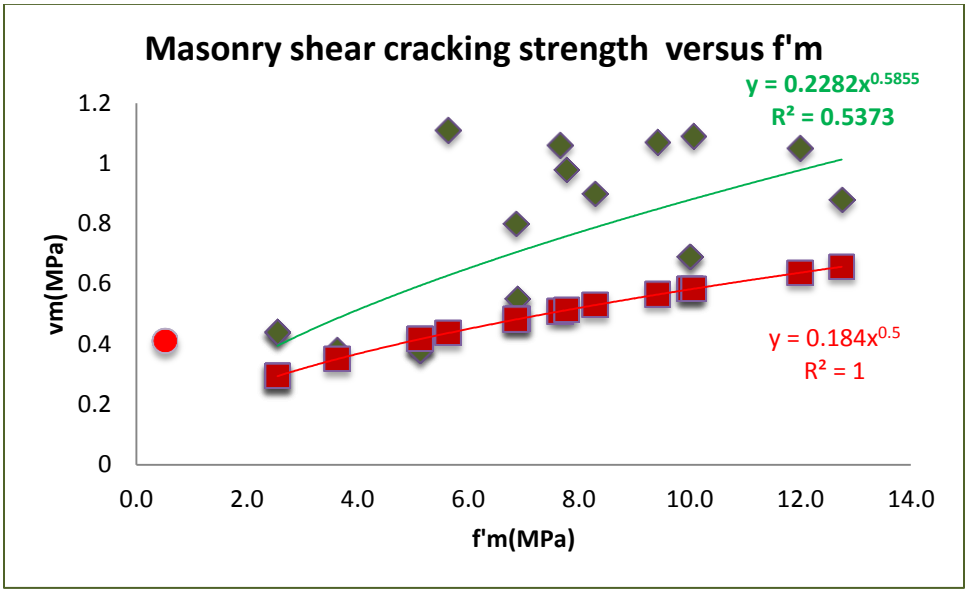


**Figure 5-2. Relationship between shear strength and compressive strength**

The relationship between shear strength in the wall panel and the shear strength in component testing is more straightforward and linearly related. Shown in the following Table 5-3 are the upper limits for shear strength in wall panels:

| Country | Shear Strength/Gross area wall |
|---|---|
| Chile | $0.35*\tau_m$, *with* $\tau_m$ *from diagonal shear component test* |
| Mexico | $(0.7)*(1.5)*\tau_m$, *with* $\tau_m$ *from diagonal shear component test* |
| Peru | $0.5*v'_m+0.23*$(Axial stress), *with* $\tau_m$ *is the shear resistance of masonry* |
| Argentina | $1.5*\tau_m$, *with* $\tau_m$ *is the nominal shear strength of the masonry from tests or from indicative values* |

**Table 5-3. Shear strength with respect to shear stress from component test**

The relationship between shear stress found from component testing and the shear strength at first crack in CM panels is shown in Figure 5-3. Despite the scatter shown on the plot,

this figure shows that the wall strength and the masonry component shear strength are two important factors affecting the performance of the wall up to cracking.

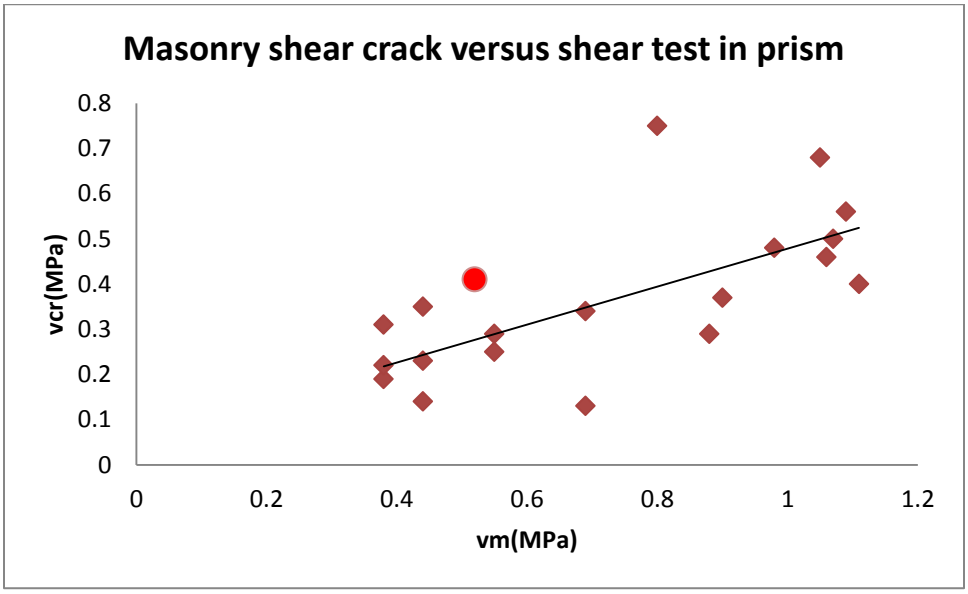


**Figure 5-3. Relationship between shear strength at crack and shear stress in the masonry prism**

In in-plane wall tests for CM walls, the impact from axial load applied on the wall panel is important by providing confinement for the wall, and thus enhancing the shear strength of the wall, as long as the vertical applied load is not great enough to crush the masonry before the first crack. The relationship of the shear strength in the CM wall and the axial stress should be linear, as shown in the following Figure 5-4

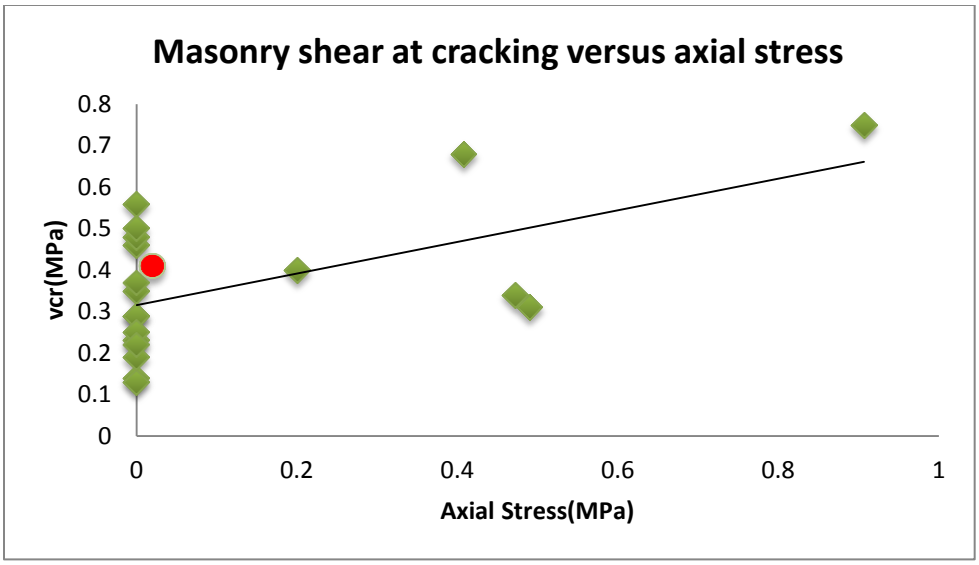


Figure 5-4. Relationship between shear strength at crack and the axial stress induced in wall panel

Riaha proposed a formula to predict maximum shear strength for the CM wall panel without accounting for the horizontal reinforcement effect in the tie columns. Figure 5-5 shows a good agreement between the experimental result and the value calculated from the proposed equation.

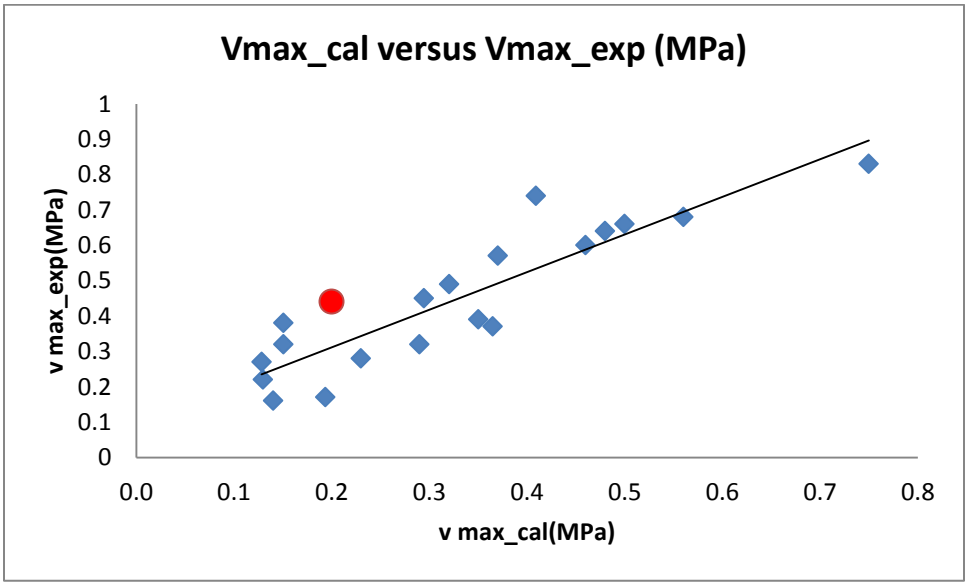


Figure 5-5. Verification for proposed shear strength and the experimental results

The intention in the current research was to improve the proposed shear strength prediction for CM shear wall done by Riaha. In order to do so, it is necessary to review the assumptions and the variables chosen for this current study, and in particular in defining the limit states. Overall, there are three limit states involved in this shear strength analysis done by (Riahi, 2007): (1) cracking, (2) maximum strength, and (3) ultimate deformation capacity. Variables for the analysis include:

1. axial stress
2. panel aspect ratio
3. masonry compressive strength
4. shear strength of the wall
5. column longitudinal reinforcement
6. masonry unit type.
7. masonry tensile strength.

There are gaps in the existing data in this variable list. The following items are key concerns which can be the emphases to improve the shear strength prediction and eliminate some of these gaps:

1. Contribution from the lateral reinforcement in tie columns.
2. Stiffness degradation during testing process and damage associated with the wall test
3. Connection from stiffness degradation and shear force in CM shear wall

In addressing concern 1, it was noted in these tests as well as previous ones that increasing the horizontal reinforcement does not increase the cracking shear strength or the cracking stiffness. If one plots the data given in Table 5-4, the plot shows no clear relationship.

| Wall ID | $V_{cr-exp}$ (MPa)[psi] | $\rho_{vc}.f_{yhc}$ (Mpa)[psi] | Reference |
|---|---|---|---|
| 1 | 0.49[71] | 0.69[100] | Beijing Ins |
| 3 | 0.78[113] | 0.68[99] | Beijing Ins |
| MR2 | 0.52[75] | 0.40[58] | San Bartolome |
| MR3 | 0.39[57] | 0.40[58] | San Bartolome |
| WBW-B | 0.52[75] | 0.52[75] | Sanchez et al. |

**Table 5-4. Effect of horizontal reinforcement in CM walls (source: (Alvarez, 1996))**

Nevertheless, the reinforcement in CM walls helps to produce a more uniform distribution of damage. More importantly, wall behavior after cracking significantly depends on the type and percentage of horizontal reinforcement (Alvarez, 1996). The presence of horizontal reinforcement produces an increase in the ultimate shear strength in the wall as much as 60% for standard horizontal reinforcement strength, from 0.4 Mpa [58 psi] to 1.06 Mpa [154 psi ]. In this research, the experimental test also showed that the wall with horizontal reinforcement has larger deformation capacity, and thus the ductility is higher when compared to the wall without horizontal reinforcement. This observation agrees with the Mexican code (NTC-M, 2004) which allows an increase in the shear strength of a masonry wall by as much as 25% if it contains a minimum specific horizontal reinforcment. Other Latin American regulations do not consider the influence of this reinforcement (Riahi, 2007).

Figure 5-6 shows the relationship of the ultimate shear strength and the horizontal reinforcement strength in CM walls using the data from (Alvarez, 1996) shown in Table 5-4. Despite a limitation of data, Figure 5-6 still shows a clear trend for the relationship between ultimate shear stress and horizontal reinforcement.

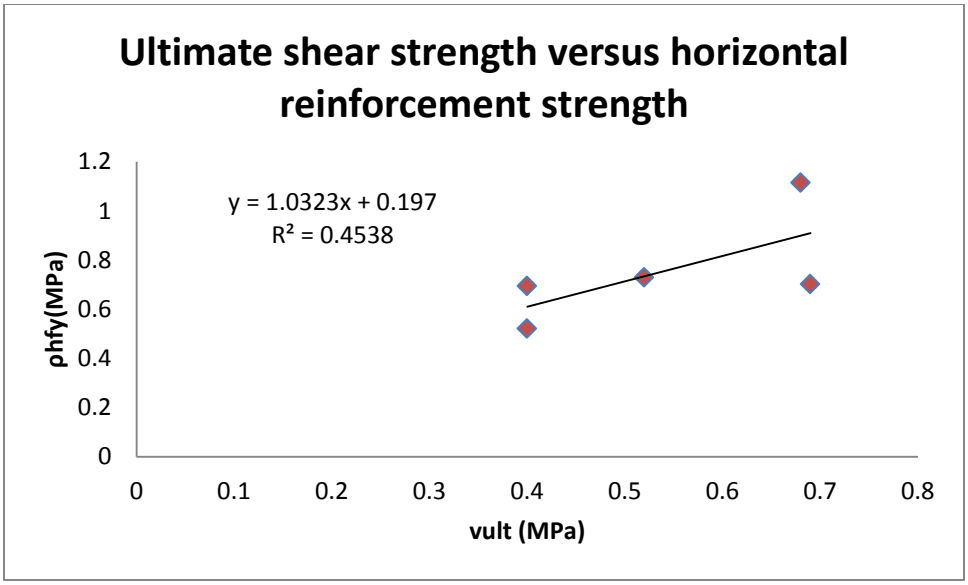


**Figure 5-6. Maximum shear strength versus horizontal reinforcement strength**

Along with the purpose of finding the shear strength, and to address the second concern in this case study, damage indices for shear walls are plotted versus the stiffness degradation. The study done by (Tomazevic & Klemenc, 1997) reported four damage indices denoted as $I_d$ to represent the different damage states of the CM walls subjected to in-plane loading. A four grade scale has been taken into account in Table 5-6.

| Damage Index | Damage Stage |
|---|---|
| $I_d$=0.25 | Initiation of the first crack in the middle part of the wall. Diagonally oriented crack passes mainly the mortar joints. Damage state at crack limit. |
| $I_d$=0.50 | Increased number of parallel cracks, oriented in both diagonals of the panel. The cracks mainly pass horizontal and vertical mortar joints. Damage state at the attained maximum resistant of the wall. |
| $I_d$=0.75 | Heavy damage. Increased number of diagonal oriented cracks with increased crack width, cracks passing also through the masonry units. The number of cracks is no longer increased, the damage however extends. Shearing of the concrete at the upper part of RC tie columns. |
| $I_d$=1.00 | Excessive increase in crack width in mortar joints, crushing of masonry units along the cracks Crushing of concrete tie columns due to the dowel action of the vertical reinforcement. Rupture of tension reinforcement or buckling of compressed reinforcements. Collapse of the specimen. |

**Table 5-5. Damage indices for damage stages for in-plane loading in CM walls (Tomazevic & Klemenc, 1997)**

From the data listed in Table 5-6, (which includes some data results from the tests listed in Table 5-4), the stiffness of CM shear walls was recorded as follows:

| Wall ID | $v_{cr}$ (MPa) [psi] | $v_{ultimat}$(MPa) | Distortion ($*10^{-4}$) (unit less) | Ultimate distortion ($*10^{-4}$) (unit less) | $K_e$(MPa) [ksi] | $K_u$(MPa) [ksi] |
|---|---|---|---|---|---|---|
| **1** | 0.49[71] | 0.702[102] | 2.3 | 24.7 | 2132.3[309] | 397.2[58] |
| **3** | 0.78[113] | 1.115[162] | 11.3 | 26.3 | 694.5[101] | 317.1[46] |
| **MR2** | 0.52[75] | 0.694[101] | 5.1 | 41.7 | 1023.5[149] | 193.1[28] |
| **MR3** | 0.39[57] | 0.520[75] | 5.7 | 17.1 | 687.2[100] | 310.2[45] |
| **WBW-B** | 0.52[75] | 0.729[106] | 12 | 74 | 480.7[70] | 118.6[17] |

**Table 5-6. Shear at crack and at ultimate stage-corresponding stiffness. Sources: (Alvarez, 1996)**

A relationship for stiffness degradation and the damage indices can then be determined from the fitted mean of the following Figure 5-7. Clearly, during experimental tests, one should expect a CM shear wall to reduce in stiffness as the damage index increases. The portion of the curve from a damage index of 0.25 to 1.0 shows a slow degradation of stiffness. Such behavior should be further examined, since CM shear wall tests should be subjected to an inelastic behavior in this region.

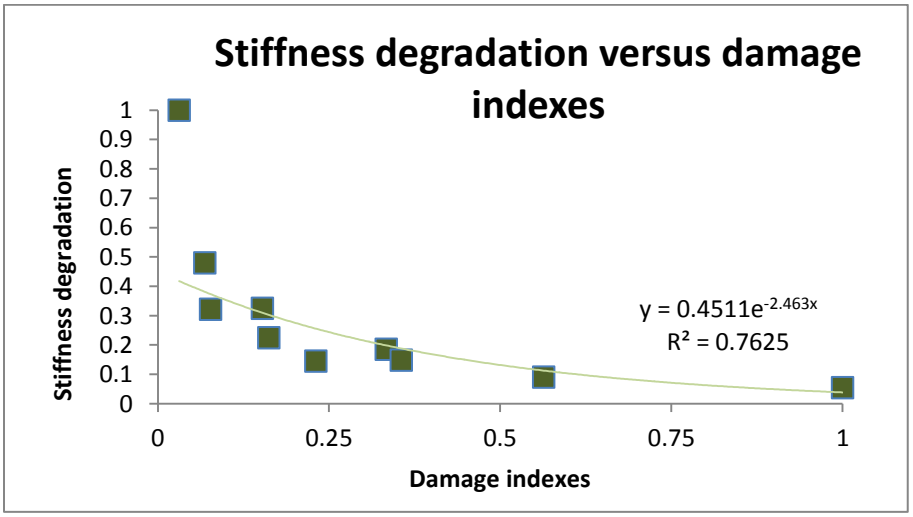


**Figure 5-7. Stiffness versus damage indexes in CM shear wall test. Data sources: (Alvarez, 1996)**

Owning the relationship from stiffness degradation and damage indexes, the relationship between the stiffness degradation and shear force predicted in CM shear wall is thus needed. This led to the following calculation. As mentioned in Table 5-5, Id=0.25 represent the damage stage at crack limit, Id=0.5 represent the damage stage at maximum resistance limit, Id=0.75 represents the damage prior to collapse stage. From the Figure 5-7, degradation 0.25, 0.175, and 0.1 are obtained. Shown in the following Table 5-7, the calculation for shear at crack and shear maximum then determined subsequently.

| Item | Value | Units | Reference/notes |
|---|---|---|---|
| I | 237168 | in4 | Bending around z axis |
| E | 112000 | psi | Prism test |
| Ke | 368.9 | kip/in | Conservatively neglect K_g |
| Ke_total | 368.9 | kip/in | 3EI/h^3 |
| K_crack | 92.2 | kip/in | 0.25Ke |
| K_max | 64.6 | kip/in | 0.175Ke |
| K_damage | 36.9 | kip/in | 0.1Ke |
| Allowable displacement | 0.6 | in | ASCE Table 12.12.1 |
| Displacement 1st guess | 0.25 | in | < 0.6 |
| Displacement 2st guess | 0.4 | in | < 0.6 |
| Shear at_crack | 23.1 | kips | K_crack* Δ1 |
| Shear_max | 32.3 | kips | K_max* Δ2 |
| Shear_ult | 22.1 | kips | K_damage *Δ_allow |

**Table 5-7. Evaluation of shear crack, shear max and shear ultimate**

In term of comparison, the following plots show the anticipated shear force at each stage.

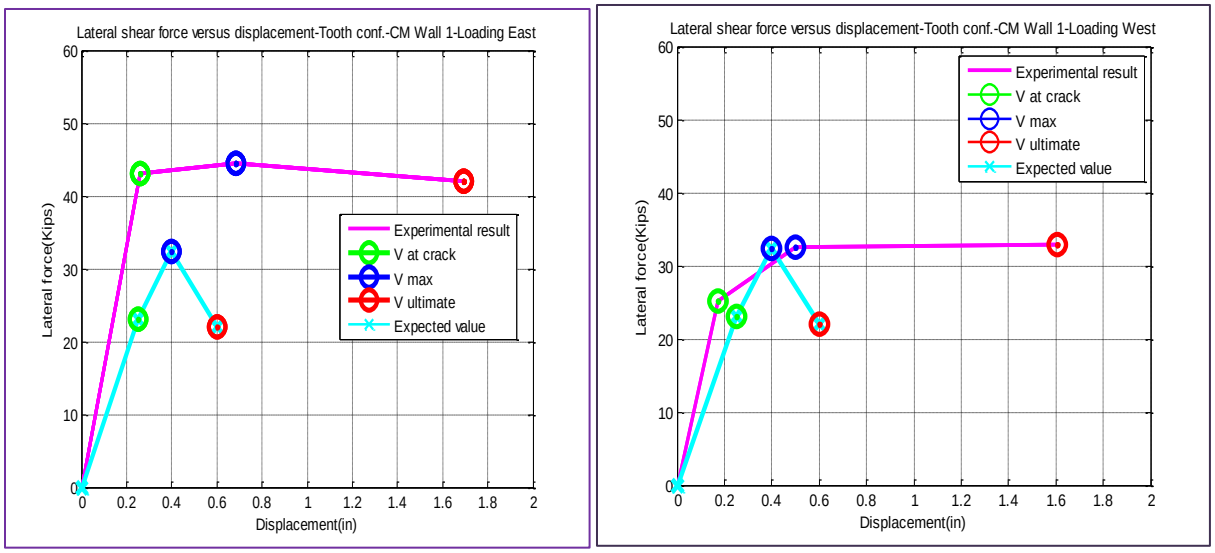


**Figure 5-8. Calculated CM wall 1 shear forces and experimental results**

The errors are listed in the following Table 5-8. Since the allowable displacement was taken from the code for cantilever masonry shear wall, which appears significant conservative as shown in the above figure. Thus, comparison only accounts for forces, especially on shear force at crack and maximum shear force. On the East side of CM Wall1, the calculation shows sufficient errors, while loading in the West direction, the comparison seems to agree well.

| CM Wall1 | | Loading East | | Loading West | |
|---|---|---|---|---|---|
| | V_Calculated | V_test | Error | V_test | Error |
| Shear at_crack (kips)[kN] | 23.1[103] | 42.9[191] | 46% | 25.2[112] | 9% |
| Shear_max (kips)[kN] | 32.3[144] | 44.5[198] | 27% | 32.5[145] | 1% |
| Shear_ult (kips)[kN] | 22.1[98.3] | 42.1[187] | 47% | 32.8[146] | 33% |

**Table 5-8. Comparison of calculated CM wall 1 shear force values and the experimental result**

Shear forces at crack and maximum stages were determined without accounting for the reinforcement in the wall. This omission follows the observation and discussion toward the beginning of Section 5.3.3. Shown in Figure 5-9 as well as Table 5-9, values for shear force at cracks at all stages agree very well. Again, ultimate displacement comparison is not mentioned here since the allowable displacement is used per ASCE7-10.

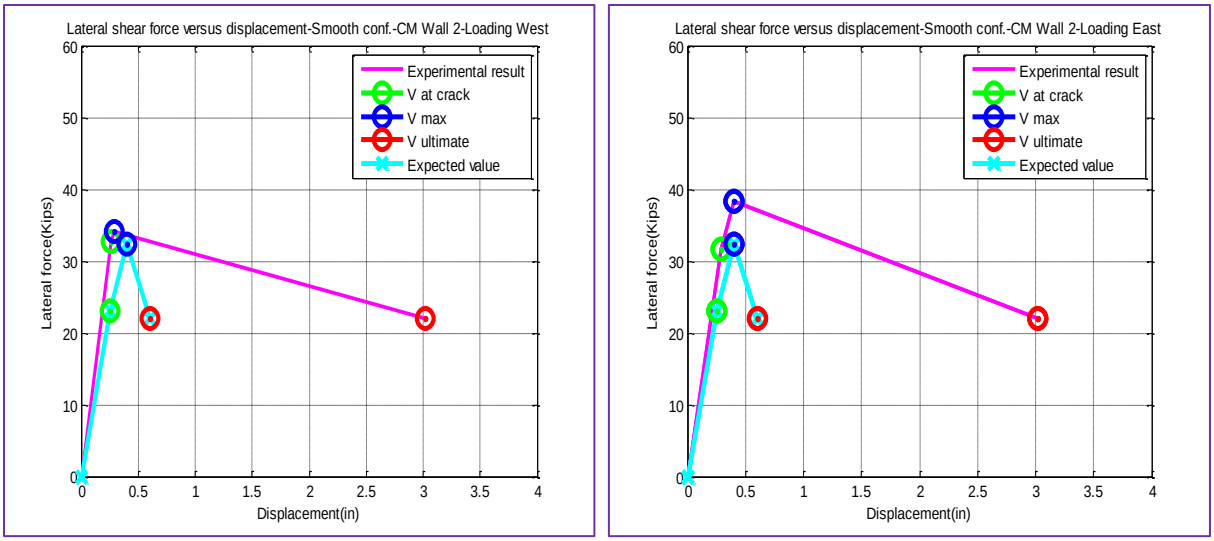


**Figure 5-9. Calculated CM wall 2 shear forces and experimental results**

| CM Wall2 | | Loading East | | Loading West | |
|---|---|---|---|---|---|
| | V_Calculated | V_test | Error | V_test | Error |
| Shear at_crack (kips)[kN] | 23.1[103] | 31.7[141] | 27% | 32.6[145] | 29% |
| Shear_max (kips)[kN] | 32.3[144] | 38.3[170] | 16% | 34.1[152] | 5% |
| Shear_ult (kips)[kN] | 22.1[98.3] | 21.9[97.4] | -1% | 21.9[97.4] | -1% |

**Table 5-9. Comparison of calculated CM wall 2 shear force values and the experimental result**

## 5.4 Case study 3: Preliminary Measurement of Reliability Index for Confined Masonry in Flexural Resistance

In contrast with Stewart & Lawrence's study, Varela-Rivera et al (2011) presented the experimental results of a study on the out-of-plane behavior of confined masonry walls. Three full scale rectangular walls were tested in the laboratory under monotonic uniform pressures. Three-side simple supported walls were considered. Wall specimens were selected based on the minimum requirements specified for confined masonry in the current Mexican Masonry Code. Uniform pressure was applied using an air bag to the CM wall panels. Mean flexural capacity of 0.14 Mpa [20 psi] for CM from Varela-Rivera was reported for tension parallel to bed joints. MSJC, 2011 recommended the use of Dawe and Seah's work in 1989 in calculation for flexural

tensile capacity for infill unreinforced masonry. Dawe and Seah, and latter work by Flangan and Bennett in 1999 reported the average ratio of observed capacity to predicted capacity of 0.98 and coefficient of variation of 28% for masonry infilled RC frames loaded out-of plane (MSJC, 2011). These values are used to obtain an example standard deviation to use with the results of the Varela-Rivera test. Using mean flexural capacity of 0.14 MPa [20 psi], and standard deviation 0.0392, an assumption is made here for a normal distribution in the Varela-Rivera test. Figure 5-10 contains the distributions of flexural capacity in CM, non-standardized in the left figure and standardized in the right plot.

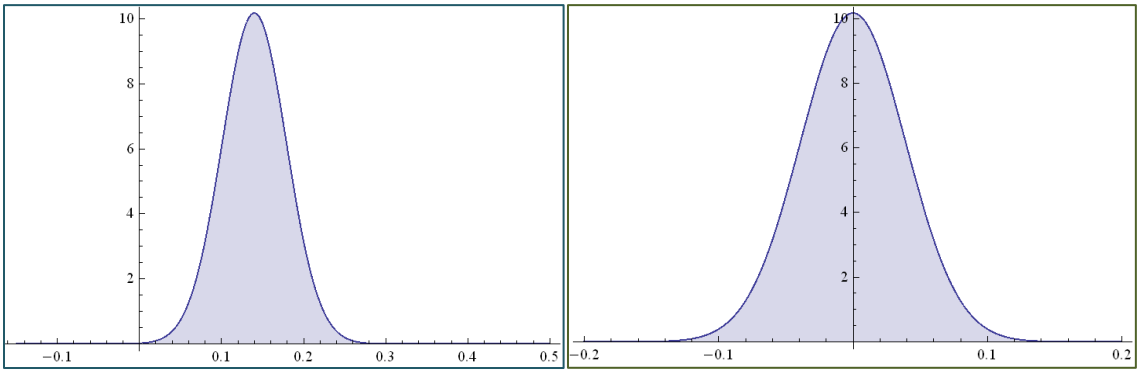


**Figure 5-10. Normal distribution of average and assumed standard deviation from Varela-Rivera results**

Instead of wind force used in Steward and Lawrence's study, air pressure applied the force though an air bag that imposed flexural moment to the wall. Varela-Rivera tested the wall with air bag pressure from 17.2 kPa [2 psi] and 34.2 kPa [5 psi] as measured by pressure transducers; the maximum pressure of 34.2 kPa [5psi] is chosen to find the maximum moment for the wall at mid height. The calculated limit state $G$ of flexural capacity random variable $X$ is based on Stewart & Lawrence's findings.

| Type | Values | Units | Values | Units |
|---|---|---|---|---|
| **Pressure** | 34.2 | kPa | 5 | psi |
| $Z_d$ | 829.7 | $mm^3/mm$ | 1.13 | $in^3/in$ |
| **Moment** | 15390 | N.mm/mm | - | - |
| **bulk density** | 6.54E-06 | $N/mm^3$ | - | - |
| ***G* mid height** | 0.00313 | | - | - |

**Table 5-10. Reported pressure and calculated parameters for flexural LS from Varela-Rivera test results**

A reliability index of $\beta$ = 3.49 is thus then obtained. This number implies a probability of failure of 0.024% at any bed joints for the 1.5 m x 3.0 m [60 in x 120 in] CM wall in the Varela-Rivera test with a specimen subjected to 34.2 kPa [5 psi] air pressure.

## 5.5 Chapter summary

In Chapter 5, the material resistance factor for unit brick under concentric compression loading and its relationship with the reliability factor was covered in a parametric study. Data from the experimental test covered in Chapter 3 was added to the study done by (Riahi, 2007) in finding a force-displacement curve for CM shear walls. The relationship between wall stiffness degradation and damage index was plotted to demonstrate the decay of wall stiffness as damage propagates. The probability of failure for CM walls subjected to out of plane loading was analyzed in case study 3. The author wishes to expand the study of finding probability of failure for in plane loading of CM shear walls as well. Such a study would require further testing, as the available information is not sufficient enough to perform the analysis. The portfolio reported in Riahi's study does not include the lateral displacement from experimental result. The testing done in the current study was only for two specimens, which is not sufficient enough to provide a distribution needed for reliability analysis.

# Chapter 6.
# Conclusion

## 6.1 Study contribution

This study covers the mechanical behavior, design, laboratory testing, and finite element analysis for solid CM shear walls in a one story building. Each chapter from Chapter 1 to Chapter 5 contains detailed description steps for each topic. They range from CM background, how to design a CM shear wall in accordance with the testing requirements, how to embed the modeling requirements for CM shear wall into finite element analysis, to what to consider in terms of general concepts for reliability. The objectives for the study have been covered with theory and detail procedure. In FEA, usually for nonlinear analysis for solid materials, the small strain theory is used. The different approach used in FE analysis in this study is applying the algorithm of large strain deformation to the behavior of the masonry panel. This application accounts for the higher order term of deformation to better capture the strain experience in the material, especially in rotation. By using the developed algorithm and implementing the damage evolution with respect to plastic strain rate, the model was able to predict a specific location of damage pattern on a CM shear wall subject in lateral loading. As part of a summary of lesson learned during this process, the following items are recommended for future research.

## 6.2 Study recommendation

For experimental research:

1. The strain gauges attached to rebar on both walls were damaged due to concrete vibration. Future experimental studies should look into installing strain gauges in a

protecting channel and tighten the channel to the side of wood frame, so that the vibration cannot damage the strain gauge.

2. In this experiment, sliding data was captured throughout two tests by the use of instrumentation. However, an investigation in irregularity of the strong floor should be carried out prior to building the specimen. A wider foundation pedestal could be constructed with additional posttensioning rods in the foundation at the front and back of test specimen.
3. Instrumentation setup for the tests was decided based on the available equipment at the time. The wall movement on both front and back faces was assumed to be identical, and thus the installation was done only on the front face of test specimen. Having another set of instrumentation setup would provide mode accurate reading data for the test.

For designers and code decision makers:

1. Through the experimental test results, it was shown that the lateral drift in a CM shear wall is greater than the MSJC Code allowable drift for an unreinforced masonry shear wall. This finding begs for more investigation for CM shear wall capacity.
2. The observation from the failure mechanism on both wall test clearly showed that the plastic hinge forms on CM shear wall is different than the failure mechanism on RC frame masonry infill shear wall. Again, this observation begs for more experimental tests to better capture the behavior of the CM shear walls.

Comparison on both allowable displacement and allowable shear force were made for both walls. By the use of this comparison, the designer can inform the building owners of which wall configuration suitable or recommended in term of force or displacement.

There is also other inspiration that the study's findings can provide. Together with some of the recommendations concluded in each chapter, the recommendations for future research attention are as following:

1. Rigidity and Massive thick wall

A wall that experiences lateral forces (e.g., an earthquake), the force could increase wall support movement, or shortening of the wall due to long term shrinkage or creep could increase the gap between the wall and its supports. These factors directly affect the out-of-plane resistance of the CM structure.

Evaluation of massive historic structures due to lateral loading is also an interesting topic and one where CM retrofit holds promise. It has been known that relatively thick masonry wall sections in many common historic building have enhanced resistance to out-of-plane loads due to arching effects, provided boundary conditions are fairly rigid. What is not known is how rigid the supports need to be. Thus *investigation* of lateral capacity and rigidity requirements for the supports in existing CM walls is necessary.

2. Slipping at the interface of reinforcement and mortar bed joint

The effects of confining member stiffness and confining stress on arching action to resist out-of-plane loading should be analyzed. Investigation into constraints for macro and micro modeling will be addressed as part of the scope of this study. Since limited research work is available to evaluate the effects of confining element and longitudinal reinforcement ratio on the behavior of the wall, it is essential to use FEA to confirm the effect of longitudinal bar size as well as confining element size on the lateral strength, initial stiffness, ductility, energy dissipation and cracking pattern.

3. Structural Reliability Current Challenges

This report has briefly introduced the range of the material resistance factor in CM. Parametric variation produced the range of selected reliability index from 3.5 to 3.8 for a masonry structure, within the range of CM tests done in Peru by Quiun (2011). The CM resistance factor ranges from 0.84 to 0.89 according to Quiun's material and ranges from 0.70 to 0.75 according to Nguyen's materials. The difference depends on coefficient of variation in material strength. Basic mechanics of CM have been introduced, as well as applications into modeling. However, laboratory testing data for CM is essential for this study to move forward. For instance, to analyze the response of CM structures in shear when the loads applied to the structure fluctuate with time and thus are of uncertain value of any point of time. While complexity of finite element modeling can be overcome without real testing data, FEM itself is still a major constraint. Probability estimation needs a combination of material testing data and relevant FEM analysis. Once experimental data are available, reliability of CM structures subjected to dynamic/seismic load can be accurately modeled.

It is also well known that workmanship has a significant impact on the performance of structural masonry, and its effect on reliability analysis is equally important. Most workmanship variability in masonry construction is related to mortar joint thickness and filling, walls being constructed level, plumb, and within tolerances compliant with the structural design, grouting techniques, and quality control procedures during construction. In reliability analysis a workmanship factor is used to account for these variations in construction quality. This factor has been reported as ranging from 1.0 for inspected masonry construction to 0.7 for uninspected masonry, with coefficients of variation of 0.1 and 0.2, respectively. Average workmanship factors

of 0.8 with 0.15 coefficient of variation and 0.8 with a coefficient of variation of 0.2 have both been suggested and used in analyses (Kazemi, Mahoutian, Moosavi, & Korany, 2011). A question remains as to whether the workmanship relationship factor for CM lies within the range from 0.7-1.0 as aforementioned. Owning the fact that the construction sequences in RM, CM, or URM involve the detail from the mason, the author believes that the workmanship factor for CM also lies from 0.7 to 1.0.

## SELECTED REFERENCES


Abaqus. (2009). *Abaqus 6.9/CAE Extended Functionality EF2 Manual.* USA: Dassault Systems Corporation.

Alvarez, J. (1996). Some topics on the seismic behavior of confined structures. *Eleventh World Conference on Earthquake Engineering* (p. 180). Elsevier.

Amadei, B., Sture, S., Saeb, S., & Atkinson, H. (1989). *An evaluation of masonry joint shear strength in existing buildings. Report to NSF.* Boulder: Dept. of Civil, Environmental and Architectual Engineering, University of Colorado at Boulder.

ASCE-7. (2005). *Minimum Design Loads for Buildings and Other Structures.* Virginia: American Society of Civil Engineers.

ASTM. (2005). *"Standard Specification for Mortar for Unit Masonry"-Standard C270-05a-Annual Book of ASTM Standards, Volumne 04.05.* West Conshohocken, Pennylvania: ASTM International.

Bartolome, A. S., & Quiun, D. (1992). Seismic behavior of a three story scale confined masonry structure. *Thenth World Conference on Earthquake Engineering.* Madrid. Spain.

Bazant, Z. P., Pan, J., & Pijaudier-Cabot, G. (1987). Softening in reinforced concrete beams and frames. *Journal of Structural Engineering*, 2333-2347.

Bazant, Z., & Oh, B. (1983). Crack band theory for fracture of concrete. *Materials and Structures, RILEM*, 155-177.

Benjamin, & Cornell. (1970). *Probability, Statistics, and Decision for Civil Engineers.* New York: McGraw-Hill.

Brandow, G. E., Ekwueme, C. G., & Hart, C. G. (2007). *2006 Design of Reinforced Masonry Structures.* Citrus Heights: Concrete Masonry Association of California and Nevada.

Brzev et al. (2010). *Performance of Confined Masonry Building in the February 71, 2010 Chile Earthquake.* EERI.

Brzev, S. (2008). *Earthquake Resistant- Confined Masonry Construction.* Burnaby, Canada: NICEES.

Build Change. (2010, May 10). *Earthquake Resistant Design and Construction Guideline.* Retrieved May 23, 2010, from Build Change: www.buildchange.org

Chen, W. (1982). *Plasticity in reinforced concrete.* New York: McGaw Hill.

Chow, C. L., & Wang, J. (1988). Ductile fracture characterization with an anisotropic continuum damage theory. *Engineering Fracture Mechanics*, 547.

CSA. (2004). *C. S. Association, S304.1-04 Design of Masonry Structures.* Mississauga,Ontario,Canada: Canadian Standard Association.

Drysdale et al. (1999). *Masonry Structures Behavior and Design.* Boulder, Colorado: The Masonry Society.

Gambarotta, L., & Lagomarsino, S. (1997). Damage Models for The seismic Response of Bric Masonry Shear Wall (Part 1): The Motar Joint Model and Its Applications. *Earthquake Enigneering and Structural Dynamics, Vol. 26*, 423-439.

Hamburger and Meyer. (2006). The Performance of Steel-Frame Buildings. *Earthquake Spectra, Vol 22, No S2, EERI*.

Haselton, C. (2006). *Beam-Column element model calibrated for predicting flexural response leading to global collapse of RC frame buildings.* Standford University.

Helwany, S. (2007). *Applied Soil Mechanics with ABAQUS aplications.* New Jersey: John Wiley & Sons, Inc.

Ibrar, M., Naseer, A., & Ashraf, M. (2012). Experimental Study of Confined Masonry: Effect Size of Confining Element and Steel Ratio. *ACI Structural and Materials Journal, Submitted paper in 2012*, 24.

Irmies, M. T. (2000). Cyclic Loading Behavior of Perforated Unreinforced Masonry Model. *12th World Conference on Earthquake Engineering.* Aucland, New Zealand.

Kachanov, L. M. (1986). *Introduction to continuum damage mechanics.* Doorrecht, Netherlands: Martinus Nijhoff .

Kazemi, S., Mahoutian, M., Moosavi, H., & Korany, Y. (2011). Relibility Analysis of Masonry Members under Compression. *ASCE Structural Congress*.

Lee, J., & Fenves, G. (2001). A return mapping algorithm for plastic-damage models: 3-D and plane stress formulation. *Int. J. Num. Meth. Eng.*, 581.

Lemaitre, J., & Chaboche, J.-L. (1990). *Mechanics of Solid Materials.* Cambridge: Cambridge University Press.

Lotfi and Shing. (1994). Interface Model Applied to Fracture of Masonry Structures. *Journal of Structural Engineering, Vol. 120, No. 1*, 4747.

Lourenco. (1998). *Experimental and Numerical Issues in The Modeling of The Mechanical Behaviour of Masonry.* Cimne, Barcelona: Structural Analysis of Historical Construction II.

Lourenco, P. B., Borst, R. d., & Rots, J. G. (1997). A Plane Stress Softening Plasticity Model for Orthotropic Materials. *International Journal for Numerical Methods in Engineering, Vol. 40*, 4033-4057.

Lubliner. (1990). *Plasticity theory.* New York: MacMillan.

Mehrabi, A. B., Shing, P. B., Schuller, M. P., & Noland, J. L. (1994). *Performance of masonry infilled reinforced concrete frame under in-plane lateral loads.* Boulder: University of Colorado at Bouder.

Midas FEA. (2009). *Nonlinear and detail Finite Element Analysis System for Civil Structures Manual: Analysis and Algorithm version 2.9.6.*

MSJC. (2011). *Building Code Requirement for Masonry Structures.* Boulder: The Masonry Society.

Neto, E. d., Peric, D., & Owen, D. (2008). *Computational methosd for plasticity-Theory and applications.* West Sussex, United Kingdom: John Willey and Sons.

NTC-M. (2004). *Normas Tecnicas Complementaria para Diseno y Construccction de Estructuras de Mamposteria (Technical Norms for Designs and Construction of Masonry Structures).* Mexico D.F.

Oller, S., Oliver, J., Onate, E., & Lubliner, J. (1990). Finite element nonlinear analysis of concrete structures using a plastic damage model. *Eng. Fracture Mechanics*, 219-231.

Ozbolt, J., & Ananiev, S. (2013). *Scalar damage model for concrete without explicit evolution law.* Pfaffenwaldring, Germany: Institute of Construction Materials, University of Stuttgart.

Ozbolt, J., Li, Y., & Kozar, I. (2001). Microplane Model for Concrete with Relaxed Kinematic Constraint. *International Journal of Solids and Structures*, 2683-2711.

Quiun, D. (2011). Shaking Table Test Perforemed on Low Quality Confined Masonry Models: An International Cooperation Improvement of Seismic Behavior. *The Eleventh North American Masonry Conference.* Minneappolis: The Masonry Society.

Ravindran, S. (2010). *Prediction of material damage in orthotropic metals for virtual structural testing .* PhD Dissertation at Cranfield University .

Regueiro, R. (2014). *Computational Finite Inelasticity and Multiphase Mechanics.* Boulder: Class Notes.

Riahi, Z. (2007). *Backbone model for confined masonry walls for performance based seismic design.* The University of British Columbia.

Roberto et al. (2011). *Seismic Design Guide for Low- Rise Confined Masonry Buildings.* World Housing Encyclopedia, EERI and IAEE (Draft).

Sarrafi, B., & Eshghi, S. (2012). Behavior of Clay Brick Confined Masonry Wall Under Cyclic Loads. *TMS_Journal Vol30No1*, 9-12.

Simo, J. C., & Ju, J. W. (1987). Strain and stress-based continuum damage model. Part I: Formulation. *International Journal Solids Structures*, 821-840.

SIMULIA, A. 6. (2009). *Abaqus/CAE Extended Functionality EF2 Manual.* USA: Dassault Systems Corporation.

Stavridis, A., & Shing, P. (2010). *Finite Element Modeling of Nonlinear Behavior of Masonry Infilled RC Frames.* ASCE Journal of Structural Engineering.

Stewart, M. G., & Lawrence, S. (2000). Bond Strength Variability and Structural Reliability. *12th International Brick/Block Masonry .* MMrid, Spain.

Tanner, J. E., & Carboni, A. (2011). Performance of Masonry Buildings in 2010 Chile (Maule) Earthquake. *The 11th North American Masonry Conference* (p. 1). Minneapolis, MN: The Masonry Society.

Taqieddin, Z. (2008). *Elasto- Plastic Damage Modeling of Reinforced Concrete.* Baton Rouge: Louisiana State University.

Tarque-Ruiz, S. N. (2011). *Numerical Modeling of the Seismic Behaviour of Adobe Buildings.*

Tomazevic, M., & Klemenc, I. (1997). *Seismic Behavior of Confined Masonry Buildings.* Ljubljana: Slovenian National Building and Civil Engineering Institute.

Varela-Rivera et al. (2011). Experimental Behaviors of three Confined Masonry Walls Subjected to Uniform Our-of-Plane Pressures. *Eleventh North American Masonry Conference*, (p. 3). Minneapolis, MN.

Voyiadjis, G. Z., & Kattan, P. I. (1989). Local approach to damage in elastoplastic metal matrix composites. *Int.J. Damage Mechanics*, 92-114.

Voyiadjis, G. Z., & Kattan, P. I. (2006). *Advances in Damage Mechanics:Metals and Metal Matrix Composites, with an Introduction to Fabric Tensors.* Oxford: Elsevier.

Yoshimura, K., Kikuchi, K., Okamoto, T., & Sanchez, T. (1996). Effect of vertical and horizontal wall reinforcement on seismic behavior of confined masonry walls. *Eleventh World Conference on Earthquake Engineering.*

# Chapter 7.
## Appendix A

1. Diagonal shear test values

| NTC- 404 for diagonal shear test. |
|---|
| Shear matrix: 0.0653 0.0673 0.1011 0.0610 |
| Mean value: S = 0.0737 |
| COV_S = 3.4210e-04 |
| Reported value after correction, see formula in NTC-404: S_m = 0.0736 |

SEISMIC DESIGN GUIDE FOR CONFINDE MASONRY BUILDINGS-EERI, 2011-APPENDIX A

Building code NTC-M, 2004

Table1. Seismic Shear Strength Computation

| Wall density check | Designation | Value | Unit | Notes/References |
|---|---|---|---|---|
| Wall cross-sectional area in N-S direction | $Aw_{N-S}$ | 9.33 | ft2 | N-S---> Seismic ditn |
| Wall cross-sectional area in E-W direction | $Aw_{E-W}$ | 18.7 | ft2 | |
| Wall density in N-S direction | $d_{N-S}$ | 10.4% | OK | |
| Wall density in E-W direction | $d_{E-W}$ | 20.7% | OK | |
| Average compressive stress due to gravity load | σ | 0.72 | ksi | |
| Basic shear strength v* | v* | 73.6 | psi | Diagonal shear test |
| Strength reduction factor(neglect0.7 factor) | $F_R$ | 1 | | NTC-M, 2004-Table5 |
| Load factor | $F_c$ | 1.1 | | |
| Masonry shear strength v | v | 73.6 | psi | Diagonal shear test |
| Seismic Shear Strength VR | $V_R$ | 98.9 | kips | |
| Strength (3 WALLS) | $F_RV_R$ | 98.9 | Kips | |
| Max strength (1 WALLS) | $F_RV_R$ | 33.0 | Kips | NTC-M, 2004 |

SEISMIC DESIGN ORDINARY PLAIN URM SHEAR WALL-AND APPENDIZ B DESIGN FOR MASONRY INFILL
BUILDING CODE: MSJC-SECTION 3.2 ACCORDING TO APPENDIX B, SECTION B.1

Table 2. Shear Strength Calculation

| Item | Designation | Value | Unit | References |
|---|---|---|---|---|
| Axial Compresion $N_u$ | $N_u$ | 1.5 | kips | Sand bags |
| Strength reduction factor | Φ | 1 | | MSJC-B.1.4/neglect for max val |
| Nominal strength | | 8.2 | kips | MSJC-3.2.4 |
| Unfactored design strength | $\Phi V_n$ | 49.4 | kips | MSJC-3.2.4.e |
| $3.8A_n f'm^{0.5}$ | | 14 | kips | MSJC-3.2.4.a |
| $300A_n$ | | 27.45 | kips | MSJC-3.2.4.b |
| $90A_{nv}+0.45N_u$ | | 8.2 | kip/ft | MSJC-3.2.4.e |
| fr | | 38.0 | psi | Bond wrench test |
| fr*An*L | $\Phi V_n$ | 20.9 | kips | Flexural value controls |

Reinforcement scheme checks

TIE ELEMENT TO WALL- INTERFACE design-EERI, 2011-APPENDIX A
Building code NT-E, 2003

Table1. Vertical tie-element Spacing check

| Tie Column | Value | Unit | SI Value | | Notes/References |
|---|---|---|---|---|---|
| Column Quantity | 2 | Columns | | | |
| Spacing | 6.0 | ft | | | |
| Checking | OK | | | | |
| Column Length | 8 | in | 203.2 | mm | |
| Column Width | 8 | in | 95.25 | mm | |
| Minimum required length | 4 | in | 110 | mm | |
| Minimum required width | 8 | in | 95.25 | mm | |
| Checking length | OK | | OK | | |
| Checking width | OK | | OK | | |

Table2. Vertical bars and confining ties

| Rebar Installation | Value | Unit | SI Value | Notes/References |
|---|---|---|---|---|
| Vertical rebar quantity | 4 | bars | | |
| Bar size # | 3.0 | | | |
| Hoop Ties/ Confined ties | | | | |
| Diameter(Smooth bar) | 0.197 | in | 5 | mm |
| Hook Ends | 135 | degrees | | |
| End Length at Tangent point | 2.50 | in | | 6*$d_{b\ or}$ 2.5" (eqtn 3-15 MSJC 3.3.3.2) |
| Clear Cover | 2 | in | 40 | mm |
| Tie Spacing, s | 8 | in | 203 | mm |
| End Column tie spacing | 4 | in | 101.5 | mm |

Table3. Vertical tie-element to wall connection. Wall 1- Toothing option

| Toothing | Value | Unit | | Notes/References |
|---|---|---|---|---|
| Toothing connection to wall | 2 | sides of the wall | | |
| Toothing length | 3.8 | in | | 1/2 of brick unit for toothing |
| Brick Unit | | | | |
| Type | Old | Brick | | |
| Unit compressive strength | 4470 | psi | | |
| Unit type | Solid | | | |
| Size | | | | |
| Long | 7.625 | in | 193.675 | mm |
| Height | 2.5 | in | 63.5 | mm |
| Thickness | 3.75 | in | 95.25 | mm |
| f'm | 1715 | psi | | Prism compression test |

Table4. Vertical tie-element to wall connection. Wall 2- Dowel option

| Steel reinforcement | Value | | Unit | Notes/References |
|---|---|---|---|---|
| Dowel into wall | 2 | sides of the wall | | |
| Dowel total length | 15.7 | in | 40 | cm |
| Dowel vertical bent hook | 12.00 | in | 30.48 | cm |
| Dowel size(Bar#3) | 0.375 | in | | |
| Column geometry | | | | |
| Height | 13.125 | ft | 2 | m |
| Length | 13.125 | ft | 4 | m |
| Thickness | 8 | in | 203.2 | mm |
| Cross sectional Area | **1260** | in2 | **0.8128** | $m^2$ |
| Dowel vertical spacing | 14 | in. | **35.56** | cm |